Investigation of Radar Signal Interaction with Crossflow Turbine for Aviation Application

Prifysgol Abertawe
Swansea University

Nikolay Litov

Department of Engineering
Swansea University

This dissertation is submitted for the degree of
Doctor of Engineering

January 2023

Declarations

This work has not previously been accepted in substance for any degree and is not being concurrently submitted in candidature for any degree.

Signed.....N.Litov.....

Date.....10/01/2023.....

This thesis is the result of my own investigations, except where otherwise stated. Other sources are acknowledged by footnotes giving explicit references. A bibliography is appended.

Signed.....N.Litov.....

Date.....10/01/2023.....

I hereby give consent for my thesis, if accepted, to be available for electronic sharing

Signed.....N.Litov.....

Date.....10/01/2023.....

The University's ethical procedures have been followed and, where appropriate, that ethical approval has been granted.

Signed.....N.Litov.....

Date.....10/01/2023.....

Abstract

The increased adoption of wind energy is an important part of the push towards a net zero-emission economy. One obstacle that stands in the way of a higher rate of wind energy adoption is the interference that wind turbines cause to nearby radar installations. Wind turbines negatively affect the performance of nearby radar sites in a variety of different ways. Almost all types of radar are affected in at least one of these ways.

In order to understand the degree to which an object such as a wind turbine interacts with radar, it is important to have detailed radar cross section (RCS) data for the object. In this work, a novel, low-cost, scale model radar cross section characterization system is presented with various advantages over traditional designs. This system was used to characterize the RCS of the novel Crossflow wind turbine. Additionally, work has been carried out on the characterization of metamaterial absorber coatings that can be applied to new and existing turbines for the purposes of reducing their radar cross section and the degree to which they cause radar interference. The works presented can be leveraged to reduce concerns around radar interference from wind turbines, as well as to iteratively generate geometries with lower radar cross sections for the aviation and infrastructure sectors, ultimately accelerating the pace of wind energy adoption and the move towards a net zero-emission economy.

Dedication

I would like to thank my supervisor for his tireless efforts and for being accommodating in the face of difficult challenges, as well as for believing in me as a student and supporting my work. Additionally, I would like to extend my gratitude to the staff of the Materials and Manufacturing Academy at Swansea University for organizing the EngD scheme and for their invaluable support through challenging times.

I would like to dedicate this thesis to my wonderful and hard-working parents who have supported me throughout and instilled me with the important values of perseverance, determination, hard-work, and problem solving.

To my amazing grandmother, who has been unwavering in her belief in me and has played an integral role in my upbringing and in me completing this work.

To my devoted and loving girlfriend, who, in her infinite patience, has been by my side throughout this process and through extremely difficult times.

Declaration

I hereby declare that except where specific reference is made to the work of others, the contents of this dissertation are original and have not been submitted in whole or in part for consideration for any other degree or qualification in this, or any other university. This dissertation is my own work and contains nothing which is the outcome of work done in collaboration with others, except as specified in the text and Acknowledgements. This dissertation contains fewer than 40,000 words including appendices, bibliography, footnotes, tables and equations and has fewer than 100 figures.

Nikolay Litov
April 2022

List of publications

1. N. Litov et al., "Radar Cross Section Analysis of Two Wind Turbines via a Novel Millimeter-Wave Technique and Scale Model Measurements," IEEE Access, vol. 10, pp. 17897–17907, 2022, doi: 10.1109/ACCESS.2022.3148064.
2. N. Litov, H. Zhou, and A. Mehta, "Low Cost Millimetre-Wave Scale Model RCS Characterisation," in 2020 IEEE International Symposium on Antennas and Propagation and North American Radio Science Meeting, Jul. 2020, pp. 1147–1148. doi: 10.1109/IEEECONF35879.2020.9329798.
3. N. Litov, A. Pal, and A. Mehta, "Ring Resonator Metamaterials for Radar Cross Section Reduction," in 2019 IEEE International Symposium on Antennas and Propagation and USNC-URSI Radio Science Meeting, Jul. 2019, pp. 1329–1330. doi: 10.1109/APUSNCURSINRSM.2019.8888700.

List of Abbreviations

2D	2-Dimensional
3D	3-Dimensional
EC	Equivalent Currents/Edge Currents
EMI	Electromagnetic Interference
FSS	Frequency Selective Surface
GHz	GigaHertz
LHCP	Left-handed Circular Polarization/Left-handed circularly polarized
MoM	Method of Moments
PCB	Printed Circuit Board
PEC	Perfect Electric Conductor
PMC	Perfect Magnetic Conductor
PO	Physical Optics
RCS	Radar Cross Section
RHCP	Right-handed Circular Polarization/Right-handed circularly polarized

Contents

List of Figures

List of Tables

1 Introduction

The number of wind turbine installations globally has been increasing at a rapid pace, fuelled by the desire of governments to transition to a carbon neutral economy and reduce the reliance of the economy on fossil fuels and other non-renewable energy sources.

One of the issues associated with the increased adoption of wind energy is the interference that wind turbine structures cause to the normal operation of nearby radar installations. This has led to a number of restrictions being placed on the areas within which wind turbine developments are permitted, as well as the establishment of exclusion zones of a certain radius around key radar installations.

Due to the increased scrutiny faced by wind turbine development planners when it comes to obtaining planning permission, the adoption rate of wind energy has reduced. That is to say: The increased scrutiny that large wind turbine developments face when applying for planning permission is one of the major barriers to the continuation of the fast current pace of wind power adoption.

One of the key metrics used when assessing the impact of a structure on a radar installation is the Radar Cross Section (RCS). This is a measure of the degree of reflectivity that an object exhibits when illuminated by a radar signal of interest. The higher the RCS of an object within the vicinity of a radar installation, the greater the area that the object will shadow behind itself, and the greater the area of clutter generated.

Thus, when considering the interference generated by a certain object, it is useful to have a detailed understanding of the RCS of the object. This gives us an idea of how great the level of interference presented is likely to be.

Additionally, moving objects generate significant Doppler spectrum contamination when within the line of sight of a radar installation. This is another major source of interference, as while stationary clutter can often be filtered out based on the observed velocity, when attempting to filter out Doppler clutter it is possible to also filter out targets of interest. This is due to the fact that the blade tip speed of wind turbines is often above the lowest expected observed velocity from a tar-

get of interest such as an aircraft. Additionally, the filtering of Doppler spectrum contamination is further complication by the fact that many civil aviation radars lack height resolution, making it impossible to filter out wind turbine clutter by setting a height threshold for object detection.

One of the main motivations of this work therefore is to characterise the RCS and Doppler spectrum returns of the Crossflow turbine, a novel design of wind turbine created by Crossflow Energy. As this is a novel design of turbine with a unique geometry, data for the RCS and Doppler spectrum returns of the turbine do not currently exist in the literature. These metrics are important to obtain so that they can be used in order to assess the potential impact of the turbine on any radar installations. Additionally, data on the radar interference/reflectivity/Doppler spectrum returns of the Crossflow turbine is useful for the purposes of comparing the performance of the Crossflow turbine against existing designs such as the horizontal axis, three bladed design most commonly observed.

The RCS of an object can be obtained using electromagnetic simulation software, which has the advantages of being low-cost, fast, and typically not requiring high-cost bespoke hardware. However, the simulation results obtained must be experimentally verified. This can be achieved via scale model or full scale RCS measurements. Both of these methods require expensive bespoke hardware. In the case of the full scale measurement, a radar system operating at the frequency of interest must be obtained. Commercially available solutions are extremely expensive, while a bespoke solution is not only expensive but bears the additional requirements of design, construction, and calibration. In the case that validation by scale model measurement is chosen, the construction of a bespoke system is typically required, as commercially available solutions do not typically exist at the high frequencies required for valid scale model RCS measurements.

Thus, one of the other motivations of this thesis is the design and construction of a bespoke RCS testbed for the purposes of characterizing the RCS of a scale model of the Crossflow turbine in order to validate the RCS results obtained via simulation.

In addition to this main body of research, investigations were conducted into

the use of radar absorptive materials and frequency selective surfaces for the purposes of reducing wind turbine radar interference. Such a technology could be retroactively applied to existing wind turbine installations in order to reduce their existing impact on nearby radar installations.

One of the main aims of this research was to characterize the radar interaction characteristics of the Crossflow turbine.

The aims provided at the start of the project are given below:

- Development of a radar wind turbine testbed
- Measurement and simulation on a scaled Crossflow Wind Turbine model
- Establish radar signature for Crossflow Turbine at various turbine heights and diameters taking into consideration ground effects
- Use of 3d EM simulations for analysing wind turbine scattering, shadowing and clutter

Initially, the characterization of the RCS of the Crossflow wind turbine using EM simulation software was considered. Various different softwares were considered and ultimately used for the characterization of the radar signatures of the Crossflow turbine.

An extremely detailed production ready CAD model of the Crossflow turbine was provided by Crossflow Energy, featuring a high level of detail involving all bolts, fixings and sub-assemblies. The model was created in Solidworks. Solidworks, CST Microwave Studio, and Blender were all used in order to simplify the model geometry and remove superfluous features such as bolts etc. which were very small in relation to the wavelengths of interest.

Initially, simulations the Crossflow turbine were run using CST Microwave Studio using the various different solvers available within the software that were suggested within the documentation as being suited for RCS simulations, namely the Time Domain solver, the Integral equation solver, and the Asymptotic Solver. CST Microwave Studio was initially used as a license was readily available at the university and in use at the Antenna and Smart City Lab. It was quickly

discovered that CST Microwave Studio and the solvers that it made available may be unsuitable for the task of simulating such a large and complex structure with the required accuracy on the machine that was being used at the time, which boasts a dual-core i5-6200U, 2.8GHz max processor, 16GB of RAM and integrated graphics. In order to accelerate the simulation, two different computing clusters available at Swansea University were employed via MPI computing, however the computing power available was still not sufficient to simulate the RCS of the turbine within a reasonable timescale. Simulation times in the order of 1 week for one aspect angle when leveraging the available compute clusters were observed, regardless of the CST solver used.

As a result of this, different software solutions for simulating the Crossflow turbine were investigated. Ultimately, the XGtd software from REMCOM was selected due to its claimed suitability for simulating electrically large structures, and its ability to leverage GPU computing. The software achieves this via a Physical Optics and Method of Equivalent Currents (ME+POC) solver technique.

This thesis describes the RCS characterization of two different turbine types, one of which is entirely novel in its design.

In this Chapter (Chapter 1), several topics are covered. The motivation for carrying this research is described. The research objectives and methods considered for use in this work are described. Finally, an outline of the thesis is provided.

Chapter 2 provides a review of the literature on the topics of radar cross section simulation and characterization, as well as on the topics of frequency selective surfaces, metamaterial absorbers, and electromagnetic cloaking devices.

Chapter **??** describes the simulations efforts carried out to characterize the RCS of the Crossflow turbine model, as well as the RCS of a horizontal-axis wind turbine model to be used as a point of comparison with the data obtained for the Crossflow turbine.

In Chapter 5, the design and construction of a novel, low-cost, millimeter-wave scale model RCS testbed constructed using off-the-shelf, commercially available components is described. The system is used to measure the RCS of a scale model of the Crossflow turbine, and good agreement is demonstrated between the

simulated and experimentally obtained results.

Chapter 6 describes the work carried out on the topics of frequency selective surfaces and their use in RCS reduction, as well as the modeling of their behaviour using equivalent circuit models. The screen printing method is also described and work is carried out on the design of a novel, flexible-substrate, low-profile absorptive/transmittive frequency selective surface for the purposes of RCS reduction.

Finally, in Chapter 7, conclusions and recommendations for future work are provided.

2 Background

Wind turbines are a strategically important renewable energy resource. Recently, there has been an increase in the adoption of renewable energy sources including wind power [6] [7] as part of a push by many governments towards reducing greenhouse gas emissions and the use of fossil fuels. An increase in installed wind energy generation capacity is necessary in order for us to meet current carbon emission reduction targets [6] [7]. As the number of global wind turbine installations has grown, there have been increasing reports of wind turbines interfering with neighboring radar installations in various ways [8] [9] [10] [11] [12] [13]. Firstly, wind turbines cause shadowing when they are located within the line of sight of a radar installation, reducing the radar's capability to track targets behind a wind farm. Secondly, the multi-path interference generated can cause the radar to show wind turbine images in places where they are not located. Additionally, due to their blade length, large wind turbines exhibit large blade tip speeds and significant Doppler spectrum contamination as a result [14]. These can often be above the minimum unambiguous velocity detectable by the radar, making them very difficult to filter, and causing the initiation of false tracks in the vicinity of the wind farm.

There exists a body of research on ascertaining the radar cross section of conventional three bladed horizontal axis wind turbines (HAWTs), with results available from measurements on full scale wind turbines, a scale model platform, as well as simulation results. In this respect, the interaction of radar with conventional and widely distributed HAWTs is well defined. HAWTs have been observed to appear as large ground targets which also appear as non-stationary due to the moving blades creating Doppler spectrum contamination [15] [16] [17]. The Crossflow wind turbine is a novel design which has not yet been widely distributed, and as a result, there is an absence of research detailing the interaction of radar, and in this case specifically aviation radar, with the Crossflow wind turbine.

First, the research that has been done on establishing the interaction of radar with HAWTs and other large objects is presented and evaluated, following which,

the specific gaps in knowledge regarding the Crossflow wind turbine are identified.

The paper which is perhaps most relevant to the project is produced by researchers at Oklahoma University [3], and looks at the radar cross section of a traditional HAWT. In this study, the researchers show that the scale model radar measurements show very similar results to both the EM simulations and the full scale wind turbine radar measurements. This is ideal, as it affirms that a scale model measurements is a valid approach to calculating the radar cross section and other effects of the Crossflow turbine.

2.1 What is radar?

Radio Detection and Ranging (Radar) [18] systems have been used in the civilian and defense sectors for a number of decades and in a wide variety of applications. The principle that is exploited for the operation of radar is the reflection of electromagnetic waves from solid objects. An illustration of this can be observed in Fig. 1.

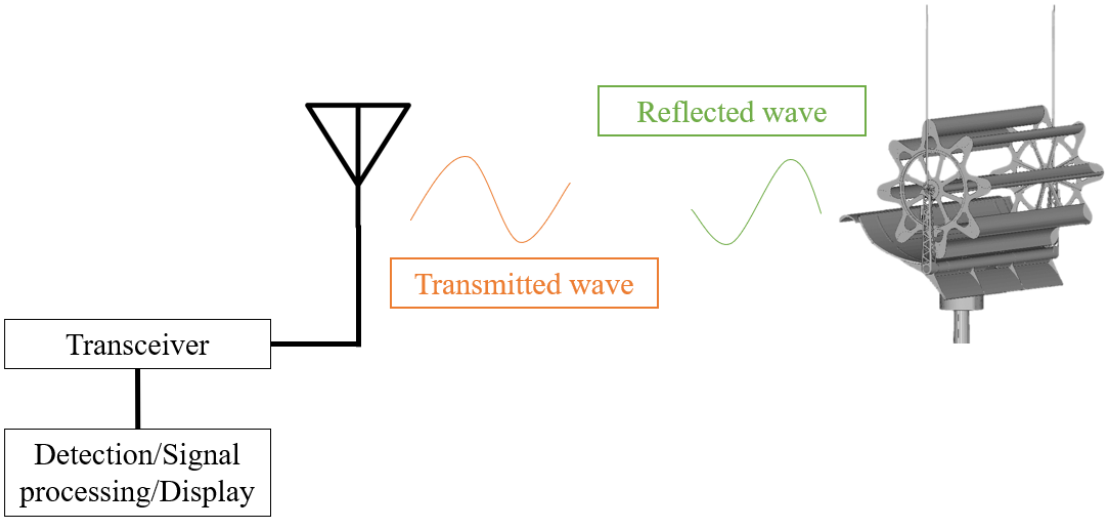

Figure 1: A diagram showing the fundamental principle of operation of radar with an image of the Crossflow turbine as the reflecting object.

Some of the earliest experiments involving radar were carried out by Christian

Hülsmeyer in 1904, who filed patents for a system capable of detecting ships and estimating the range to the ship from the detector. This was perhaps the first radar system constructed capable of both detection and ranging [19]. Hülsmeyer's system used a 50cm wavelength and a spark gap to produce the pulsed signal. His system was demonstrated to officials but was rejected at the time.

Following these early experiments, radar was extensively developed by many countries for military purposes. One of the major following developments was that of the cavity magnetron, the first working prototype of which was presented in 1940 [20].

2.2 Radar and aviation specific applications

Radar is a system that is used for object detection at range. This is achieved by using electromagnetic radiation, usually in the form of radio waves or microwaves. The first step in detecting an object using a radar system is to illuminate the object with electromagnetic radiation. This may be achieved using a rapidly rotating antenna, which illuminates a broad area continuously. At the same time, a second, in most cases co-located antenna (the same antenna as the one used for transmitting is in some cases used) listens for any returned signals. When the transmitted electromagnetic radiation is incident on an object, it will interact with it in a number of ways - in the majority of cases, some of the electromagnetic radiation will be "scattered" i.e. reflected back in the direction of the radar, hence allowing the second antenna to receive it. If the object that the electromagnetic radiation is incident upon is metallic and conductive in nature, the incident radiation will excite currents in the object and cause it to re-radiate some radiation, thus acting as a standalone radiating antenna. In addition to this, the object will naturally reflect some of the the incident radiation. This process is called scattering, and the intensity of the radiation which is scattered back in the direction of the sender, as well as the angle of the returned scattered radiation, is a function of the size and shape of the object on which the radiation was incident, as well as the material which it is made from, the distance of the object from the radar system, and the velocity of the object relative to the radar system.

Initially, in order to express radar cross section, the effective equivalent area of a flat plate reflector was used. Currently, the radar interaction characteristics of the target is expressed as the area of an equivalent isotropic reflector [21]. This is expressed as the symbol σ. As a result of the wide variation that is seen in terms of values for radar cross section, logarithmic units are often used. Thus, the radar cross section will be presented as dBm^2. These units can be interpreted as a ratio of the received power and the power that would have been reflected from a target with an area of one meter squared. Hence, a reading of $20dBm^2$ would mean that the object in question has the same radar cross section as an isotropic reflector with a surface area of 10^2, or $100m^2$.

The radar cross section of a target is a complex parameter which is dependent on both the characteristics of the incident wave, in addition to characteristics of the illuminated target. In terms of the incident wave, the key features are the polarization of the wave, the propagation angle i.e. the angle at which the incident waves approaches the target, and the operational frequency of the source producing the illuminating wave. With regards to the characteristics of the target which affect the radar cross section, these are chiefly the target geometry and the material properties of the target.

The definition of radar cross section which will be used for this project is given as the following equation:

$$\sigma = 4\pi R^2 \lim_{R\to\infty} |\frac{E_s}{E_i}|^2$$

where R is the distance between the radar transceiver and the target in meters, θ is the Radar Cross Section in dBm^2, E_s is the far field scattered electric field intensity, and E_i is the far field incident electric field intensity.

This equation is applicable only in the far-field region, which is also ensured by the specified limit that R tends to infinity. The ratio of E_s and E_i is the ratio of the electric field intensities of the scattered radiation and the incident radiation.

2.3 Aviation specific radar

Airport surveillance radar is the name given to the specific application of radar technology in detecting the locations and presences of aircraft in a certain area around an airport, often called the terminal area. It is the primary method of controlling the air traffic around airports, and is used in directing planes and preventing collisions.

There are two main radar systems which are used in airport traffic surveillance. These are called the primary and secondary surveillance radar [22]. The primary surveillance radar is comprised of a parabolic antenna dish that is fed with a peak power of 25kW and a mean power of 2.1kW, and is rotated in order to pass a vertical fan shaped beam of electromagnetic radiation in all directions, thus detecting aircraft in all directions within a certain radius around the airport. The primary surveillance radar operates in the S band frequency range of 2.7-2.9GHz.

The secondary airport surveillance radar has the capability of interrogating information from the aircraft, which includes the following data:

- Aircraft identification
- Barometric altitude
- Emergency status code

The secondary surveillance radar operates in the L band frequency range of 1.03-1.09GHz and a power in the region of 160W-1500 W.

2.4 Radar types and modes

2.4.1 Mono-static Radar

Mono-static radar is defined as radar in which case the transmitting and receiving antennas are co-located [23], or in some cases, are even the same antenna. In this case, a switching circuit is employed in order to switch the same antenna between transmitting and receiving modes. This is possible because antennas have symmetrical characteristics in terms of gain when receiving and gain when transmitting.

2.4.2 Bi-static radar

In the case of bi-static radar, the receiving and transmitting antennas are not co-located, but are instead separated by a distance which is in the order of magnitude of the distance expected between the target and the radar installations. One of the advantages of this type of radar as compared to a mono-static radar installation is the covert operation of the receiver - the receiver location cannot be known by the target, whereas with the mono-static mode of operation, the target knows where the transmitter is due to the fact that the transmitting and receiving antennas are co-located.

2.4.3 Multi-static radar

In the case of multi-static radar, there must be at least three components, comprising of any mixture of receivers and transmitters, for example two receivers and one transmitter, or vice versa. One of the advantages of multi-static radar is a potentially higher target classification ability, through the ability to view the target from multiple aspects in the case of multiple transmitter receiver pairs.

The most commonly used civilian airport surveillance radars are mono-static, and so the most concern will be given to calculating the RCS of the Crossflow wind turbine within this context.

2.5 Radar polarization

Polarisation within the context of electromagnetic radiation e.g. radar is taken to mean the property of the electromagnetic radiation which specifies the orientation of the oscillations [24]. The most commonly used modes of polarization, and the three modes most easily selectable for the polarization mode of the excitation wave used during the radar cross section measurement in CST Microwave Suite are linear polarization, circular polarization, and elliptical polarization.

Circular polarization is exhibited by an electromagnetic wave when the electric field component and the magnetic field component oscillate orthogonally to one another, are of the same magnitude, and are 90°out of phase with one another. It is possible to describe the direction of the circular polarization as left or right handed, or clockwise/anti-clockwise. The wave is considered Right-handed circularly polarized (RHCP) if it is rotating clockwise and Left-handed circularly polarized (LHCP) if it rotating anti-clockwise when viewed from the source in the direction of propagation.

Elliptical polarization is another mode of polarization, and can also be described as partial polarization. This mode of polarization is achieved when both the electric and magnetic field components of the wave are not oscillating in exactly the same plane as each other orthogonal to the direction of propagation of the wave, however they are both present and may be oscillating with different magnitudes to each other, have a any value of phase difference, or any combination thereof. This usually results in elliptical polarisation.

Linear polarisation is a polarisation mode which is characterised by the direction of the electric field vector [25]. In the case of horizontally linearly polarized radiation, the electric field is confined to the horizontal plane orthogonal to the direction of propagation of the wave.

2.6 Multipath clutter effects

Multipath clutter, or clutter created by multipath propagation of the radar signal, is a phenomenon whereby the reflected signal from the object reaches the receiving antenna via a path different to the one it took to to reach the object. In certain cases, this can result in false images being present on the radar due to the reflected wave occuring on the receiving antenna from a different place than the object that scattered the wave. In addition to this, it is possible for multipath propagation to produce both destructive and constructive interference, and possibly make the object that initially scattered the wave look larger or smaller than expected. Multipath propagation effects can also affect a phase shift in the reflected signal, and thus produce errors in the velocity signals read by the radar regarding an object.

2.7 The different types of electromagnetic scattering

Scattering is the process by which electromagnetic radiation and particles are forced to change direction from a straight path into one or more differently angled paths due to discontinuities in the media through which they are propagating. In this instance, the most important type of scattering is that incurred by radar illumination signals as they interact with the target.

A closed form solution does not exist for calculating the electromagnetic scattering induced by arbitrary shapes, however there are closed form solutions for the scattering induced by spheroids and other simple shapes.

2.7.1 Mie scattering

Mie scattering is a method of calculating the scattering caused by a spherical object which is of a diameter much larger than the wavelength of the electromagnetic radiation in question [21]. At this stage, the scattering characteristics of the object are much more closely linked to the geometry of the object as opposed to just the size.

2.7.2 Rayleigh scattering

Rayleigh scattering is the solution of electromagnetic scattering that can be applied to spheres which are much smaller in diameter than the wavelength of the electromagnetic radiation in question [21]. Together with absorption, this is one of the main mechanisms of attenuation of electromagnetic radiation in the atmosphere.

2.8 Relative velocity detection using radar

The shift in frequency of the returned radar signal can be used to ascertain the velocity of the target object relative to the radar system. An increase in the frequency of the returned signal indicates that the target is moving towards the observer, while a decrease in the frequency of the returned signal indicates that the target object is moving away from the observer. The change in frequency of the radiation reflected from a moving object is known as the Doppler effect. This functionality is useful, especially when detecting the direction and speed of travel of the target is extremely vital, such as in certain military applications, however this functionality is also useful in civilian applications such as aviation radar.

2.9 Radar hardware

2.10 Oklahoma paper

The hardware which is generally used for measurements of radar cross section is a scatterometer. A scatterometer measures the return of the electromagnetic radiation which is scattered by the target in question.

In essence, the scatterometer is a monostatic radar system. In the paper by Kong *et al.* [3], the scatterometer build is explained as pertaining to the project.

The system also has a mode switching module which allows different parts of the horn antenna to be energised independently, thus allowing the researchers to examine the radar cross section using different modes of polarization, which is a robust methodology and ensures greater completeness of observations and conditions.

Table 1: System parameters presented by Kong *et al.* [3]

System parameters	Values
Operating frequency	10.5 Ghz
Peak transmit power	126 mW
Antenna gain	12dBi
Antenna 3dB beam width	30 degrees
Transmit pulse width	8-20 ns
PRF (Pulse repetition frequency)	95-24400 Hz
System bandwith	100 MHz

The system was also mounted on a rotor, in order to simulate both the scanning mode of a radar system, as well as the spotlight mode.

In terms of the data acquisition, a 200MHz sampling rate PCI data acquisition card was used in order to sample the incoming waveform with the same frequency as that at which the transmitting waveform is pulsed. A 16 bit resolution is used in order to capture the scattered signal with a high resolution. The incoming data from the acquisition card was saved to hard disk in real time so that a record of the experiments is maintained.

This paper is presented as it describes a complex bespoke system and highlights many of the challenges associated with the design and construction of a bespoke system for the purposes of indoor scale RCS characterization, namely the difficulty in designing a system capable of meeting the high-frequency operation required to satisfy electrodynamic similitude theory.

2.11 Yamada paper

In the paper by Yamada *et al.* [26], a vector network analyzer is used, while connected to a PC running LabVIEW. This is a much more elegant and straight forward solution than making custom hardware, and writing custom scripts in MATLAB in order to visualize the data, which was the approach taken in the paper by Kong *et al.* [3]. In addition to this, a commercial vector network analyser can most likely achieve much greater levels of accuracy and precision than a bespoke setup.

2.12 Ochodnicky paper

In a paper by Ochodnicky *et al.*, a comprehensive list of rules is layed out for performing the an RCS measurement using the comparison method [27]. The most important rules that need to be observed when performing radar cross section characterization using scale models are as follows [27]:

- The measurements must be performed in the far field radiation region of the antenna
- The minimal dimensions of the object under test must be in the optical scattering region i.e. large compared to the wavelength used
- The object under test must be within the 1st Fresnel's zone
- Multi-path interference and echoes from the surroundings must be avoided

2.13 Naval stealth from Design to Real Life - Lecture

In this lecture, the results of a scale model navy ship radar cross section test are presented. The researchers use a scale model of size 1:75 in an anechoic chamber [4]. The researchers also outlined the way in which they scaled each of the variables they used during the scale model testing [4]. These are presented in Table 2.

Table 2: Scale model testing parameters presented by Heemskerk [4]

Parameter	Scaling relationship
Time	$t_{model} = \frac{t_{fullscale}}{S}$
Frequency	$f_{model} = f_{fullscale}.\mathrm{S}$
Wavelength	$\lambda_{model} = \frac{\lambda_{fullscale}}{S}$
Conductivity	$\sigma_{model} = \mathrm{S}.\sigma_{fullscale}$
Resistance	Does not scale
Permittivity	Does not scale
Permeability	Does not scale
Antenna gain	Does not scale
RCS	$RCS_{model} = \frac{RCS_{fullscale}}{S^2}$

Where S is the scaling factor, which in this specific case is 75. This paper gives a good description of how the most important factors in the scale model simulation should be scaled down in order to obtain good accuracy and result validity.

2.14 Radar cross section reduction methods

A number of different solutions and mitigation measures have been employed for the reduction of RCS and specifically the problem of wind turbine-radar interference. One of these is the application of radar absorptive coatings (RAM coatings) and metamaterials for reduction of RCS [28] [29]. RAM coatings are designed to absorb the incident electromagnetic radiation and convert it to heat, thus reducing the magnitude of the reflected electromagnetic radiation. One type of RAM consists of an array of pyramid shape foam structures. This type of RAM is often used to line the inside of anechoic chambers used for conducting electromagnetic measurements, with the aim of reducing the interference of reflections from the wall of the measurement chamber. The foam is usually impregnated with conductive carbonyl carbon black spheres. The size of the pyramid shapes is dependent on the frequency of the radiation being used.

Another type of RAM which is frequently used is an iron ball paint absorber. This comes in the form of a paint containing small spheres coated with ferrite or carbonyl iron. The best formulas for this type of RAM material are highly classified and used in military applications for the RCS reduction of aircraft and marine vessels. For high effectiveness, it is also required that the iron balls are arranged in a specific pattern, making the manufacturing of this type of coating difficult.

One alternative approach of reducing radar cross section is a Salisbury screen [30]. It is considered to be one of the initial concepts within the field of radar cross section reduction techniques. The Salisbury screen works on the principle of splitting the incident wave into two waves which are 180°out of phase with each other, thus causing them to combine and cancel out through negative interference. A disadvantage of the Salisbury screen is that it only works for one frequency, so as a RCS reduction measure it can be defeated by a frequency hopping radar. Also, depending on the wavelength of the frequency in question, the Salisbury screen may need to be quite thick, and so may impede aero- or hydro-dynamic performance. The effective bandwidth of the Salisbury Screen can be improved through various multi-layer designs. One variation on the Salisbury screen is a

Jaumann absorber.

Split ring resonators also offer radar cross section reduction capabilities. Split ring resonator technology has been demonstrated to provide the most effective incident radiation attenuation out of any radar absorptive approach. The split ring resonators resemble an "O" shape with a gap, or more accurately a "C" shape. They can also be other shapes, such as a square. The gap in the ring is tuned to the frequency range in question.

A very tentative technology which is not yet ready for mass application is the application of carbon nano-tube paints to radar targets. Carbon nano-tubes have been shown to absorb electromagnetic radiation in the microwave range. In addition to this, the carbon nano-tubes reduce the visible light reflectivity of the surface they are applied to. There are some major hurdles to the manufacturing of this type of coating, however work has been done on using various different methods for suspending the carbon nano-tubes in a paint to use for coating.

Finely powedered silicon carbide has also been added to heat resistant paint before being applied to stealth aircraft in order to aid with radar cross section reduction.

Finally, metamaterials are another class of radar absorptive technologies which can be employed for the reduction of radar cross section. The definition of meta-materials is materials that have properties that do not exist in nature - in the specific electromagnetic case, this is taken to mean a material or object which has electromagnetic properties different from the constituent materials, and electromagnetic properties which are not arising from the properties of the materials used for the construction, but rather arising due to the structure of the materials. Meta-materials have been the object of extensive study due to their incredible and extremely rare properties - namely the ability to exhibit a negative index of refraction, in addition to negative permittivity and permeability with regards to electromagnetics [31] [32] [33].

These solutions involving the use of radar absorptive coatings or frequency selective surfaces/metamaterials have however not been implemented widely at the design and manufacturing stage, and are very costly to apply retroactively to

wind turbines that have already been commissioned.

A further proposed approach capable of realizing the reduction of wind turbine-radar interference and which has been used for the RCS reduction of targets generally is that of shaping, i.e. tayloring the shape of the object in question with the goal of reduced direct electromagnetic reflection in mind. In the case of the wind turbine blades, this is not possible, as aerodynamic performance constraints are the main driver for the blade shape. At the same time, it can be difficult and costly to redesign the tower of the turbine so that it exhibits a lower RCS. Typically, the interference of wind turbines is mitigated via the establishment of exclusion zones around radar installations [34] [35].

2.14.1 Papers relating to radar cross section reduction techniques

One invention that has been patented by Qinetiq [36] is a Jaumann type filter construction that can be applied to the blades of the wind turbine, and has been shown to signifcantly reduce the radar cross section of the wind turbine, without a significant increase in manufacturing complexity, cost, or difficulty. In order to reduce the impact of the potential increase in weight that may be caused by the addition of a RAM coating, Vestas (the company that built the stealth turbine prototype according to the Qinetiq design) and Qinetiq incorporated the RAM coating in two layers consisting of a glass reinforced epoxy and a plastic foam, which were built into the construction of the wind turbine as opposed to being an addition to the existing design. The end result of this design decision was an identical weight to a conventional non-stealth wind turbine blade, however Qinetiq did report that they expect the increase in cost over conventional blades to be in the order of 10%.

Overall, there is a concensus that the radar cross section of the turbine is not greatly dependent on the height of the turbine [37], nor is it possible to greatly reduce the radar cross section of the blades of the turbine by changing their shape, due to the very specific shape required from the blades for the aerodynamic properties necessary [37]. It is however possible to use RAM coatings or layers incorporated into the construction in order to reduce the RCS of the blades, however this

may carry weight penalties, and at least up until now has been shown to always carry a cost penalty during the construction of the turbine and blades.

2.14.2 Metamaterial papers and applications for the reduction of radar cross section

Some of the first research into radar absorptive meta-material designs was performed in the 1980s and 1990s. The first designs centred around applying artificial chiral media to achieve a reduction in RCS [38]. Chirality in this instance refers to an object which cannot be bought into congruence with a mirror image of itself only through the use of rotations and translations in space [38].

One of the first developments and seminal works in terms of creating meta-materials specifically designed for their electromagnetic properties was written by Daniel Friedric Sievenpiper [39]. In this doctorate thesis, Sievenpiper presents an in-depth discussion of high impedance electromagnetic surfaces. Much of the information here is also useful in understanding the various mechanisms involved in radar signal scattering and also RCS reduction. Sievenpiper presents a novel (for the time) design for a high impedance electromagnetic surface which does not support the propagation of surface waves with a certain narrow bandwidth of frequencies. This is accomplished through the use of raised flat surfaces which are suspended above the ground plane by a connecting middle section and are also separated from each other by a small air gap. When these elements are much smaller than the wavelength of radiation in question, they can be modelled as a lumped element model circuit. The gap between the surfaces presents the capacitive component, and the current path from surface to surface presents the inductive element, thus creating a conventional LC filter structure from the viewpoint of the surface currents and leading to a reduction in their propagation.

In order for a meta-material designed to interact with electromagnetic waves to be effective, the structural features of the material must be smaller than the wavelength. As a result of this, the feature size is often in the order of millimetres, for microwave radiation applications. Meta-materials with a negative permeability are metamaterial designs that have a magnetic permeability of less than 0 i.e.

$\epsilon = 0$, but a positive permittivity. This is one explored subset of meta-materials. The second is meta-materials with a negative permittivity i.e. $\mu = 0$ and a positive permeability. The third subset of meta-materials which is not quite so frequently explored is the double negative class of meta-materials, i.e. where both permittivity and permeability are negative ($\epsilon = 0$, $\mu = 0$) [40]. There are various designs available, some of which utilize the split ring resonator [41].

In a paper published in the International Microwave and RF conference (IMaRC), a metamaterial absorber working in the C band is presented which is designed to reduce the radar cross section of an antenna by being placed around it. It is stated that the resonator meta-material is designed for reducing the RCS of a planar antenna [42].

In a paper titled "Thin AMC Structure of Radar Cross-Section Reduction" [43], the authors present a geometrically simple and relatively thin meta-material structure which can be applied for the reduction of RCS. This structure makes use of a cross-hatch pattern of perfect electric conductor (PEC) and artificial magnetic conductor (AMC) structures. The reduction in radar cross section using this method is achieved through a similar mechanism as that of the Salisbury screen, i.e. reflecting the incident radiation in such a way as to cause de-constructive interference between the reflections. The cross-hatch pattern achieves this by dual material nature - the artificial magnetic conductor cells reflect the incident signal with no induced phase shift, whereas the perfect electric conductor cells produce a phase shift of 180°in the reflected wave.

Similar results have also been achieved by other researchers, for example in a paper titled "Broadband Radar Cross-Section Reducting Using AMC Technology" [44]. In this paper, the researchers responsible were able to achieve similar results to the researchers in the previously presented paper. In this case, the researchers employed the use of a chessboard structured pattern consisting of two elements. This is the main difference in implementation as compared with the previously presented paper. According to the researchers, the "condition for destructive interference is maintained", however due to the fact that the two AMC elements can be tuned to different frequencies while this condition is maintained,

wideband operation is achieved. The researchers are also able to achieve broadband radar cross section reduction, in addition to a RCS reduction greater than 10dB. With this design the properties of easy manufacturing the the ability to conform to a surface of complex geometry are maintained, making this ideal for applications to existing structures.

For the above two papers, it has been shown that they are only really valuable over a relatively narrow range of frequencies, mostly due to the repeating unit cell design. The unit cell can only resonate at so many different frequencies. Another example of a proposed meta-material application for radar cross section is the paper by Song et. al. [45]. In this paper, the researchers present an extremely wideband meta-material that has shown a minimum of 10dB radar cross section reduction over the entire X-band (7-12GHz). The meta-material is also polarisation insensitive. These properties are achieved through a repeating and rotating unit cell based on several differently sized patch designs, two of which being a ring patch design. A novel approach to designing the repeating units has also been employed, involving the construction of four intertwined sub-arrays. This is an interesting piece of research which could potentially be applied in a film format to the outside of objects with the aim of RCS reduction. It also seems relatively straight forward and inexpensive to manufacture, resulting in low application cost - ideal for retrofitting to existing structures and vehicles.

Another paper which has been presented claims a wideband RCS reduction of 10dB "over 60% frequency bandwidth" [46]. In this paper, the researchers produce a meta-material design based on electromagnetic band gap (EBG) unit cells arranged in the form of a checker board pattern. The property of the EBG unit cell structure which is exploited to produce the radar cross section reduction is the frequency phase shift relationship exhibited by the material. That is to say, the phase shift of the waves reflected by the meta-material is different to that of the incident wave. The magnitude of this phase shift changes with the frequency of the incident radiation. The variation which is achieved is from +180°to -180°in a linear fashion with increasing frequency from 0 to 8GHz. In practical testing, the researchers achieved a 10dB or lower reduction in radar cross section over the

frequency range of 4.2 to 7.5GHz, or a span of 3.5GHz. This is a wide enough span to cover the frequency ranges used by airport surveillance radar, and so it is feasible that this type of design could be scaled to the frequency band of interest for this work.

Another paper which covers a proposed wideband EBG meta-material structure is titled "Wideband Smaller Unit cell planar EBG structures and their applications" [47]. In this paper, the researchers discuss a wideband meta-material comprised of a repeating structure of EBG unit cells. The main application for this material proposed by the researchers is actually the use of the material between the antenna and ground plane to reduce the interference of the signal being reflected from the ground plane of the antenna. The S_{21} parameters are presented for the material. The S_{21} parameter refers to the 2-port network convention used for defining the incident, reflected, and transmitted signals for an element. The S_{21} parameter refers to the radiation intensity which is passed through the network, in this instance meaning the EBG element.

One of the main drawbacks with certain EBG and other meta-materials is the dependence on normally incident radiation. This makes certain meta-material designs inapplicable to the radar cross section reduction of the Crossflow turbine or other objects/vehicles. One of the reasons for this is the multitude of curved surfaces on the Crossflow turbine which are essential in meeting the aerodynamic performance requirements. Even of the incident radiation is also incident from a direction orthogonal to the face of the turbine, it will not be incident from a direction orthogonal to the many surfaces of the turbine. In the application of certain meta-material designs for the reduction of RCS, performance would be reduced. Another reason why they are not very well suited for application to existing structures is the fact that the Crossflow turbine will change orientation frequently as the wind direction changes, meaning that the incident radiation will almost always be illuminating a target from a direction which is not orthogonal to the front facing plane.

In addition to this, the goal of meta-materials research in terms of creating a frequency selective surface for radar cross section reduction is to absorb the

incoming radiation. This can be useful in reducing the radar cross section seen by mono-static radar, i.e. it can be a useful approach to reducing the radiation scattered directly back in the direction from which it was incident. However, this does not address the problem of multi-patch scattering and ghosting, whereby radiation can be scattered by an object, then from the surroundings, and back to the receiver. It also may not be an ideal approach in trying to reduce the radar cross-section as seen by bi-static radar systems. In addition to this, it does not remove the shadowing caused by the object, which is also a pertinent concern in the context of air surveillance radar, as aircraft directly behind a target causing shadowing may be missed by the radar. This shadowing would also allow the cloaking to be detected.

One design exists which attempts to address these concerns, i.e. produce an ideal cloaking device for electromagnetic radiation [48]. The paper achieves this by controlling the path of the incoming electromagnetic radiation in such a way as to guide it around and behind the object - this is achieved via spatial variation in the electromagnetic parameters of the cloak [49] [50].

2.14.3 The current state of meta-material research regarding RCS reduction

There have been a variety of meta-material designs aimed at reducing the RCS of a target through absorbing the incoming radiation and converting it to heat, thus removing the portion of the backscattering pattern in the direction of the transmitter. Other types of designs have focussed on re-directing the incident radiation in different directions. Unfortunately, a disadvantage of both of these approaches is that they do not take care of the shadowing caused by the object, which both obstructs the view of the radar (undesirable in the case of a wind turbine near an airport) and allows the cloaked object to be detected through detection of the shadowed region in certain circumstances. A lot of these solutions are also planar solutions and so cannot be applied to all surfaces of the target.

Newer types of designs focus on guiding the incident radiation around the target [48] [51] [52] [53] [54] [55]. Unfortunately, these meta-materials are most

often in the shape of a cylinder. It would not be appropriate to place a cylinder around a wind turbine, as this would prevent the turbine from generating any energy.

One of the pieces of research that proposes a meta-material design based on the Minkowski FSS addresses the previously mentioned issues - most importantly, it is almost completely polarization insensitive, in addition to being insensitive to the angle of incidence of the incoming radiation [56]. Also, this is an extremely thin planar solution which seems like it could be applied almost as a film to the outside of an existing target. However, this kind of design does not guide the electromagnetic radiation around itself, thereby still not removing the problem of shadowing.

Ideally, a new meta-material design is needed. One that is thin, can be mounted on a flexible substrate for retro-fitting to existing structures and vehicles, and also guides radiation around itself without absorbing any of it, no matter what the polarization or incident angle is of the incoming radiation.

2.15 Andrade *et al.* paper and the feasibility of using a RAM coating for mitigation

With regards to the possibility of using radar absorptive material (RAM) coatings to reduce the radar cross section of the wind turbines, there has been work done examining the efficacy of this approach on attempting to reduce the radar cross section of fighter aircraft for military applications, namely reducing the distance at which the aircraft is first detected by hostile radar [57].

The researchers presented a 3D model of an F-5 fighter aircraft, and tested the radar cross section of the aircraft at 11.1GHz for different RAM coating scenarious, from almost completely coated in RAM, to almost completely uncoated. The tests were performed in simulation using the CST Microwave suite. The researchers state that the same frequency was used for all tests due to the frequency dependence of the RAM coating effectiveness, which varies from between -5dB reduction in reflectivity at 9.2GHz to -28.06dB reduction in reflectivity at 11.2GHz for the specific FC70 RAM coating used in these experiments.

2.16 Wind farm clutter mitigation in air surveillance radar paper

In this paper, the authors discussed wind farm interference mitigation techniques which are based on a UK Royal Air Force demonstration. They also quantify false alarm and false track reductions as a result of the mitigation solutions employed.

The experiments were performed using a Watchman S-band radar which is used for short range air traffic control and which was in the vicinity of a number of wind farms in South Wales. [5].

Initially, the radar was calibrated and was then used to record multiple days worth of data of aircraft flying over the wind turbine farms near the radar in pre-planned scenarios. The next step in the proceedings for the researchers was the installation of a replacement signal processor and tracking system (SPE-3000 upgrade kit) by Sensis [5]. This upgrade kit was used to replace all of the existing radar electronics apart from the transmitter and antenna. The receiver of the SPE-3000 is interfaced with the low noise amplifier (LNA) of the Watchman radar and is downconverted to an intermediate frequency of 6MHz, before being fed into a 14 bit analogue to digital converter, for use in the Radar Signal Processor system.

Overall, the researchers reported the following data in terms of performance of the wind turbine interference mitigation measures taken with regards to spurious and missed plots in and around the wind turbine sites:

Table 3: Wind farm interference mitigation results as claimed by Perry *et al.* [5]

Wind farm	False plots	Missed plots
C	3	3
D	1	4

This paper shows that there has already been significant work done with regards to mitigating the effect of wind turbines by changing the radar hardware and software to newer digital based methods. This may be a far cheaper option than attempting to change the design of turbines which are to be installed, or attempt-

ing to retrofit RAM coatings, shrouds, or other mitigation methods to existing turbines. Improving current radar systems would not only reduce the negative intereference of radar with existing wind farms, but also create the opportunity for the improvement of the capabilities of the radar beyond the mitigation of negative inteference. Examples of other improvements which modern radars may exhibit over older analogue models are better target recogntion, better range, i.e. earlier target detection from a further distance, and improved resistance to jamming attempts through the employment of technologies such as frequency hopping (so called frequency agile radars). In addition to this, modern radars generally will have better accuracy, both in the spatial domain and in the Doppler domain. This would result in an overall increase in national security when applied to military radar, e.g. allowing radar operators to detect targets earlier and be able to identify targets earlier. Also, civilian aviation radar would benefit from such improvements in radar, which would give airport control radar operators the ability to more closely track the movements of planes within the terminal area of the airport, and thus have a greater margin of safety when directing aircraft, reducing the likelihood of mistakes leading to off course aircraft or the greater possibility of mid-air collisions.

2.17 Project impact

The project is kindly sponsored by Crossflow Energy, in addition to the M2A, The Welsh European Social Fund, and Swansea University.

One of the key impacts of this project is the addition of another competitive advantage for the Crossflow company, in addition to the already existing competitive advantages inherent to the design of the turbine such as improved serviceability, lower cost, and improved performance during low wind conditions.

Additional cost savings will be realized through the envisaged reduction in length of the planning permission application process that will be realized by removing the need for a radar interference survey to be carried out in certain areas.

When the project is completed, the radar cross section of the turbine will be

known, and various methods will have been employed in order to reduce it. Depending on the degree of success of the project, it is even possible that the turbine could be made entirely invisible to radar. This will massively open up the areas in which Crossflow is able to apply for permission to build turbine installations. This will have a huge impact for the company, and in turn for the local economy through the creation of more employment opportunities. Some of the locations which would become accessible for development include the areas near and around airports, as well as the areas near military bases.

In terms of the impact on the wider economy, the more widespread integration of renewable energy generating Crossflow turbine will result in a more diversified and decentralized grid. It will also reduce the dependence of the grid on energy generation through the burning of fossil fuels. Infrastructure in more remote locations could be simplified, by potentially completely removing the need for a link to the national grid. In addition to this, more remote expeditions may be enabled and research/military bases could be built in locations where they previously could not have been due to infrastructure concerns.

The results of the research related to reducing the radar cross section of the wind turbine will also be applicable to other objects. The methods may be used in the development of the next stealth aircraft and ships. This would be a very large project impact, potentially resulting in a significant tactical advantage in military applications.

2.18 Environmental impact of the project

There are various aspects which must be considered when giving thought to the environmental impact of the project. These can be broken down into two broad sections. One section is the environmental impact of the activities conducted throughout the duration of and leading up to the resolution of the project, while the second broad section is the environmental effect of the outcome of the project.

With regards to the activities that will be conducted throughout the duration of the project, it is not anticipated that any of these should have a significant environmental impact. A large portion of the work and design will be conducted in

simulation - this does not require the consumption of any resources, excepting the electricity used to power the machines, and the associated environmental impact of the electricity generation. Unfortunately, large computational capacity is required when dealing with simulations and design of this scale, which required a large quantity of electrical power. There will be some environmental impact associated with the generation of this power, as the national grid is not powered entirely from renewable sources. Some resources will be consumed during practical testing for the radar cross section and radar cross section reduction methods. The bespoke antennas for the small scale mono-static radar set-up will be made from metal, which is recyclable. The materials that will be used to construct the meta-material RCS reduction layer and the materials that will be used to construct the scale model Crossflow turbine have not yet been chosen, however consideration will be given to the possibility of recycling the chosen materials, and they will be chosen to minimize environmental impact while ensuring they have the correct properties for the task.

The environmental impacts of the successful completion of the project will be positive and significant. It will be much more straight forward to apply for planning permission to erect one or several radar invisible Crossflow turbines in a variety of locations where it was hitherto impossible to build renewable wind energy power installations due to radar interference concerns. This will increase the adoption of renewable energy on a global scale, thus reducing the dependence on fossil fuels for power generation. Radar invisibility would also allow the Crossflow turbine to be erected on large tanker/cargo ships, which will reduce their consumption of extremely polluting fuel which contains higher levels of sulphur compounds than conventional diesel fuel [58]. The Crossflow turbine can achieve this by satisfying some of the power requirements of the ship. This will be a significant result in terms of pollution reduction, as large ships contribute significant amounts of pollution, and are set to contribute more in the future [59]. Overall, the environmental impact of the successful completion of the project will contribute significantly to the end goal of removing our dependence on fossil fuels.

3 Simulation Benchmark Test Case and Simplified Turbine Model

One of the key metrics used when assessing radar interference is RCS. This metric is a strong predictor of the magnitude of the cluttering and shadowing effects that can be expected to be generated by an object or a new development. Doppler spectrum contamination is also a key metric in determining the magnitude of radar interference generated by an object or development.

Simulation is a key tool in the evaluation of novel structures with regards to their electromagnetic performance and the degree to which they interact with radar signals. Electromagnetic simulations can be used to predict every aspect of radar interference, and they are a generally fast, affordable, and accurate solution to the problem [13]. However, it is necessary for simulation results to be verified experimentally. Full scale measurements can be very time consuming and expensive, requiring access to full scale radar installations [10], [60], as well as posing difficulties with controlling the large number of variables. With scale model measurements, it is easier to set up a controlled environment, the experiment takes less time, and is generally cheaper to perform. However, there are still significant costs associated such as that of building or hiring an anechoic chamber and obtaining a scatterometer system that works at a sufficiently high frequency [26]. Detailed RCS data exists for a variety of widely used wind turbine designs, most notably the horizontal-axis wind turbine (HAWT) geometry with three blades. The Crossflow turbine is a novel wind turbine with various advantages over traditional HAWT designs. The entire Crossflow rotor structure is mounted horizontally on a slew bearing and is driven by motors so that the rotor can be rotated to face the wind to maximize power production, and face out of the wind to reduce the frontal area in extreme wind conditions, thus limiting the loads on the tower and foundation.

In this section, the groundwork for the simulation of the RCS characteristics of the Crossflow turbine and HAWT is described. This involves the discussion around the computational resources required, the simulation methods considered, the challenges associated with the simulation of electrically large scenarios, as well

as results from a number of test simulations on a simplified model which provide an understanding about how the shape of and material from which a structure is constructed from contribute to its RCS characteristics and potential for generating interference.

In this chapter, the work carried out to obtain the simulation data necessary to determine the magnitude and nature of any interference generated by the Crossflow turbine is described. Additionally, the work involved in obtaining simulation data for a three bladed, horizontal axis turbine design is described. Finally, the two sets of simulation data are compared for the purpose of ascertaining any differences in performance between the two designs.

3.1 Computational cluster benchmarking and selection

Due to the very large electrical size of the problem, and the anticipated future need for large computational power due to the high number of simulations that will be run throughout the duration of the project, it was decided that testing needed to be performed on a number of available high performance clusters. The aim of benchmarking cluster against each other using a test simulation was to gain real world computational performance data, and thereby to decide exactly what hardware configuration would be most beneficial to the project.

The problem is computationally large due to the electrically large nature of the structures that require simulation. At the frequencies of interest, the structures are many thousands of wavelengths in size in a number of dimensions. This property of the simulation problem makes it computationally large due to the methods used for modelling an electromagnetic problem. Frequently, Finite Element Method (FEM) models are used for the simulation of electromagnetic scenarios. This method involves the discretisation of the space to be simulated, resulting in a mesh structure. At the points of the mesh, the differential equations involved in modelling the phenomenon of interest, in this case the electromagnetic behaviour of the scene, are evaluated, and the values obtained are interpolated along the edges of the mesh to arrive at a solution for each point in the scene. One of the requirements for a valid simulation is that a minimum number of mesh cells per

wavelength is observed. This is necessary to ensure that the values for electric and magnetic field intensities are calculated at dense enough points as to produce a valid representation of the electromagnetic radiation and its behaviour. This requirement, coupled with the electrically large nature of the scenarios considered, can result in a simulation size in the hundreds of millions to billions of mesh cells.

3.1.1 Benchmark simulation

A model was put together to act in the simulation used for benchmarking for the different clusters. The simulation in question was a 2×8 patch antenna array tuned for the 2.4GHz frequency range. The mesh settings are presented, and were selected to give a high mesh resolution, resulting in a mesh size of ~5.6 million mesh cells. This was to ensure that the simulation was representative of the kind and magnitude of simulations that will be performed.

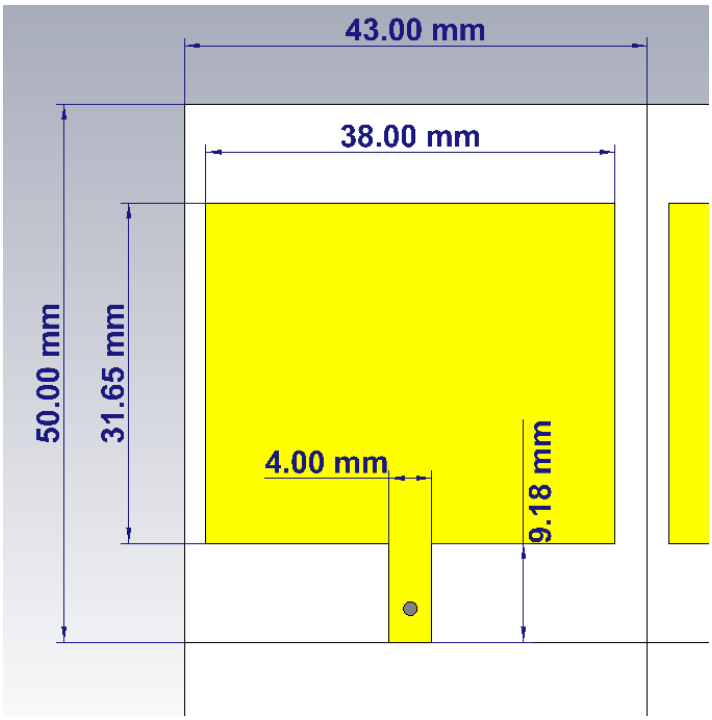

Figure 2: Front view of one of the 16 patch antennas in the 2x8 patch antenna array model used for cluster benchmarking

3.1.2 Clusters and cluster selection criteria

CST Microwave Suite has a host of acceleration methods which are made available to the researcher in order to reduce simulation time. Different solver techniques and problem types lend themselves more or less so to the different acceleration methods.

The different solvers offered by CST are presented below:

- Transient solver
- Frequency domain solver
- Eigenmode solver
- Resonant solver
- Integral equation solver
- Asymptotic solver
- TLM solver
- PIC solver

The two solvers which are most suited for the type of simulations that will be performed on the Crossflow turbine are the Integral equation solver and the asymptotic solver. These are also the default solvers offered when selecting the simulation template for the radar cross section calculation of an electrically large object. It therefore makes sense to choose a cluster with the performance criteria and nature of acceleration which are most suited to this solver. The time domain solver will also be used frequently, especially for smaller scale proof-of-concept simulations; as it is a good and accurate general purpose solver. The CST documentation was also consulted with regards to the suitability of the different solvers for acceleration, and this information was used in conjunction with the simulations result data to make a final decision.

Four clusters were tested using the test simulation. The first cluster was already available and used for research in the Antennas and Smart City Labs, called the IAT cluster. This cluster consists of 16 nodes, each supporting 24 threads (for a total of 384 threads) and 32GB of RAM (for a total of 512GB of RAM). This cluster at present has no GPU capabilities.

The second cluster benchmarked was the High Performance Computing Wales cluster (HPC Wales). This cluster is designed to provide large scale computing resources to academia and industry alike. The cluster is mostly housed in Swansea and Cardiff Universities, with links to Aberystwyth, Bangor, Glamorgan, the University of Wales Alliance Universities in addition to a range of business innovation centres [61]. The HPC Wales cluster is extremely capable, with a wide variety of nodes and acceleration methods. The chief acceleration methods available are load division and distribution via the MPI protocol, in addition to GPU acceleration on some select nodes. Jobs are submitted to the cluster via the SLURM Job scheduler, and the researcher manually inputs the number of cores, RAM, and nodes they wish to employ for a simulation. We were especially interested in gauging the exact gain in terms of time that can be offered by GPUs. It was possible to run some GPU tests on the HPC Wales cluster as they possess a GPU cluster in Swansea containing 16 nodes, each having 16 cores (for a total of 256 cores), and a NVIDIA Tesla M2090 general purpose GPU with 6GB of internal memory.

The third high performance cluster that testing was performed on was the Catapult cluster. This cluster houses a number of nodes, with a wide variety of configurations ranging from nodes with 2 cores and 16GB of RAM to nodes with over 100 cores, 512GB of RAM and up to 8 general purpose NVIDIA GPUs. This was also a useful test opportunity to acquire the realistic impact of GPU acceleration on the solvers and problem types we would be working with. GPU acceleration is well suited to the majority of solvers, except PIC and Frequency domain, though small gains may be had with these solvers also.

Permission was petitioned and granted for access to the Astute cluster, also housed at Swansea University. The Astute cluster houses approximately two thousand cores and over 3TB of RAM. Computations on this cluster are therefore

accelerated through MPI load division and distribution. This is also extremely conducive to our workload, as MPI acceleration gains scale linearly for all solvers. This ensures that we have good acceleration regardless of which solver is being used for a simulation. The extremely large RAM capacity of this cluster is also extremely beneficial, as the Crossflow turbine RCS problem is an electrically very large problem, and even with mesh simplification, will still require a high number of nodes with a large combined RAM capacity. This cluster is also currently available and so is currently the favourite in terms of cost effectiveness, as well as performance.

3.1.3 Benchmarking results and final cluster selection

The parameters for the clusters that were tested are summarised again in Table 4, along with the time they took to complete the test simulation presented in the previous subsection. It must be noted that when the simulation was run on the IAT cluster, the model was recreated in exactly the same way but under the 2015 version of CST. This was because the 2017 version had not yet been installed. This was also one of the tasks that had to be performed in order to ensure the readiness of the IAT cluster for the workload.

Cluster comparison						
Cluster	Acceleration mode	Node	Total cores	Total RAM	GPU acceleration	Time taken for test simulation to complete
IAT Cluster	MPI	N/A	16 nodes × 24 cores = 384 cores	512GB	None	50.5 minutes
HPC Wales cluster	MPI + GPU	Swansea GPU cluster nodes	2 nodes × 16 cores = 32 cores	128GB	2 × NVIDIA M2090	Untested - Estimated to be in the order of 120 minutes
Catapult cluster	GPU	NGO8	1 node × 40 cores = 40 cores	512GB	8 × NVIDIA V100 GPU NVLink	20 minutes
	GPU	NGD5	1 node × 16 cores = 16 cores	128GB	4 × NVIDIA K80 GPU	56 Minutes
Astute cluster	MPI	N/A	~2000 cores	~3TB	None	Untested

Table 4: A table showing the different clusters and the time they took to perform the test simulation outlined previously

It can be seen that the GPU acceleration properties make a significant difference in the simulation time. This evidence is also corroborated by the CST documentation, which states that GPU acceleration can often be non-linear with an increasing number of GPUs, as compared to MPI and distributed computing which often scales linearly with increasing numbers of nodes and threads.

It would therefore make sense to try to employ GPU computing, due to the smaller hardware footprint required and the ease of use. It would be possible to build a very capable computational node with a large number of GPUs for a price in the region of £30 to £60 thousand pounds, that would exceed the capabilities of the IAT Cluster and the capabilities of some of the nodes available in the Catapult cluster. After exploring the option of using the Astute cluster within the context of the results from our benchmarking, it was concluded that building a local GPU compute node would not be the most cost effective or fastest option. This was based on a quote received from OCF for a workstation with 4 × NVIDIA P100 GPUs for a price in the range of £38,000, with an academic discount. Although such a machine would have a significant compute capacity, it would still be dwarfed by the Astute cluster. The Astute cluster is also currently under-utilised, and submitted simulations would not wait in a queue for a long time. This makes the Astute cluster the natural choice of cluster for the largest simulations, however smaller simulations will also be run on the IAT Cluster.

3.2 Simulation methodology and results

3.2.1 Assessment of suitability of CST for simulation

In order to ascertain exactly what methods are available within CST for calculating RCS, several test simulations were performed.

The test simulations which allowed the greatest understanding of how CST Microwave Suite calculates the radar cross section of a target were those of a T-shape made up of different materials. Three separate models were tested. All three simulations were of a T-shaped model, however for the first simulation the material of the T-shape was defined as entirely Plexiglass, for the second simulation

the material was defined to be entirely 1010 alloy steel, and for the final of the three variations on the model, the horizontal part of the T shape was split into two sections - the front facing section was defined to be 1010 alloy steel, while the rear facing section was defined to be Plexiglass. This was with the intention of ascertaining exactly how and from where CST illuminates the target, and how it measures the scattering of the radiation.

Figure 3 is a schematic perspective view of the (a) - simplified T-shaped turbine model defined as being entirely made out of plexiglass, (b) - simplified T-shaped turbine model that has both steel and plexiglass sections, and (c) - simplified T-shaped turbine model defined as being made entirely out of steel. The steel sections are visible as the grey wireframe cuboid and grey solid, whereas all of the blue/purple sections are made of plexiglass. The depth of the horizontal portions of the T is 0.2m, and the steel and plexiglass sections are of equal depth, i.e. 0.1m each.

Next, the excitation wave parameter was viewed in order to understand the nature of the illuminating electromagnetic radiation which was being used for the RCS calculation. It was noted that the electromagnetic radiation being used was a plane wave, which had a linear polarization. The polarization was in the x=1 plane orthogonal to the direction of propagation of the wave, which was in the z=-1 direction, i.e. against the "front" of the T shaped model. Looking at the model from the same perspective view as that shown in the perspective view showing the geometry of the model, the incident face and properties of the plane wave is presented.

The excitation signal which is used for generating the linearly polarized plane wave is a Guassian signal of length 2.5ns. A graphical representation of the signal is presented.

By viewing the fact that there was only one excitation plane wave defined, and after studying the CST documentation in depth, the method used by CST Microwave Suite for calculating the radar cross section of an object became clear. Counter-intuitively, when selecting mono-static RCS as the calculation mode during the initial setup of CST, a bi-static radar measurement is actually conducted.

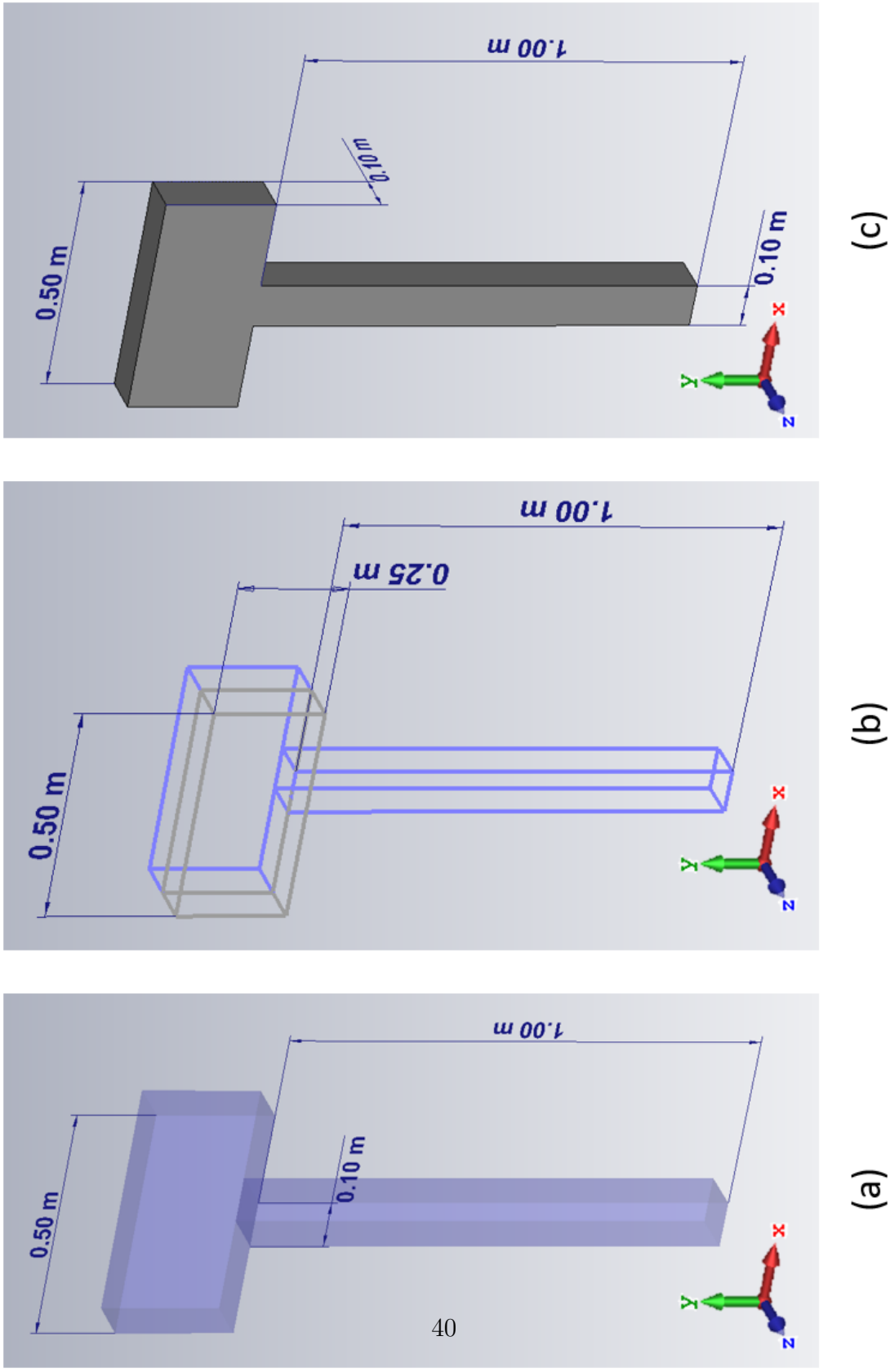

Figure 3: A perspective view of the T-shaped simplified turbine models used for ascertaining the RCS calculation methodology used by CST

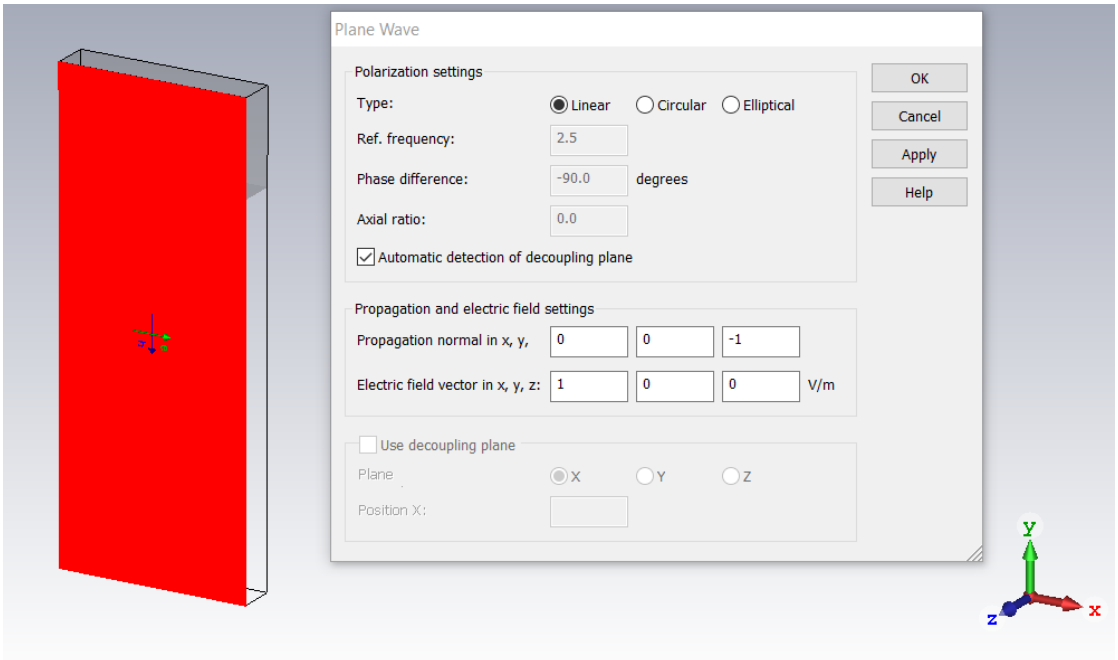

Figure 4: A perspective view of the T-shape model including the plane wave used for illuminating the target

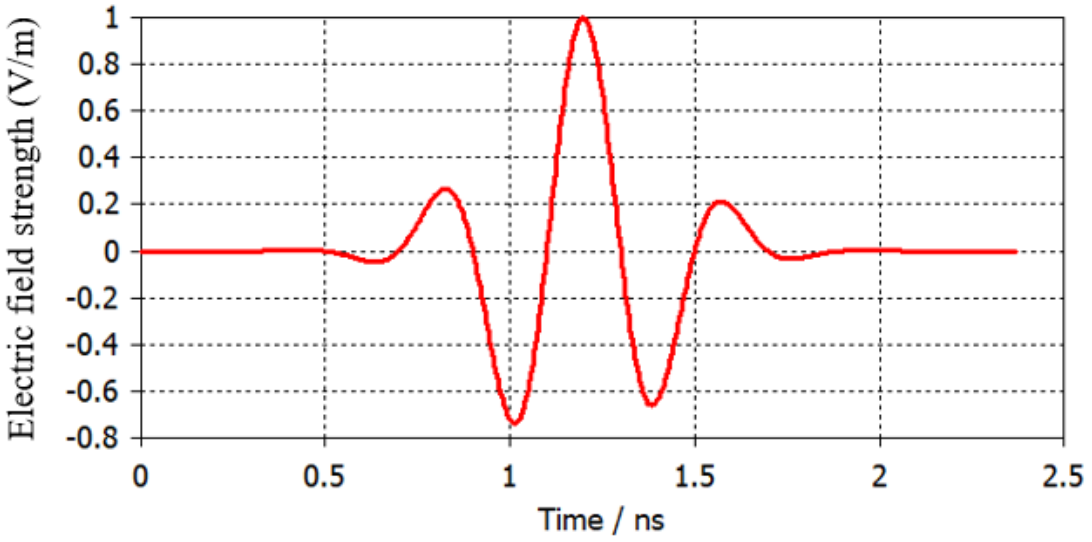

Figure 5: A graphical representation of the excitation signal used to generate the illuminating plane wave

To expand further, the target is only illuminated by the plane wave which is defined under the "Plane Waves" section in the Navigation Tree. The three dimensional far-field radiation plot is then produced by measuring the intensity of the scatter radiation at a range of theta and phi values. That is to say, the target is illuminated from one angle, and the direction which is scattered in all directions around the object is measured.

3.2.2 Simplified Turbine model Simulation

The results make sense with the context of the RCS calculation methodology used by CST Microwave Suite and described in the previous sub-section. They are presented in this section. The results are grouped by frequency i.e. for each frequency step, the results for each of the model material configurations will be presented before going on to the next frequency step. This is so that easy comparison can happen between how the different materials affect the radar cross section.

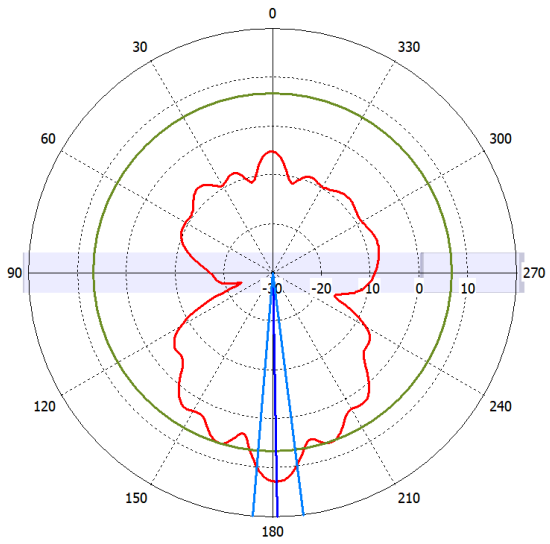

Figure 6: f = 1GHz, Main lobe magnitude = 12.8dBm^2, main lobe direction = 181°, Angular width (3dB) = 11.9°, Side lobe level = -6.1dB.

It can be noted that the direction from which the incident radiation is arriving is from the 0°direction on the polar plots in all cases. It is also clear that in the

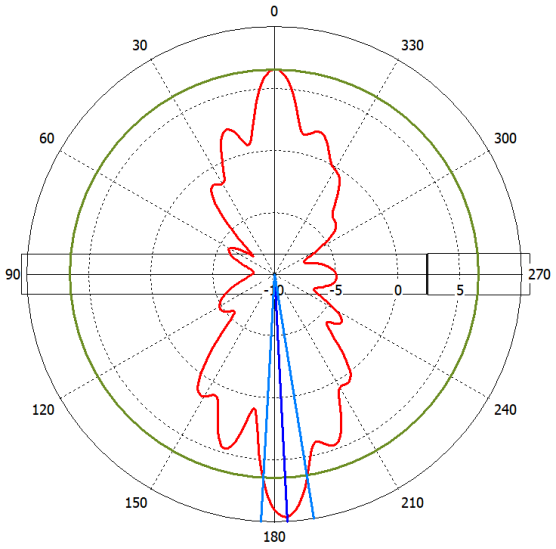

Figure 7: f = 1GHz, Main lobe magnitude = 9.61dBm^2, main lobe direction = 183°, Angular width (3dB) = 12.3°, Side lobe level = -3.1dB.

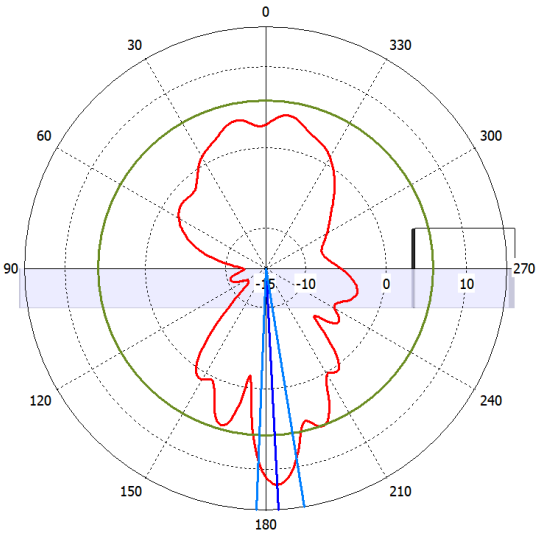

Figure 8: f = 1GHz, Main lobe magnitude = 11.9dBm^2, main lobe direction = 183°, Angular width (3dB) = 11.5°, Side lobe level = -6dB.

majority of cases, the main lobe direction is actually behind the T-piece simulation. This is because of the horizontal polarization of the incident radiation and the

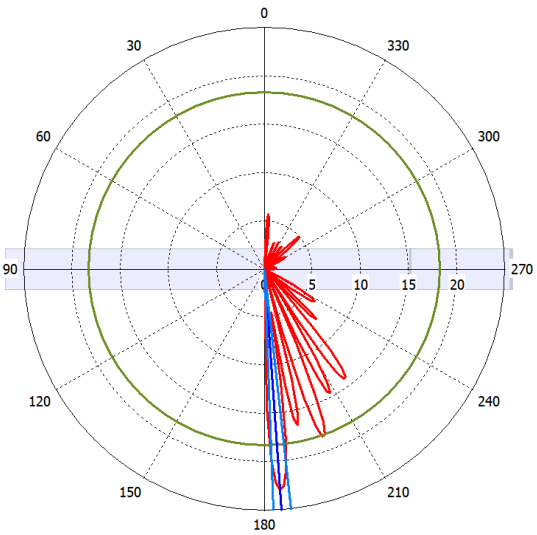

Figure 9: f = 1GHz, Main lobe magnitude = 23dBm^2, main lobe direction = 184°, Angular width (3dB) = 4.2°, Side lobe level = -4.7dB.

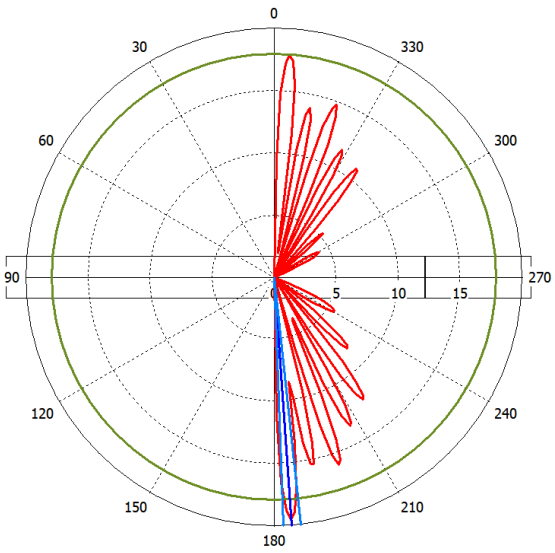

Figure 10: f = 1GHz, Main lobe magnitude = 19.5dBm^2, main lobe direction = 184°, Angular width (3dB) = 4.1°, Side lobe level = -1.6dB.

interaction it has with the geometry of the target object. As the incident radiation is horizontally polarized, the large majority of it will pass around the structure, given the thin tower structure that takes up the majority of the width of the area

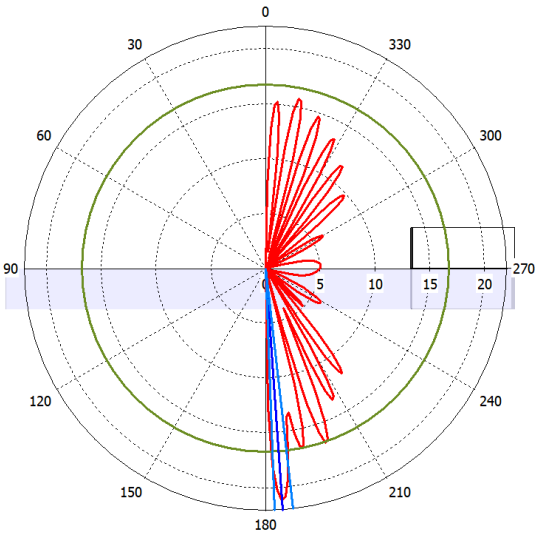

Figure 11: f = 1GHz, Main lobe magnitude = 21.1dBm^2, main lobe direction = 184°, Angular width (3dB) = 4.4°, Side lobe level = -4.4dB.

covered by the excitation plane wave. This is evidenced by the fact that the main lobe of the reflected radiation is lower in magnitude compared to the main lobe of radiation that has passed effectively unhindered behind the wind turbine.

It must also be noted that the flat part of the polar plot where there is no recorded radiation is the location of the ground plane. In the simulation, the bottom of the wind turbine was lined up with the ground plane, even though this is not correctly pictured in the diagrams.

The frequencies of 1 to 1.2GHz are of interest because the radar which interrogates the aircraft transponder unit which provides information such as their unique codes and altitude, status codes etc.

The next major frequency of interest is 2.8GHz, which is used for locating and tracking aircraft within the terminal area of the airport (60 miles radius).

Next, the simulations were repeated, but this time using an excitation wave with specified left hand circular polarization. This means that the excitation wave is composed of two plane waves which interact to form a rotating electromagnetic wave which rotates counterclockwise when viewing the wave from the viewpoint of the source. The results can then be compared to illustrate the interaction between

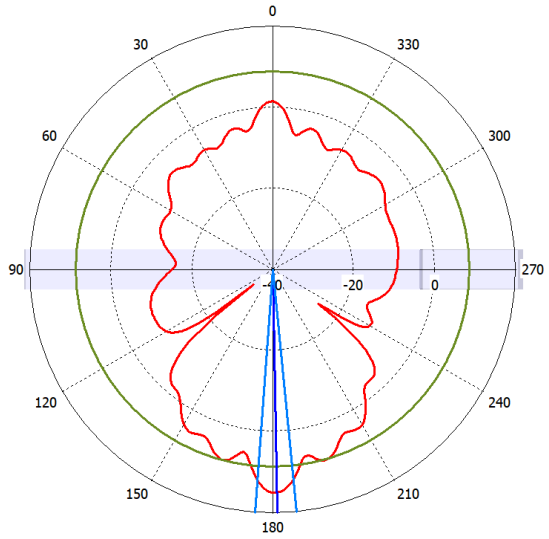

Figure 12: f = 1.2GHz, Main lobe magnitude = 15dBm^2, main lobe direction = 181°, Angular width (3dB) = 9.8°, Side lobe level = -6.3dB.

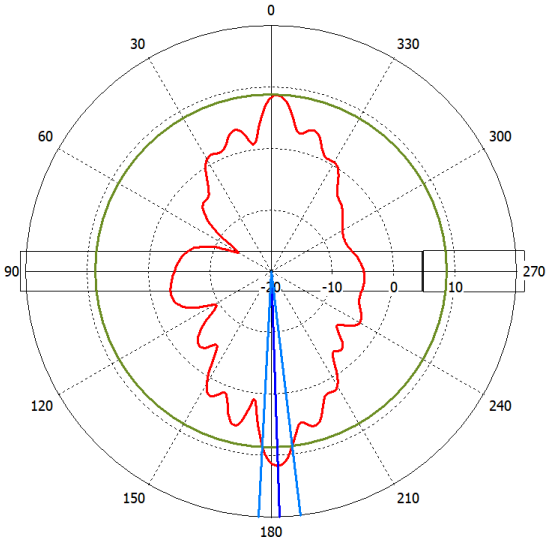

Figure 13: f = 1.2GHz, Main lobe magnitude = 11.6dBm^2, main lobe direction = 182°, Angular width (3dB) = 9.8°, Side lobe level = -3dB.

different wave polarizations and frequencies with the target geometry and material type. The simulations have only been repeated with a ground plane, as this is more

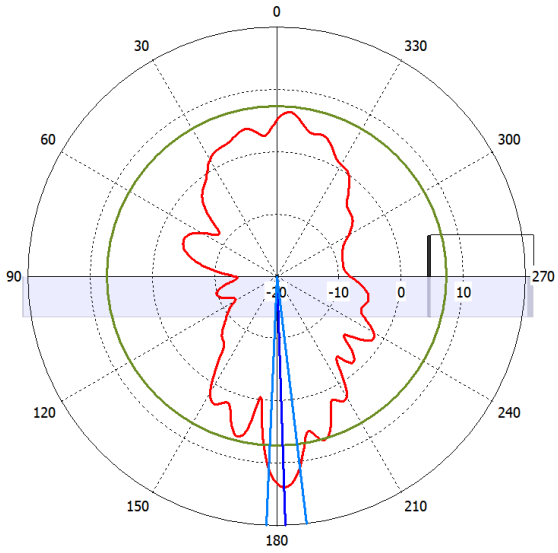

Figure 14: f = 1.2GHz, Main lobe magnitude = 13.9dBm^2, main lobe direction = 182°, Angular width (3dB) = 9.4°, Side lobe level = -6.6dB.

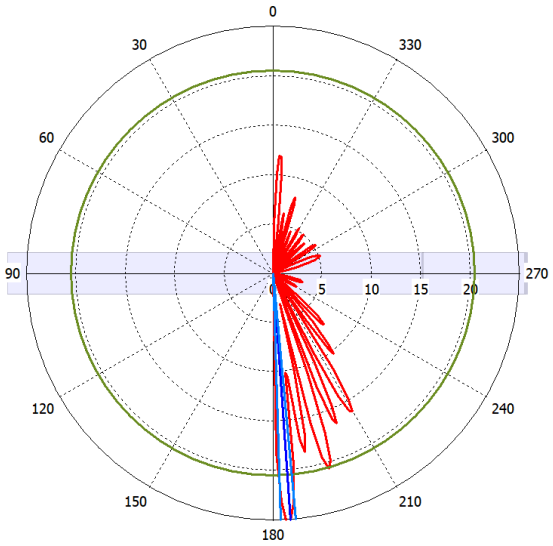

Figure 15: f = 1.2GHz, Main lobe magnitude = 25.1dBm^2, main lobe direction = 184°, Angular width (3dB) = 3.5°, Side lobe level = -4.6dB.

representative of real world conditions, and simulating without one does not add any extra insight into the radar cross section characteristics of the target.

The plan for progression is to reduce the model complexity by rebuilding the

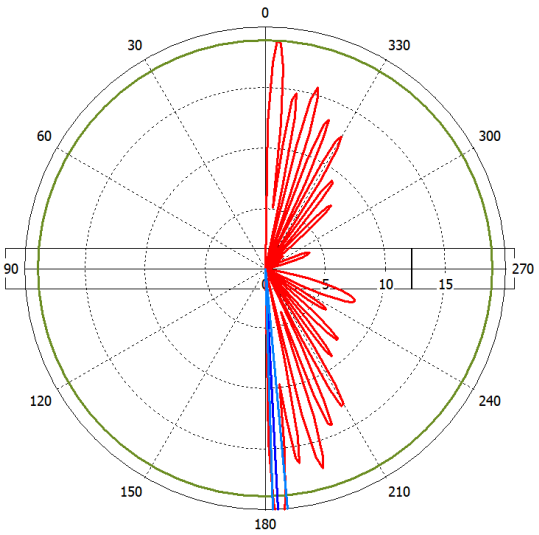

Figure 16: f = 1.2GHz, Main lobe magnitude = 21.2dBm^2, main lobe direction = 183°, Angular width (3dB) = 3.5°, Side lobe level = -2.3dB.

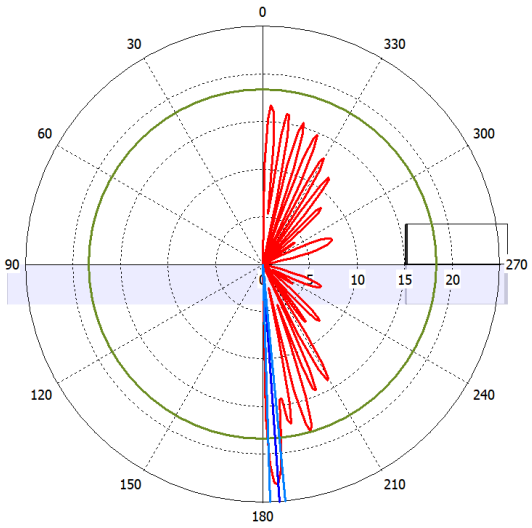

Figure 17: f = 1.2GHz, Main lobe magnitude = 23.1dBm^2, main lobe direction = 184°, Angular width (3dB) = 3.7°, Side lobe level = -4.8dB.

model within CST. To begin and get a general idea of the radar cross section that can be expected from the Crossflow turbine, the T shaped simulation model previously presented was scaled up to the same proportions as the Crossflow turbine.

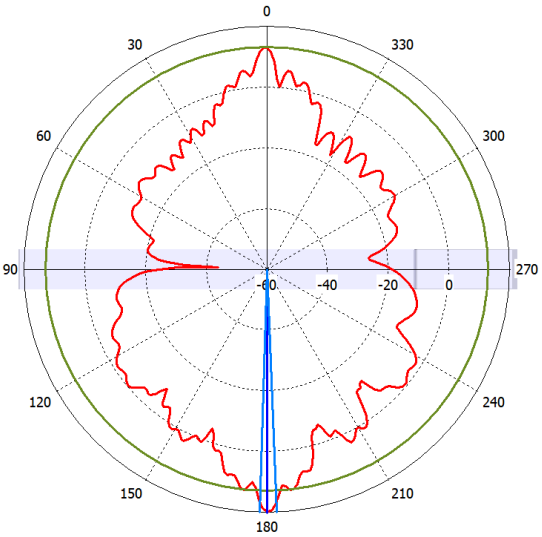

Figure 18: f = 2.8GHz, Main lobe magnitude = 19.7dBm^2, main lobe direction = 180°, Angular width (3dB) = 4.1°, Side lobe level = -6.7dB.

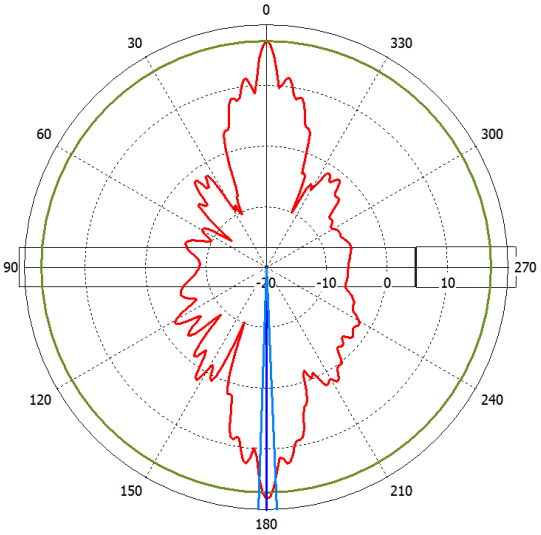

Figure 19: f = 2.8GHz, Main lobe magnitude = 18.2dBm^2, main lobe direction = 180°, Angular width (3dB) = 4.3°, Side lobe level = -1dB.

The large T-shaped model is presented in Fig. 33. The height of the tower supporting the cuboid representing the nacelle is 12m, and the width of the cuboid is 6m. The front face has been defined to be made of steel, in order to give as high a

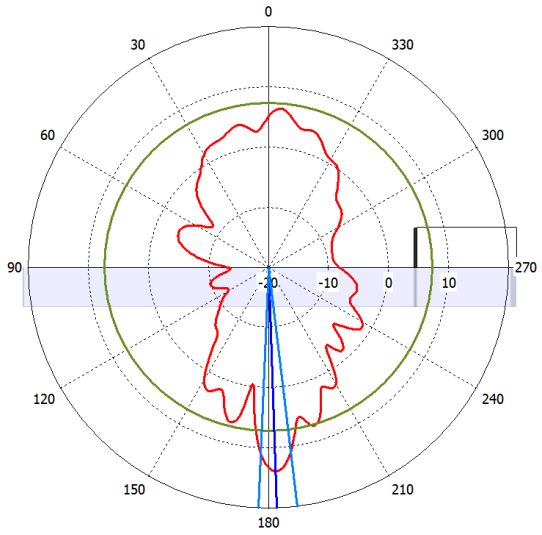

Figure 20: f = 2.8GHz, Main lobe magnitude = 13.9dBm^2, main lobe direction = 182°, Angular width (3dB) = 9.4°, Side lobe level = -6.6dB.

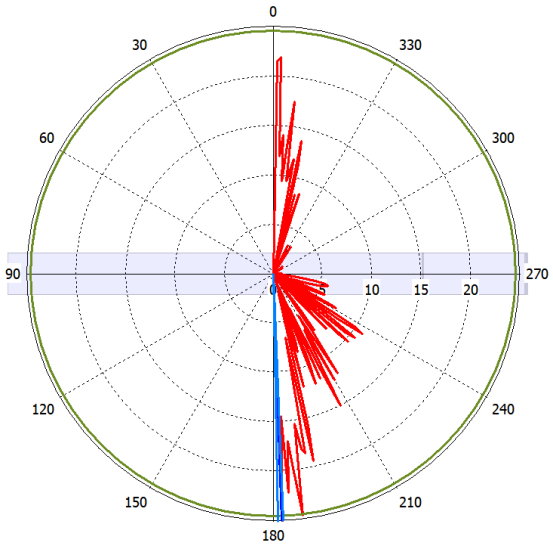

Figure 21: f = 2.8GHz, Main lobe magnitude = 28.7dBm^2, main lobe direction = 182°, Angular width (3dB) = 1.2°, Side lobe level = -4.2dB.

reading for radar cross section as possible in this instance. This simulation was run using the Integral equation solver, which is recommended by CST for electrically

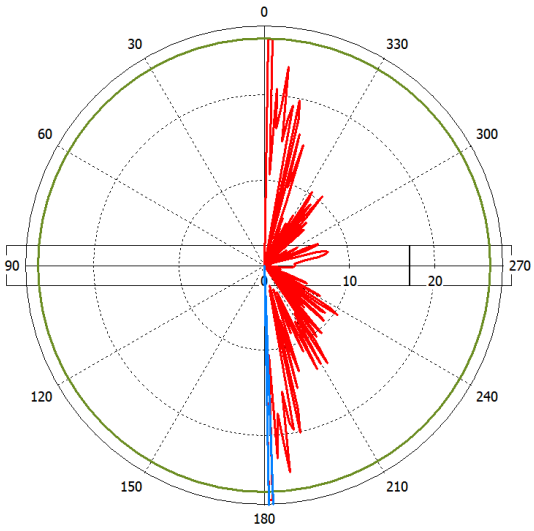

Figure 22: f = 2.8GHz, Main lobe magnitude = 27.5dBm^2, main lobe direction = 181°, Angular width (3dB) = 1.2°, Side lobe level = -1.0dB.

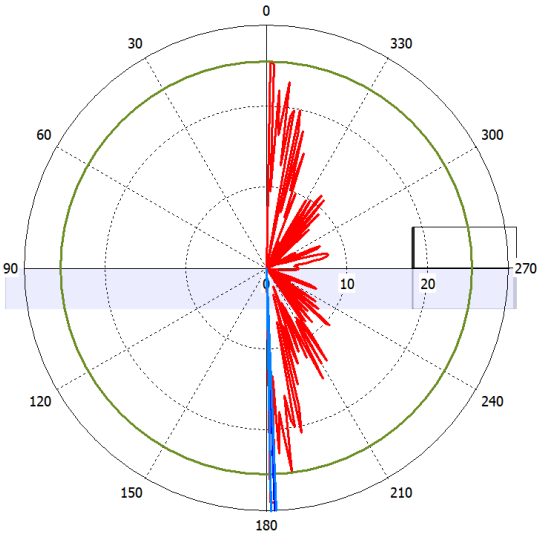

Figure 23: f = 2.8GHz, Main lobe magnitude = 28.9dBm^2, main lobe direction = 182°, Angular width (3dB) = 1.2°, Side lobe level = -3.4dB.

medium to large simulations. Despite the simplicity of the structure, the mesh size generated was 868 million mesh cells - a very large mesh.

The plane wave used to excite this model was linearly polarized and had an

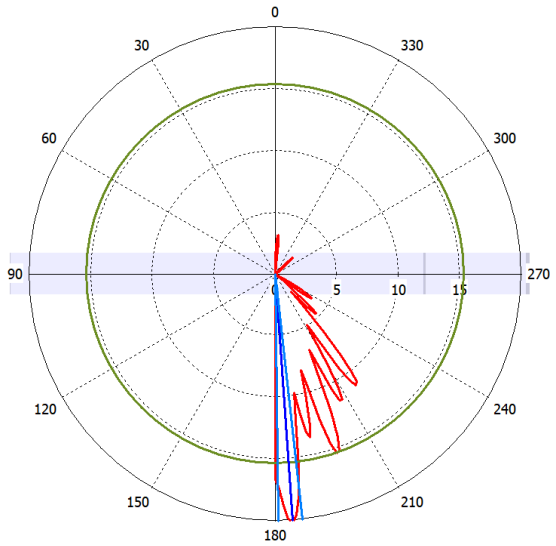

Figure 24: f = 1GHz, Main lobe magnitude = 20.2dBm^2, main lobe direction = 184°, Angular width (3dB) = 5.7°, Side lobe level = -4.8dB.

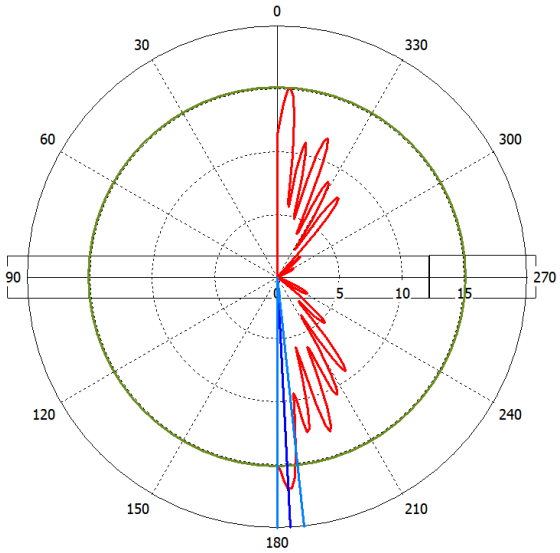

Figure 25: f = 1GHz, Main lobe magnitude = 16.9dBm^2, main lobe direction = 183°, Angular width (3dB) = 6.1°, Side lobe level = -1.8dB.

axial ratio of 1. The results of this simulation showed that we can expect a large radar cross section in the area of 60dBm^2. This is a very significant radar cross

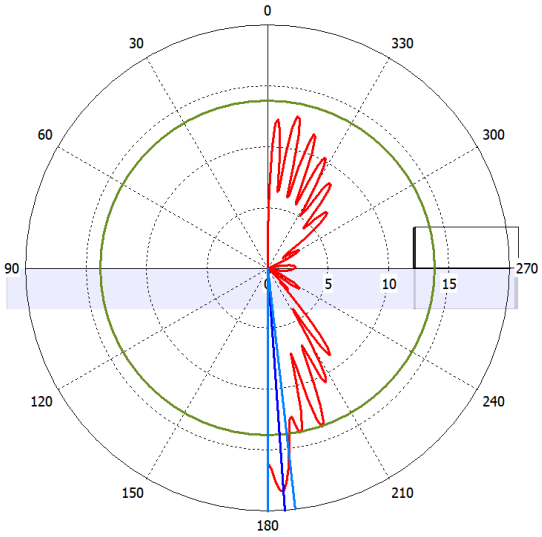

Figure 26: f = 1GHz, Main lobe magnitude = 18.4dBm^2, main lobe direction = 184°, Angular width (3dB) = 6.5°, Side lobe level = -4.6dB.

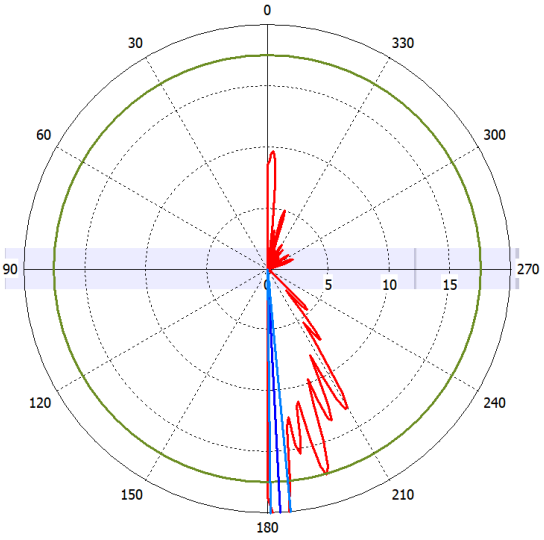

Figure 27: f = 1.2GHz, Main lobe magnitude = 22.4dBm^2, main lobe direction = 183°, Angular width (3dB) = 4.7°, Side lobe level = -4.9dB.

section which is within the same order of magnitude as the radar cross section produced by conventional three bladed wind turbine designs illuminated with a vertically polarized 1.5GHz wave [64].

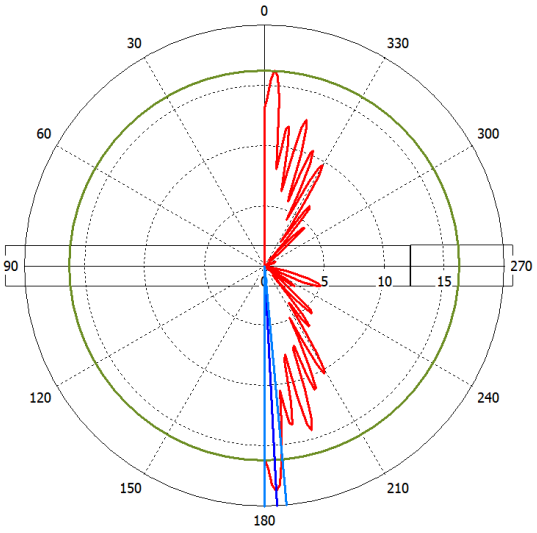

Figure 28: f = 1.2GHz, Main lobe magnitude = 18.8dBm^2, main lobe direction = 183°, Angular width (3dB) = 5.2°, Side lobe level = -2.5dB.

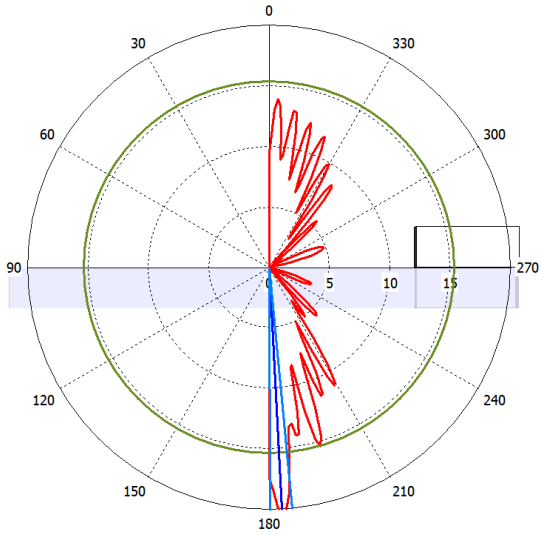

Figure 29: f = 1.2GHz, Main lobe magnitude = 20.5dBm^2, main lobe direction = 183°, Angular width (3dB) = 5.3°, Side lobe level = -5.1dB.

This may seem high, especially due to the smaller physical size of the simplified T-shape model as compared to the blade lengths of the conventional wind turbine measurements [64]. The radar cross section here appears higher due to the

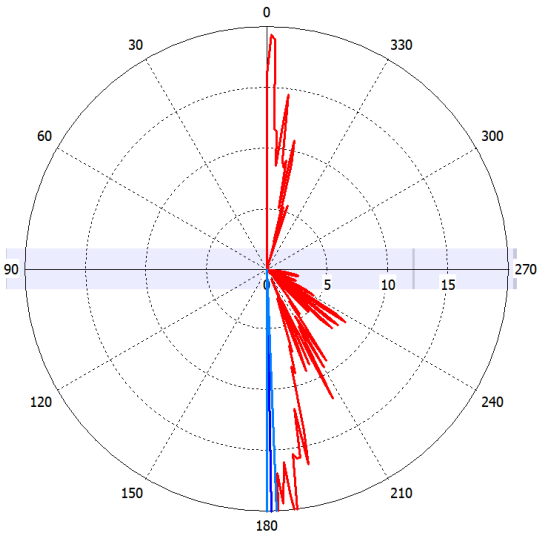

Figure 30: f = 2.8GHz, Main lobe magnitude = 26.6dBm^2, main lobe direction = 181°, Angular width (3dB) = 2.2°, Side lobe level = -5dB.

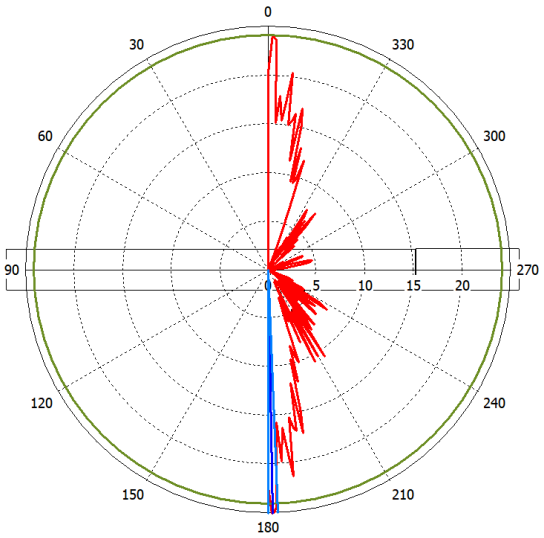

Figure 31: f = 2.8GHz, Main lobe magnitude = 25.5dBm^2, main lobe direction = 181°, Angular width (3dB) = 2.2°, Side lobe level = -1.3dB.

horizontal polarization as opposed to the vertical polarization used in the cited work. A simulation was attempted using circular polarization, however unfortunately this simulation failed with an unknown error code initially, so results are

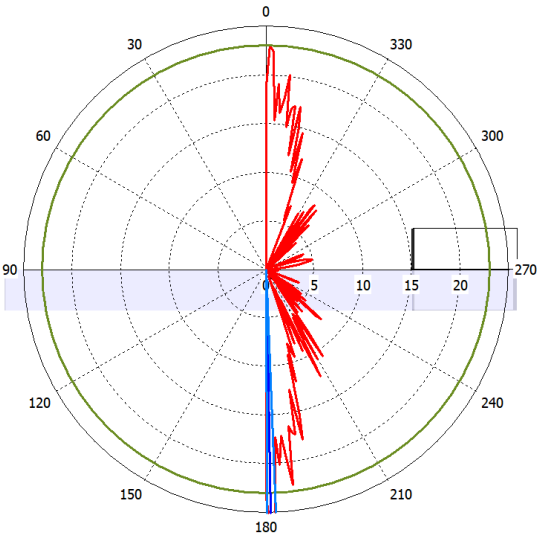

Figure 32: f = 2.8GHz, Main lobe magnitude = 26.8dBm^2, main lobe direction = 181°, Angular width (3dB) = 2.2°, Side lobe level = -3.7dB.

still pending the resolution of this issue. It is likely that the radar cross section of the Crossflow wind turbine will be lower than this conservative estimate, perhaps most of all because the Crossflow turbine is not a solid flat surface, but instead, the nacelle is comprised of a collection of curved surfaces with gaps between them. This will allow some of the radiation to pass through, in addition to having the curved surfaces causing scattered reflections as opposed to the normal incident reflections generated by a large flat surface.

In summary, it can be seen from the test simulation results presented that when the structure is in the optical scattering size range, the shape of the structure is the primary driver of the RCS. The materials used and the specific size are of a lesser importance. This information will be used to inform the methodology used in the simulation of the full Crossflow turbine model and the HAWT model in the following chapter.

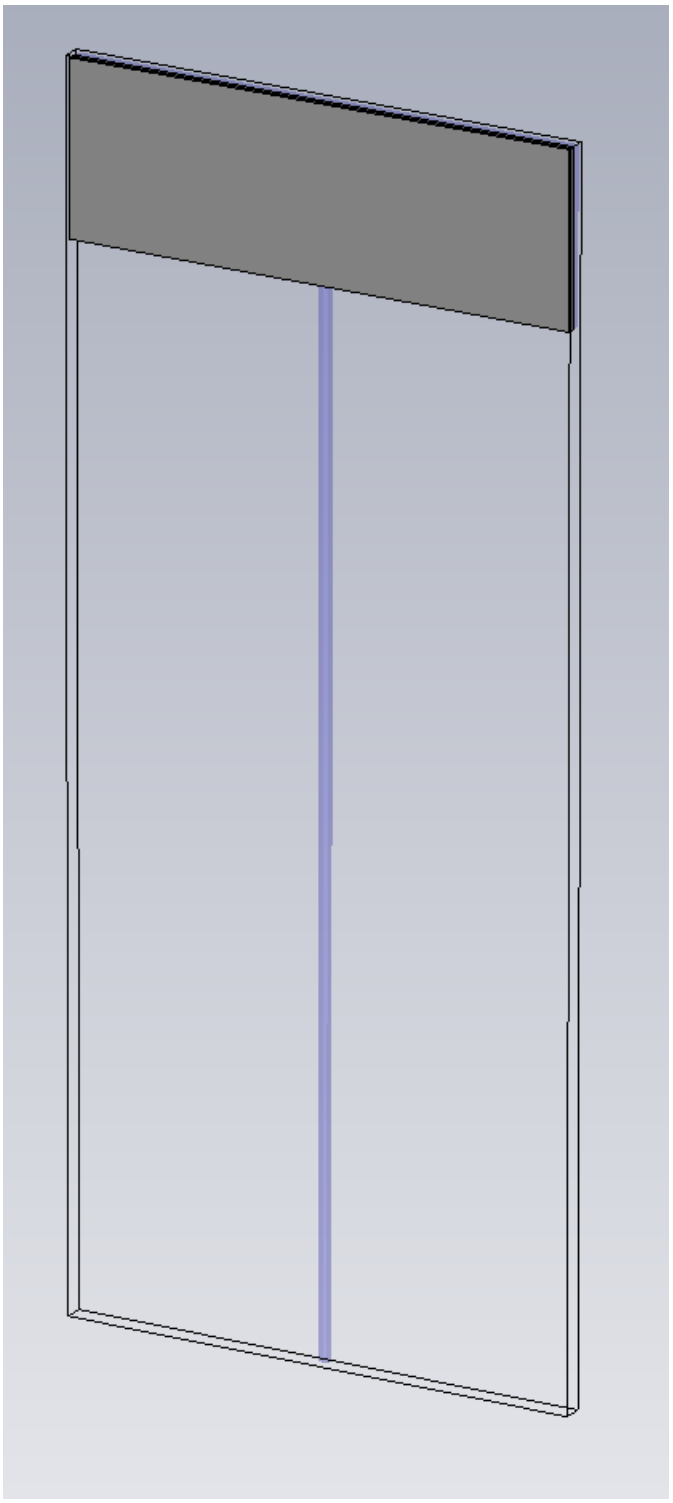

Figure 33: A perspective view of the large T-shaped simulation

4 Detailed Crossflow Turbine and HAWT Model Simulation

4.1 Simulation methodology - CAD model setup and meshing

In order to validate the proposed methodology, two wind turbine geometries were tested and compared - the Crossflow turbine, and a traditional HAWT geometry. The Crossflow turbine CAD model used for the simulation consisted of 150k faces, while the HAWT model was comparatively simpler at 30k faces.

Initially, a CAD file of the Crossflow wind turbine was requested and kindly provided by Crossflow Energy. This is a very large and detailed CAD file, totalling 22 megabytes in size. The CAD file consisted of the Crossflow wind turbine itself, together with all of the supporting structures that would be installed alongside the Crossflow turbine in a practical situation - namely the shipping container which would have housed the wind turbine during transit, a bank of two solar panels installed at the foot of the turbine, in addition to a small generator.

The CAD files of the Crossflow wind turbine were subsequently imported into the CST Microwave Suite, which is a software written by Dassault Systemes and is used for various electromagnetic and circuit simulations. It is an industry standard software, and there is much combined expertise with this software within the university, so it was a natural choice for the simulation of the turbine. It also has the capability of simulating extremely large objects, which is a necessity for this project.

Next, the Crossflow turbine CAD file was meshed in CST. Unfortunately there were many problems which had to be overcome, which were mostly caused by overlapping surfaces and edge inconsistencies, which CST had difficulty with, especially in the case that there were overlaps between parts of the model that had differing material definitions. This is because the Crossflow turbine file supplied was made up of several assemblies in Solidworks. In most cases, this was resolved by using a boolean add operation in order to make the two differing surfaces the

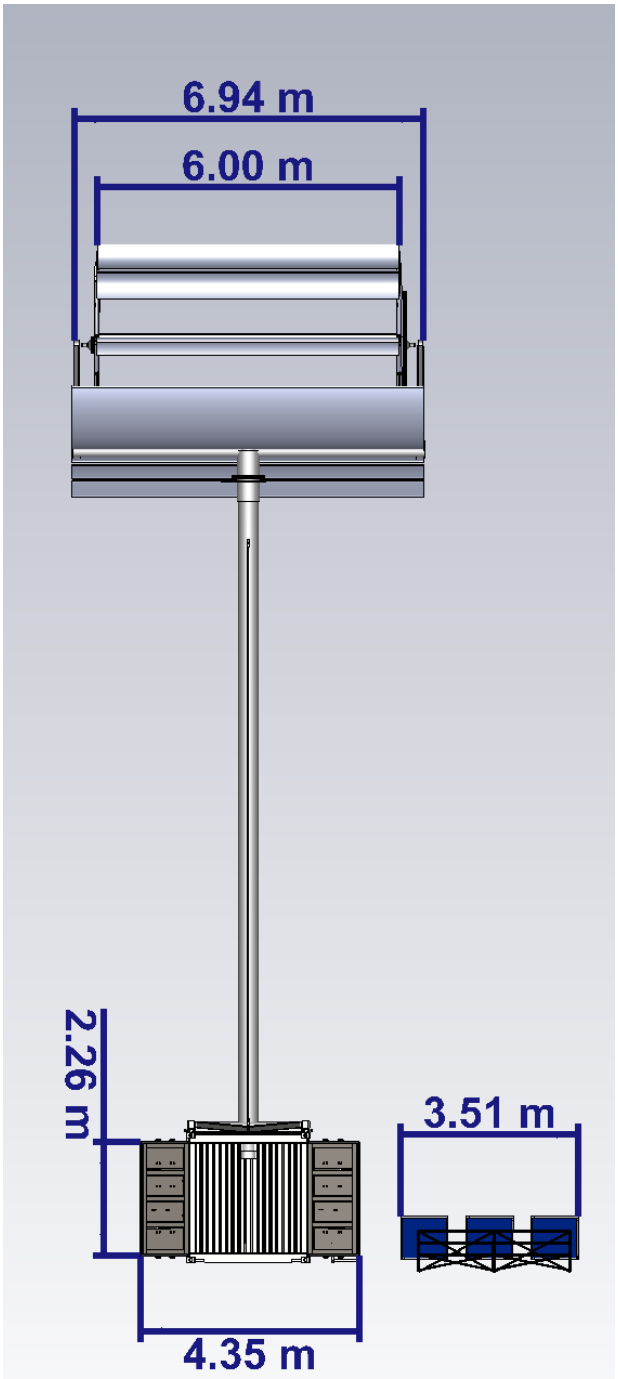

Figure 34: The front view of a Crossflow wind turbine installation CAD model

same object, thus removing the problems of meshing at the boundary. Unfortunately, this also means that the two parts now have to be defined as being made of the same material. This is something that would affect the radar cross section, and needs to be addressed appropriately in order for valid results to be produced. One way that this problem could be worked around is to define the new conjoined part as being made of a material having the higher reflectivity and therefore radar cross section. This would result in a more conservative result of a higher radar cross section.

In addition to this, initially there were some problems with importing the CAD file into CST. There were some surface issues, however the built in healing mechanisms within CST seemed to take care of the errors. Unfortunately because of the closed source and proprietary nature of the CST Microwave Suite, it is unknown exactly what changes were made during the healing process implemented by the CST Microwave Suite. This is also somewhat a concern when considering the validity of any results produced at all - due to the closed source and proprietary nature of the software package, it is impossible to verify the results, short of conducting practical testing. This is what will be performed in this case. In addition to this, the software has been widely used by other researchers within the lab for other similar applications, such as antenna simulations. In these cases, they have seen good agreement between the results produced by CST and the results obtained from practical testing performed on the manufactured antenna.

The first successful simulation that was run was only on the nacelle region of the Crossflow turbine, with the central gear ring pulley removed. This was because the gear ring pulley structure was composed of several sections which could not be boolean added, and the lack of this structure should not make a massive difference to the overall radar cross section, predominantly in the front view seen in Figure 34. In addition to this, a model had to be put together quickly for initial testing as there was only a limited amount of time on the trial license that was purchased in order to evaluate the suitability of the High Performance Computing (HPC) Wales cluster for the purposes of the project.

The model was meshed with the mesh settings that can be seen in Figure 38.

The quality measure applies to the tetrahedral mesh generator and describes how well the mesh cells relate to the shape of an ideal, equilateral tetrahedron. A higher value describes mesh cells most closely resembling a tetrahedron, while a lower quality value describes mesh cells which do not closely resemble an equilateral tetrahedron and may result in a negative impact on the convergence time of the simulation.

The models of the two turbines were simplified using Solidworks by removing all internal geometries as well as removing all unnecessary and very small features which increase the mesh size drastically without providing any additional accuracy or validity. An example of one of the features that was removed from the Cross-flow turbine is the toothed pulley ring, which can be seen in Fig. 39. The final meshes for both models were generated by the Xgtd from REMCOM, following the previously mentioned simplification and feature reduction using Solidworks.

Figure 35: An angled view of the deployed Crossflow turbine CAD file

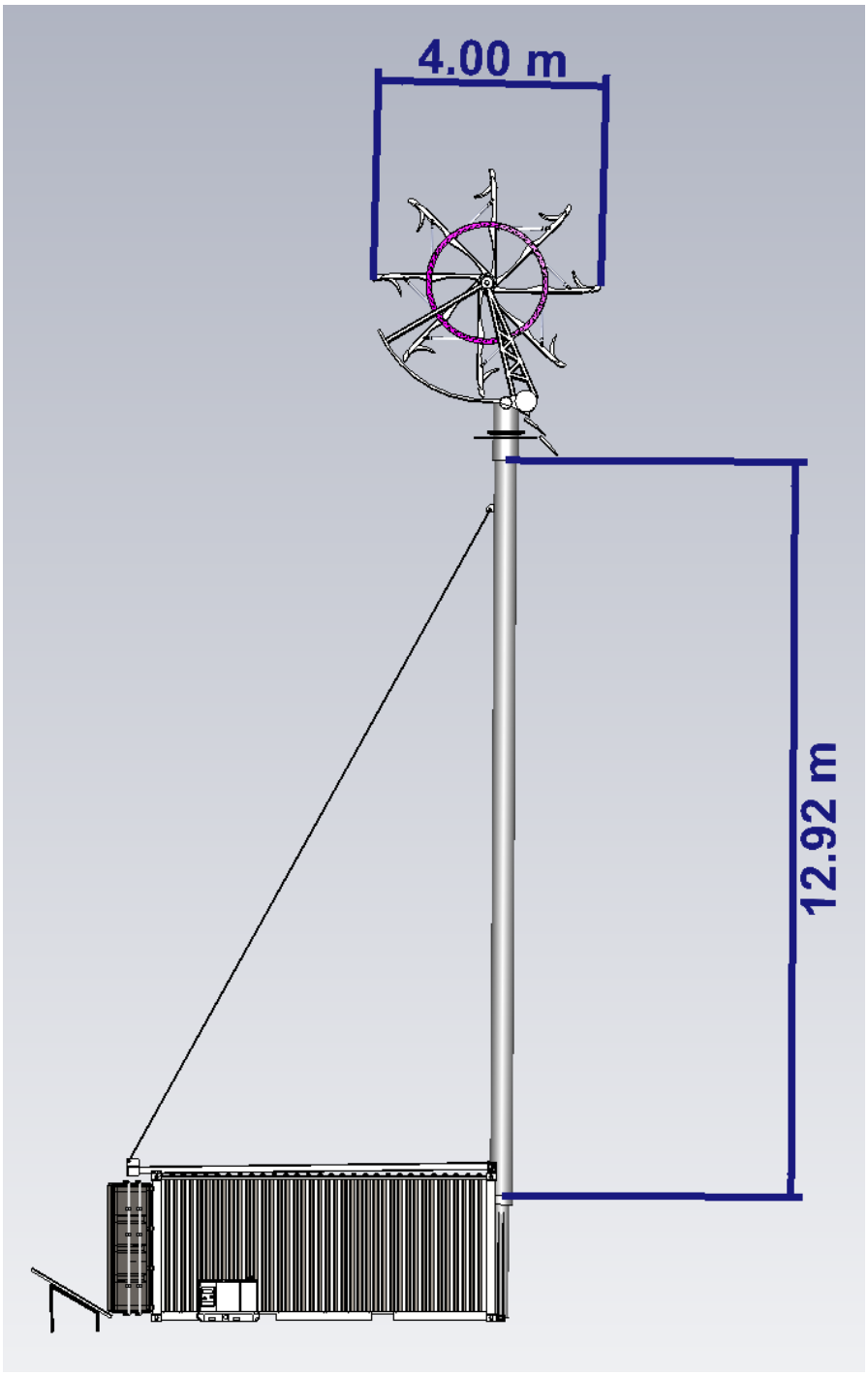

Figure 36: A side view of the deployed Crossflow turbine CAD file

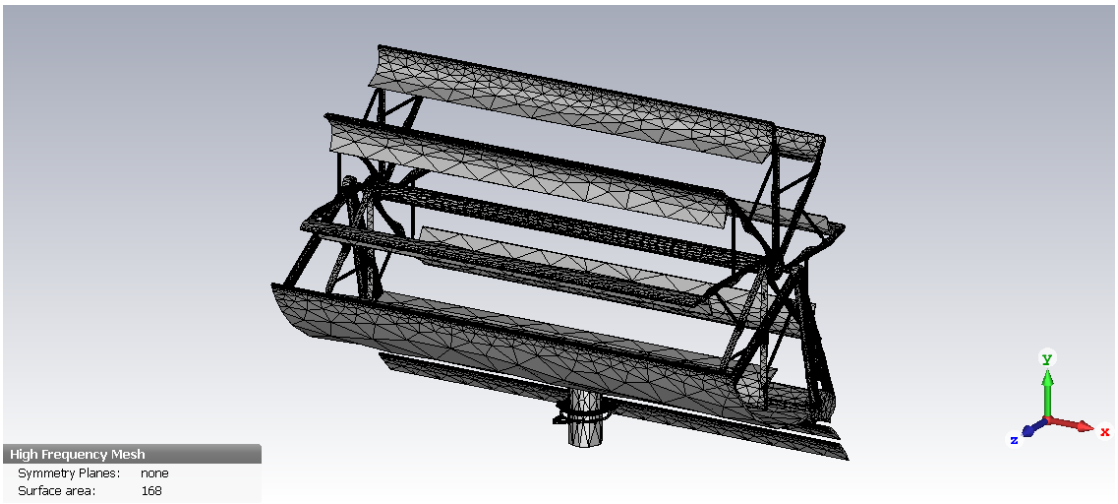

Figure 37: A view of the meshed nacelle without the gear ring pulley used in the first electromagnetic simulation of a Crossflow turbine part

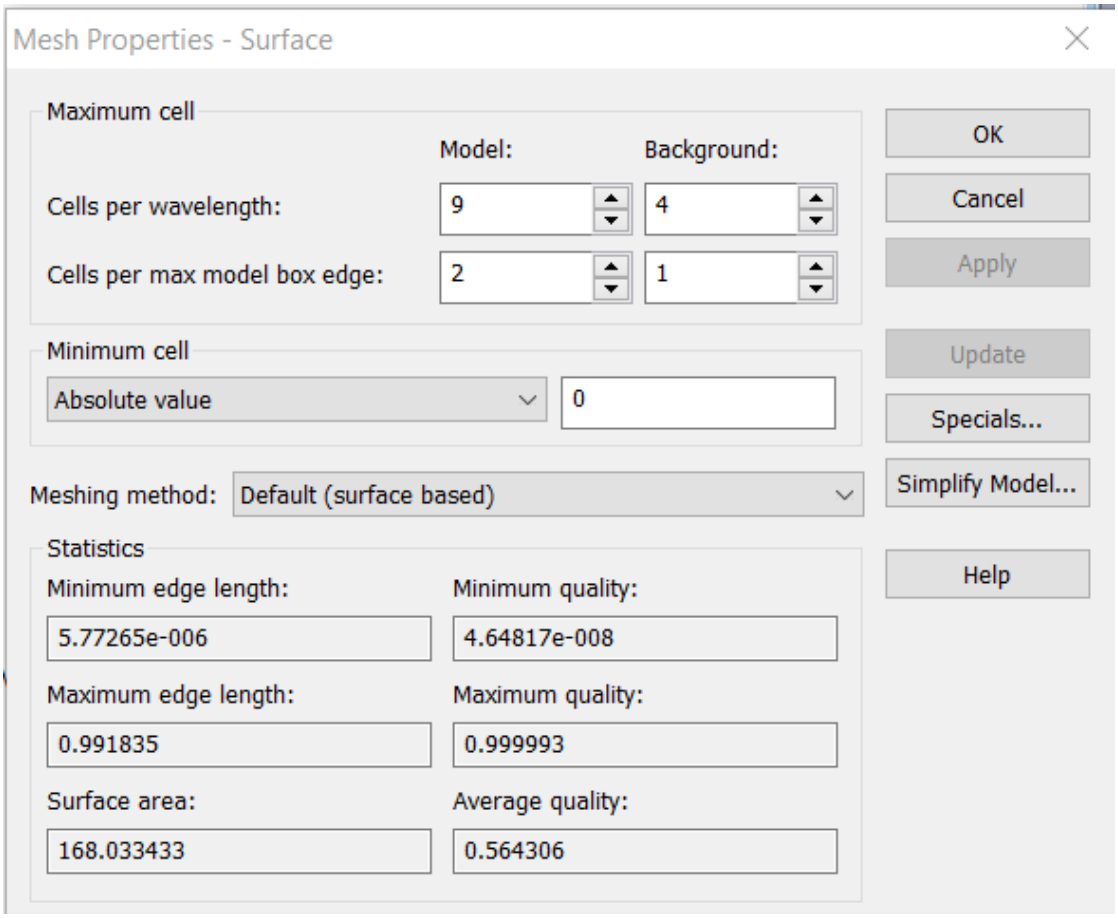

Figure 38: First Crossflow simulation mesh settings

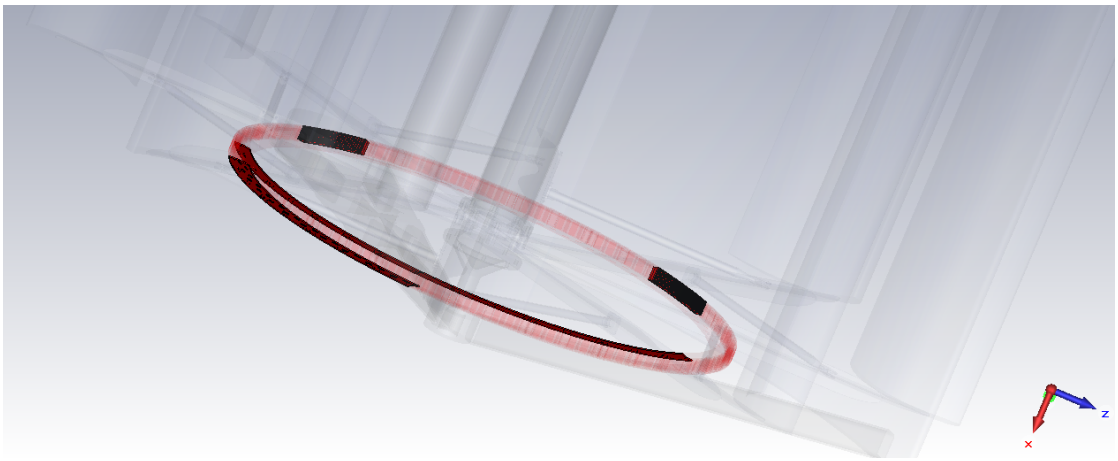

Figure 39: An image of the toothed pulley ring of the Crossflow turbine, which is one of the features that was removed using Solidworks prior to meshing the CAD model, as it increased the mesh cell count of the generated mesh significantly, without providing any additional accuracy or validity to the model.

4.2 Simulation methodology - Simulation parameter setup

Initially, when creating the simulation project, various parameters must first be defined within CST. One of these is the workflow suited to the simulation type. Under radar cross section, CST Microwave Suite offers the following workflows:

- Mono-static RCS
- Bi-static RCS
- Time-signal Radar
- Multi-static Radar
- Radar Range Profile
- RCS with Material Features

These are explained in more detail in the literature review.

The Crossflow turbine and HAWT models can be seen in Fig. 40. The HAWT model was obtained from a free CAD model repository [65]. The simulation results were obtained using the electromagnetic simulation software Xgtd from REMCOM [66]. This software uses the Physical Optics and Method of Equivalent Edge Currents (PO + MEC) methodology to simulate electrically large scenarios in a computationally efficient manner. Both models were simulated under illumination by linearly polarized (Phi and Theta polarized) plane waves at a frequency of 2.82 GHz, which is the main frequency used by primary surveillance radar (PSR) installations in civilian aviation radar applications.

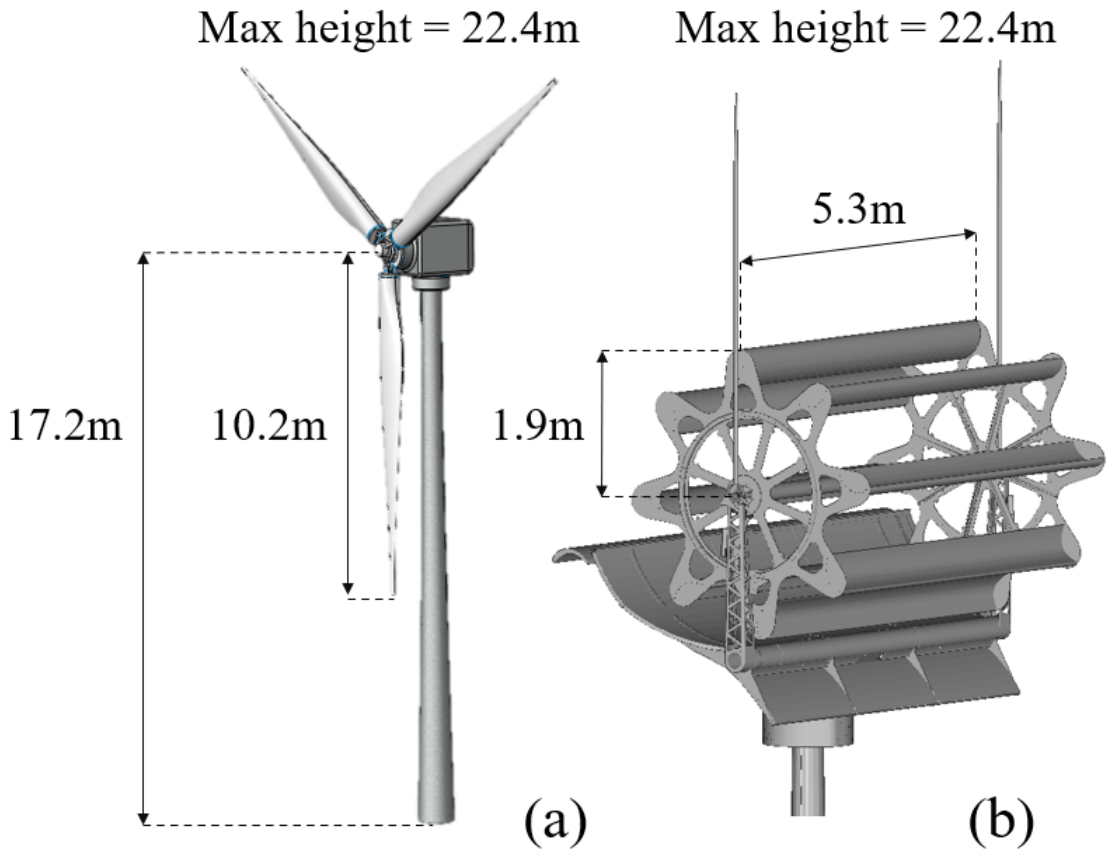

Figure 40: An image showing the CAD models of (a) The HAWT, and (b) The Crossflow turbine.

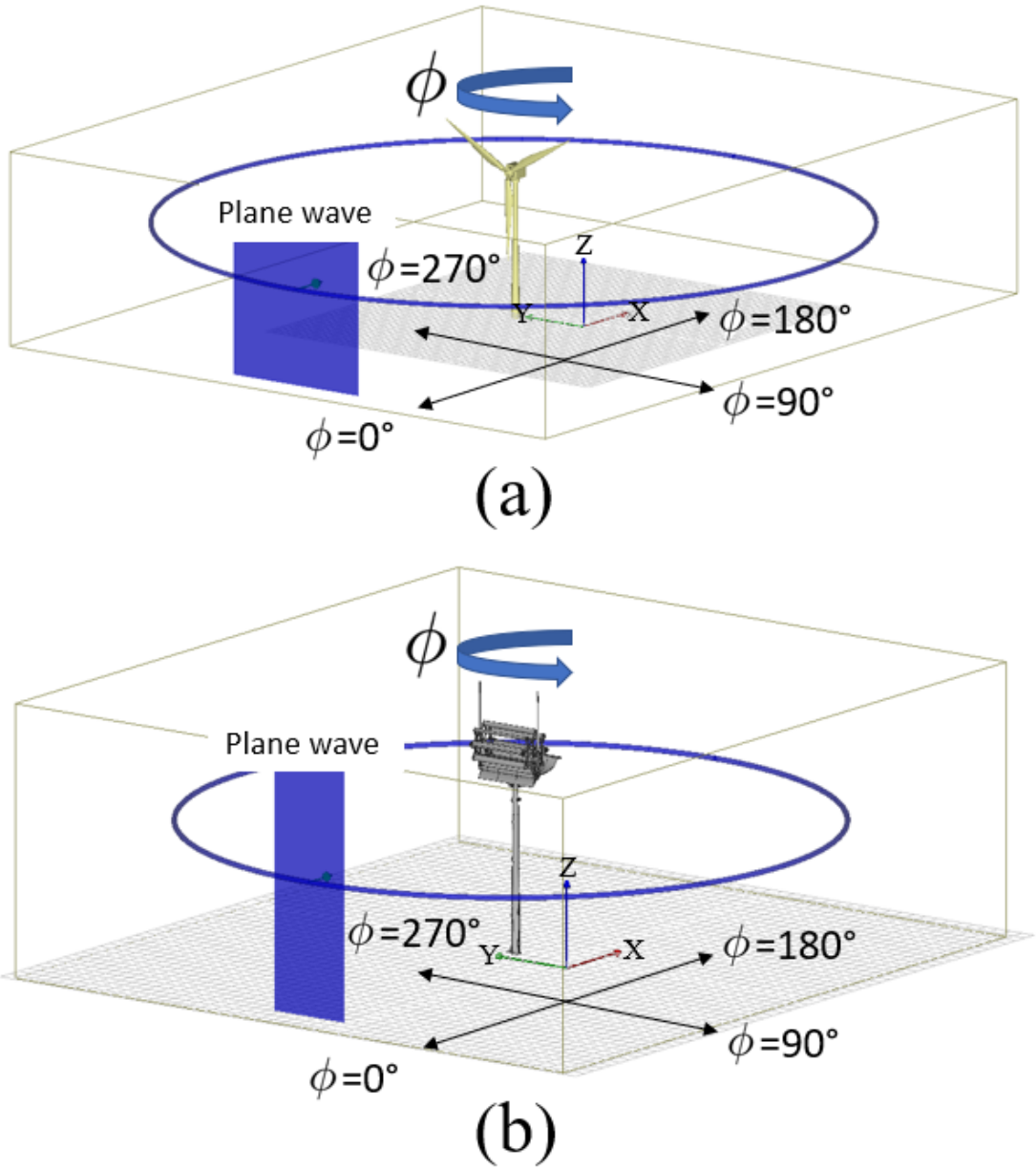

Figure 41: An image of the simulation scenario used for the RCS characterization of (a) the HAWT, (b) the Crossflow turbine. Simulation parameters: Frequency = 2.82GHz, Illumination method: Plane wave. Waveform type: Gaussian/chirp. Boundary conditions: Open (non-reflective).

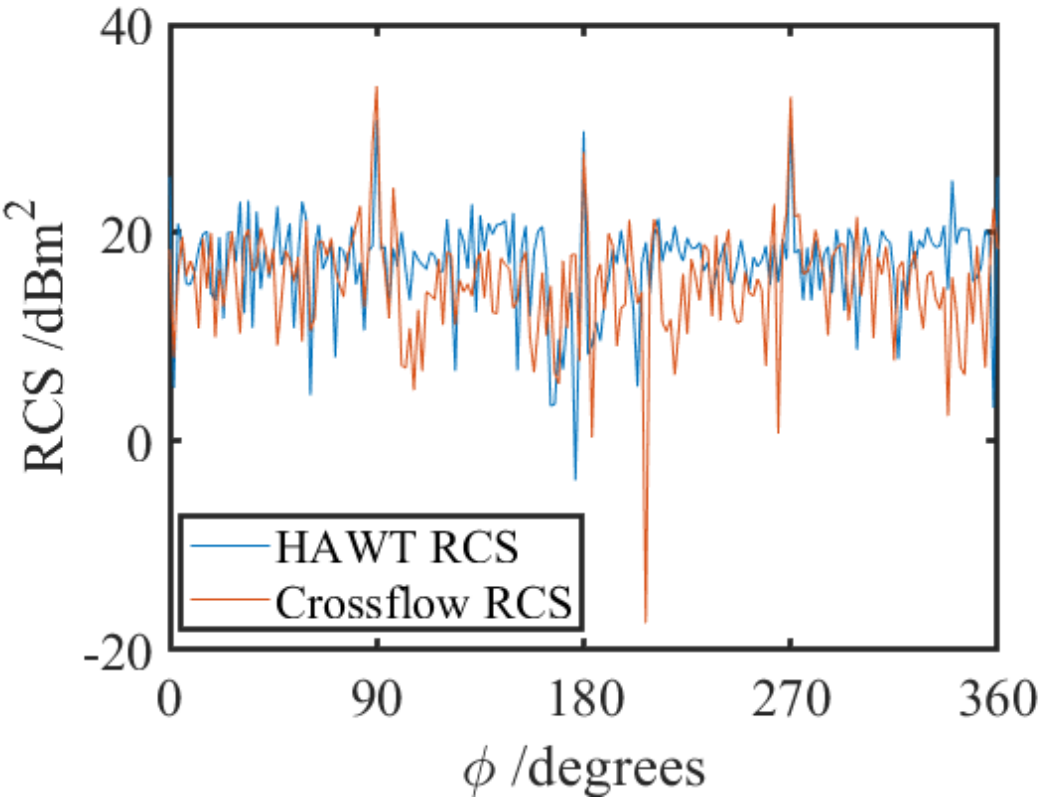

Figure 42: A comparison of the HAWT and Crossflow monostatic RCSs, when illuminated by a Phi polarized plane wave.

4.3 Results and Analysis

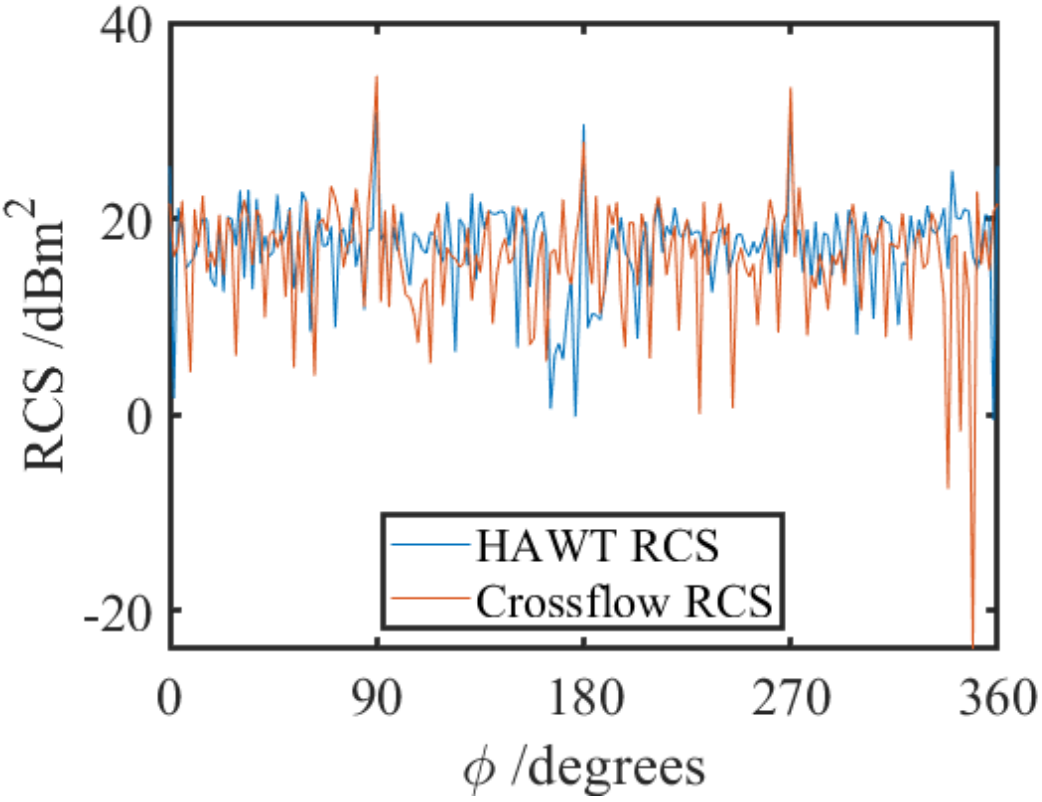

Figure 43: A comparison of the HAWT and Crossflow monostatic RCSs, when illuminated by a Theta polarized plane wave.

The simulation scenarios for both turbines, including the plane waves used to illuminate the respective structures can be seen in Fig. 41 (a) and (b). The plane waves used to illuminate the two structures are of different areas, in order to ensure that the entire frontal area of each geometry is illuminated while optimizing the simulation process.

Comparison plots with the RCS results of both the Crossflow turbine and HAWT under each polarization can be seen in Figs. 42, 43. It can be seen that the obtained HAWT RCS results are similar to those presented in the literature [67], [68], [69], [70]. From the presented simulation results, it can be seen that the

Crossflow turbine exhibits lower average monostatic RCS values when compared with a traditional HAWT geometry, while the peak RCS for both turbines occurs at the same aspect angles ($\phi = 90°$ and $\phi = 270°$).

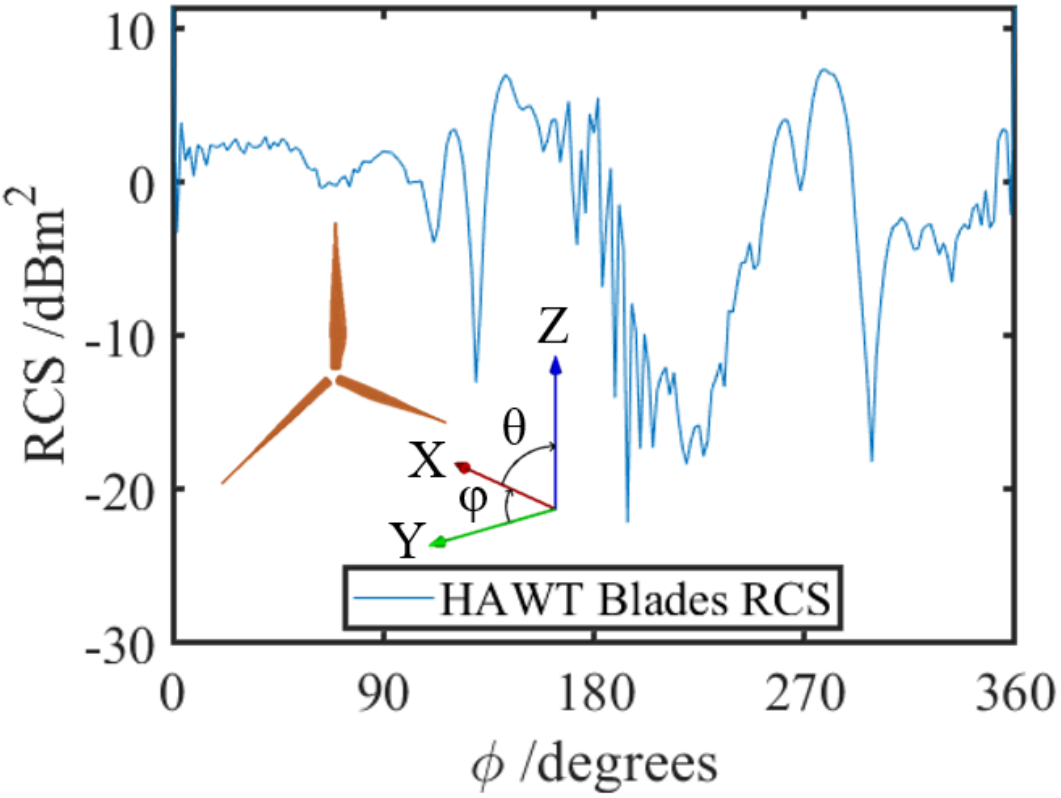

Figure 44: A plot showing the simulated RCS of only the blades of the horizontal axis wind turbine under Phi Polarization.

This work shows and confirms that the RCS of an object in the optical scattering region is dictated strongly by the geometry of the object. A minima in the RCS of the HAWT at approximately $\phi = 175°$ can be observed in Fig. 42 and 43. This minima can be attributed to the reflectivity characteristics and geometry of the HAWT blades.

This is evidenced in the results of the RCS simulation that was conducted of only the HAWT blades, which can be seen in Fig. 44. Here it can be seen that the local RCS minima occurs in the same place as it does in the RCS results obtained

Table 5: A table showing a comparison of the physical characteristics of the rotors of the two wind turbine models presented.

Physical characteristic	HAWT	Crossflow turbine
No. of blades	3	8
Blade length	4m	6m, 1m rotor diameter
Maximum rotational speed	160rpm	60rpm
Maximum blade tip speed	67.02 m/s	6.28 m/s

Table 6: A table showing a comparison of the RCS metrics of the rotors of the two wind turbine models presented under Phi Polarization.

RCS Metric	HAWT	Crossflow turbine	Difference
Peak RCS	31.16 dBm^2	34.09 dBm^2	-2.93 dBm^2
Minimum RCS	-7.25 dBm^2	-17.41 dBm^2	10.16 dBm^2
Average RCS	17.15 dBm^2	14.54 dBm^2	2.61 dBm^2

Table 7: A table showing a comparison of the RCS metrics of the rotors of the two wind turbine models presented under Theta Polarization.

RCS Metric	HAWT	Crossflow turbine	Difference
Peak RCS	31.27 dBm^2	34.59 dBm^2	-3.32 dBm^2
Minimum RCS	-4.56 dBm^2	-23.89 dBm^2	19.33 dBm^2
Average RCS	17.15 dBm^2	15.47 dBm^2	1.68 dBm^2

from the simulation of the entire turbine. With regards to the maxima of the RCS of the two turbines, these can be attributed to the high reflectivity of the sides of the turbines, which is owed to the prominence of flat surfaces in these aspect angles. In carrying out this work and explaining the scattering mechanism that generates the observed RCS plots, clear advantages for the Crossflow turbine in terms of monostatic RCS and dynamic Doppler returns have been demonstrated, when compared with a HAWT design of comparable dimensions.

To elaborate on the simulation results presented here, two tables are presented comparing key RCS metrics belonging to the two turbines under different polarizations. It can be seen from Tables 6 and 7 that the Crossflow turbine exhibits lower minimum and mean RCS values than the HAWT under both polarizations tested, however it can be seen that the HAWT exhibits a slightly lower peak RCS than the Crossflow turbine.

As discussed previously, Doppler spectrum contamination is one of the major contributors to the interference generated by wind turbines in the vicinity of radar installations. In order to quantify the magnitude of the Doppler returns from the two wind turbine models presented, analytical work was carried out in MATLAB using the Phased Array System Toolbox [71]. The Doppler returns from the two wind turbine models were calculated at the point of maximum rotational velocity, representing a worst case scenario. Table 5 shows a comparison of the physical characteristics of the two wind turbines. It can be seen from the table that the Crossflow turbine has a lower peak rotational speed and shorter blades, resulting in a significantly lower maximum blade tip speed as compared with the HAWT. This lower peak blade tip speed corresponds to a much lower observed peak Doppler shift. The Time-Doppler plots for the case of the HAWT and for the Crossflow turbine are shown in Fig. 45.

In order to provide a greater number of points of comparison between the Crossflow turbine and HAWT, heat maps were created showing the RCS of both turbine models for a variety of different θ and ϕ aspect angle combinations.

The dimensions of the Crossflow turbine CAD model used can be seen in Table. 9.

Table 8: A table showing the parameters of the two different chirp profiles used during testing.

Chirp Profile Characteristic characteristic	Chirp profile 1	Chirp profile 2
Start frequency	77GHz	77GHz
Frequency slope	29.982 MHz/μs	1.014 MHz/μs
Bandwidth	1798.92MHz	60.84MHz
ADC samples per chirp	256	256

Table 9: An table showing the x,y,z dimensions of the Crossflow turbine CAD model used.

	X	Y	Z
Maximum values	0.418591m	7.98384m	23.2784m
Minimum values	-3.80362m	0.864045	0.833659

The heat map showing the RCS for a variety of θ and ϕ aspect angles when the turbine is illuminated by a Theta Polarized plane wave can be seen in Fig. 46. A similar heat map can be seen in Fig. 47, however the RCS values presented in this heat map were obtained when the Crossflow turbine was illuminated by a ϕ - polarized plane wave.

Additionally, similar heat maps were produced for the HAWT. This work comprises a study of the effect of the tower height on the RCS of the geometry. In Fig. 48, the RCS heat map for the HAWT can be seen when it is illuminated by a θ - Polarized plane wave, in the case when it is given a 12m tall tower, and the nacelle and blades are scaled to achieve an 8m rotor/blade sweep diameter.

A heat map showing the RCS of the HAWT with a 12m tower and 8m rotor diameter when illuminated by a ϕ - polarized plane wave can be seen in Fig. 49.

In addition to the HAWT being simulated with dimensions such that the tower

is of height 8m and the swept blade area diameter is of size 8m, the HAWT was also scaled to be the same total height as the Crossflow turbine. This resulted in a blade length/swept area radius of 10.24m. The results of this simulation can be seen in Fig. 50 for the case of ϕ - polarization and 51 for the case of θ - polarization.

The main contributing factor to the variation of the RCS of the HAWT as ϕ varies is the geometry of the wind turbine blades, in addition to the nacelle of the HAWT. Both the blades and the nacelle present large reflective surfaces depending on the aspect angle. The reason why these geometries of these features are the main contributing factors that affect how the RCS of the turbine changes with aspect angle is that the size of the HAWT and its features place it in the optical scattering region, i.e. the smallest feature of the geometry is still very large compared to the wavelength of radiation used to illuminate the object. In the scattering region, the geometry and shape of the object under test is the deciding factor of its RCS as opposed to the absolute size of the object.

The contribution of the HAWT blades towards the total RCS of the HAWT has been demonstrated by the simulation of the RCS of the blades only. The blades were also simulated under different angles in order to show the effect of the angle of the blades on the RCS.

The simulation setup used in simulating the blades of the HAWT can be seen in Fig. 52 and 53.

In Fig. 54, the RCS of the HAWT blades only scaled to be the same size as they are in the full HAWT simulation can be seen, when they are each rotated by 60 degrees.

Similarly, in Fig. 55, the simulation setup used to obtain the RCS of the HAWT blades only when scaled to be the same size as they are in the full HAWT simulation can be seen, when they are not rotated at all, i.e. the trailing edge of the vertically downwards pointing wing is facing along the negative direction of the y-axis. This simulation results produced by this setup can be see in Fig. 56.

Continuing the analysis of how to various elements of the HAWT and their geometry contributes to the overall turbine RCS, with a view to demonstrating that the RCS of the object is a result of its geometry, I carried out simulations of

some of some of the other component structures of the HAWT. The nacelle of the model specifically contributes strongly to the overall RCS of the model at certain aspect angles, specifically at the aspect angles of $(\theta = 90°, \phi = 0°), (\theta = 90°, \phi = 90°), (\theta = 90°, \phi = 180°), and (\theta = 90°, \phi = 270°)$. A rectangular plot of the RCS of the nacelle only when scaled to the size that it would be when the HAWT is scaled to the same height as the Crossflow turbine can be seen in Fig. 57. Similarly, a heat map of the RCS of the nacelle only under ϕ - polarization can be seen in Fig. 58, and a heat map of the RCS of the nacelle only under θ - polarization can be seen in Fig. 59.

In a similar way, the HAWT nacelle and blades only (without the tower) were simulated. The simulation setup can be seen in Fig. 60. A rectangular plot of the nacelle and blades only can be seen in Fig. 61. Heat maps of the RCS of the nacelle and blades only under ϕ - and θ - polarization can be seen in Fig. 62 and 63 respectively.

As it was eventually decided that only the nacelle of the Crossflow turbine would be studied due to the limitations of the experimental setup, simulations were also carried out of the nacelle of the Crossflow turbine only. These results can be seen in Fig. 64 and 65.

For additional comparison data, simulations of the HAWT and Crossflow turbine models were also carried under the condition of illumination by LHCP radiation. In Fig. 66, a heat map of the RCS of the HAWT when illuminated by LHCP radiation can be seen. In Fig. 67, a heat map of the RCS of the Crossflow turbine when illuminated by LHCP radiation can be seen.

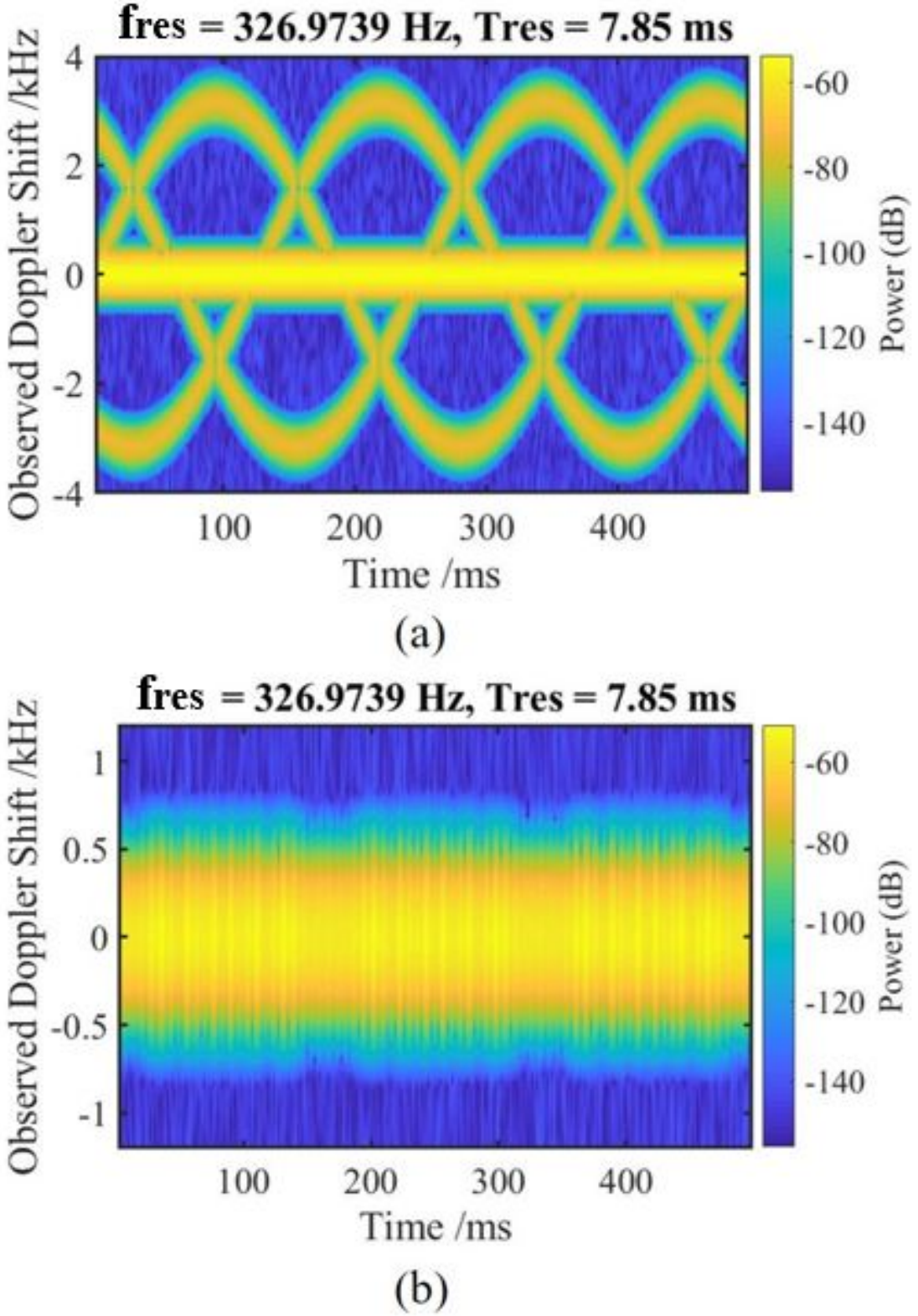

Figure 45: A time-Doppler plot showing the micro-Doppler returns calculated to be produced by the presented (a) horizontal-axis wind turbine model when it is rotating at its maximum speed of 160rpm, and (b) the Crossflow turbine model when it is rotating at its maximum speed of 60rpm.

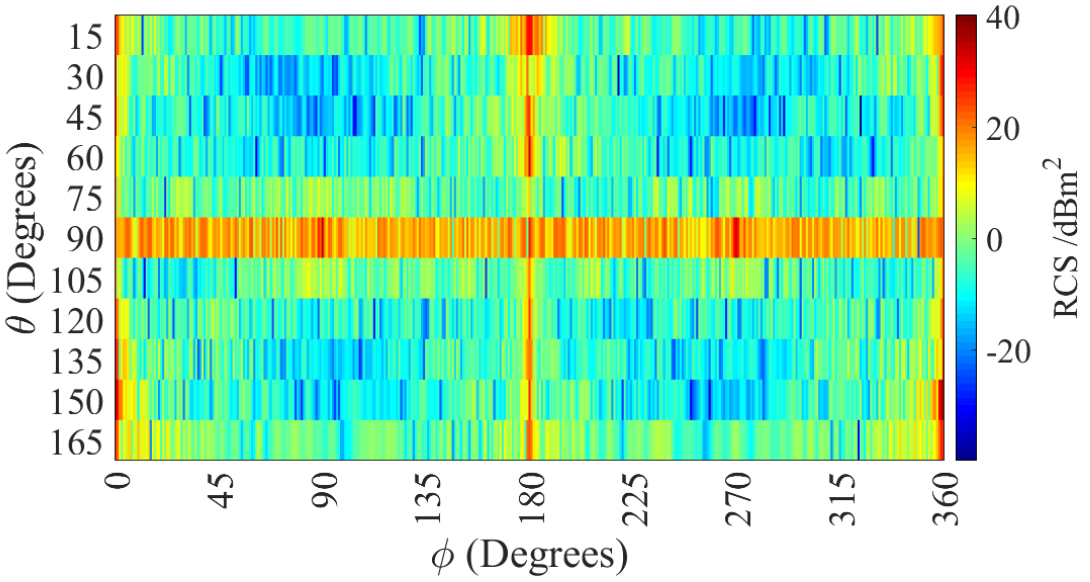

Figure 46: A heat map showing the RCS of the Crossflow turbine for a variety of θ and ϕ aspect angles when illuminated by a θ - polarized plane wave.

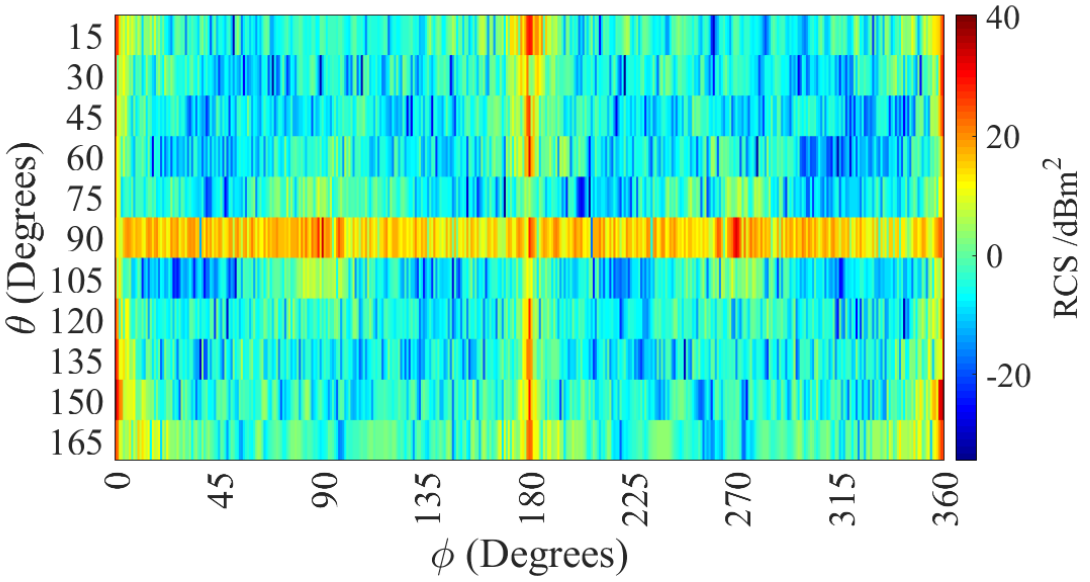

Figure 47: A heat map showing the RCS of the Crossflow turbine for a variety of θ and ϕ aspect angles when illuminated by a ϕ - polarized plane wave.

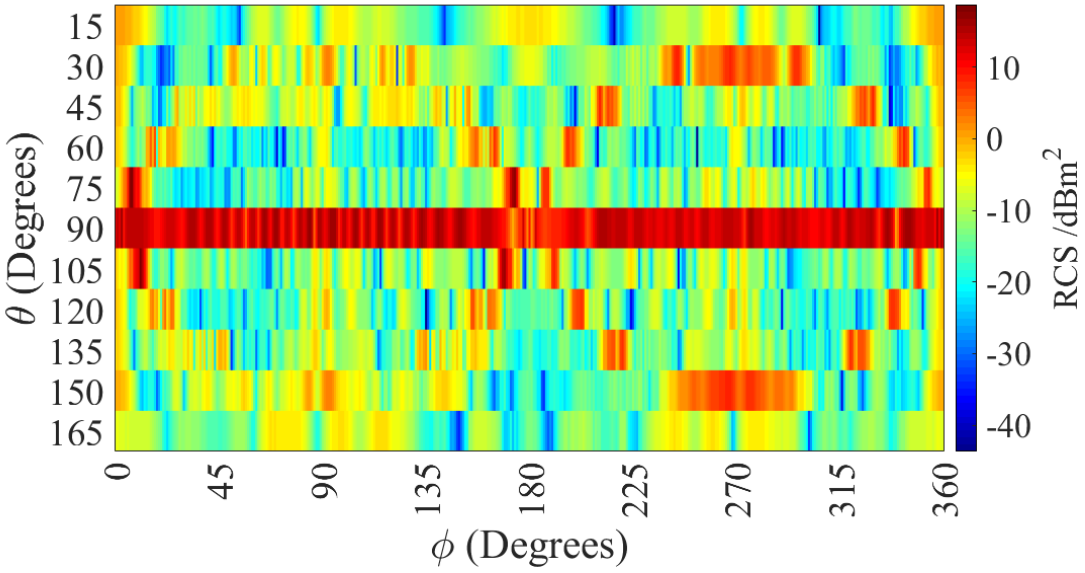

Figure 48: A heat map showing the RCS of the HAWT with a 12m tower and 8m rotor diameter for a variety of θ and ϕ aspect angles when illuminated by a θ - polarized plane wave.

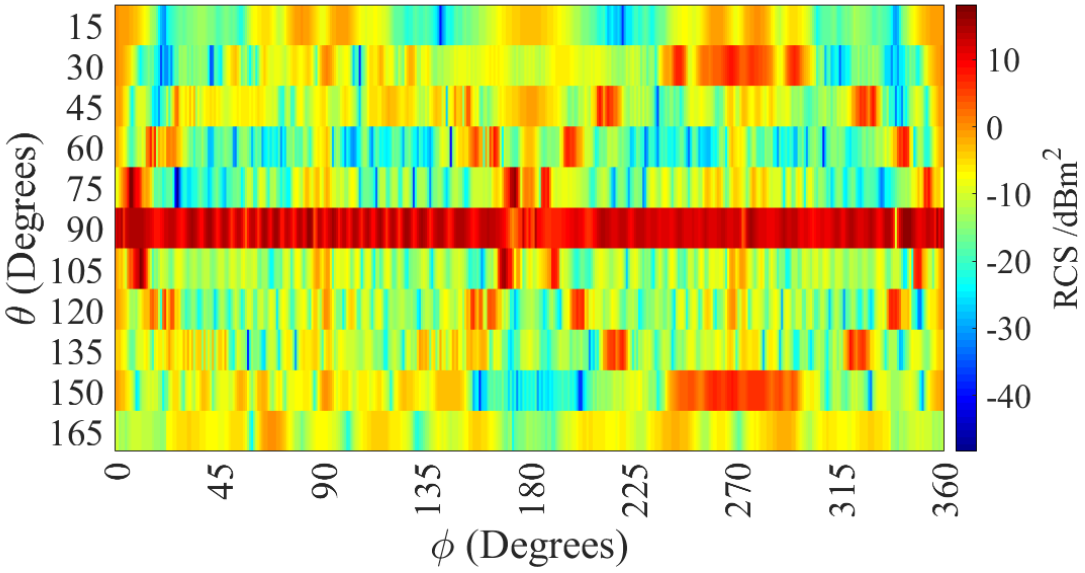

Figure 49: A heat map showing the RCS of the HAWT with a 12m tower and 8m rotor diameter for a variety of θ and ϕ aspect angles when illuminated by a ϕ - polarized plane wave.

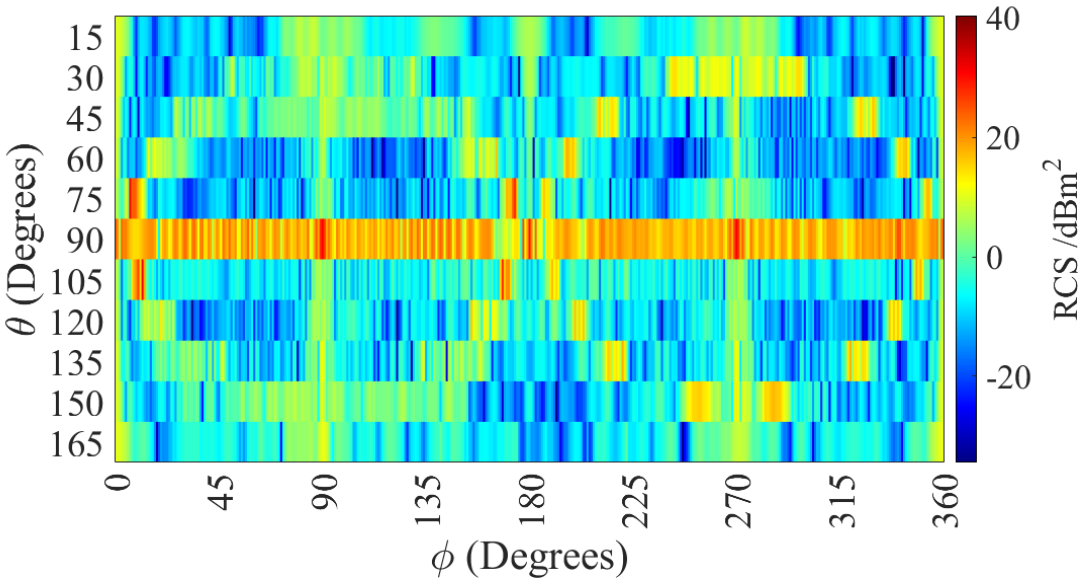

Figure 50: A heat map showing the RCS of the HAWT with a tower height of 17.2m and a rotor diameter of 10.24m for a variety of θ and ϕ aspect angles when illuminated by a ϕ - polarized plane wave. The turbine is scaled to be the same total height as the Crossflow turbine (22.4m).

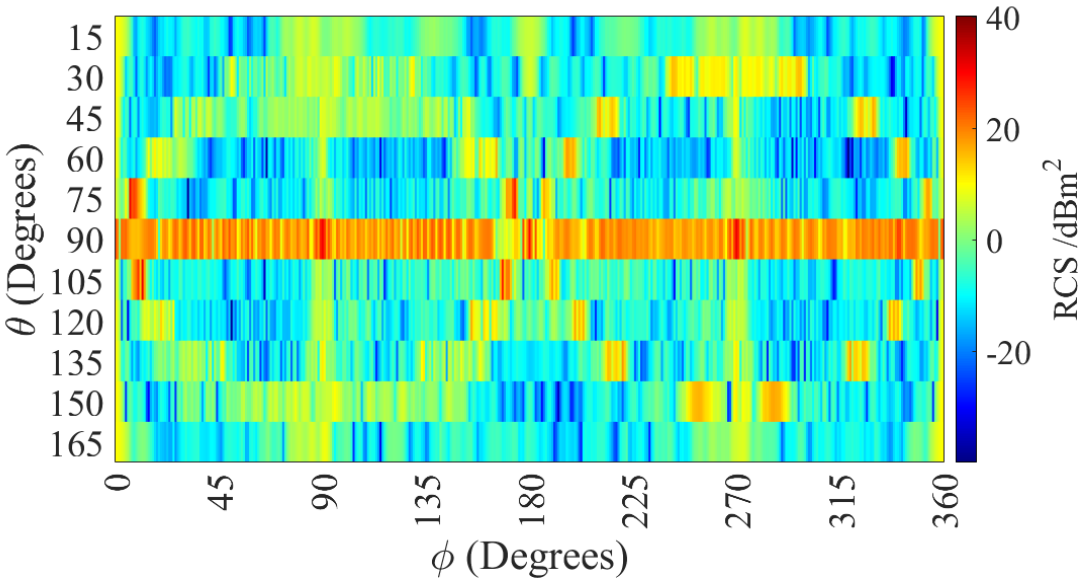

Figure 51: A heat map showing the RCS of the HAWT with a tower height of 17.2m and a rotor diameter of 10.24m for a variety of θ and ϕ aspect angles when illuminated by a θ - polarized plane wave. The turbine is scaled to be the same total height as the Crossflow turbine (22.4m).

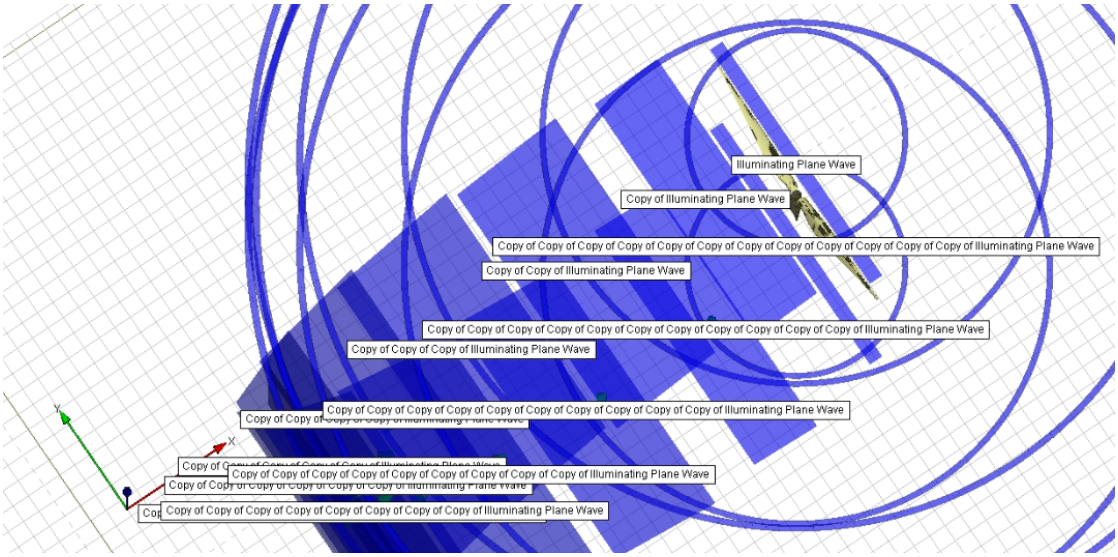

Figure 52: An image of the simulation setup used to characterize the RCS of the HAWT blades only.

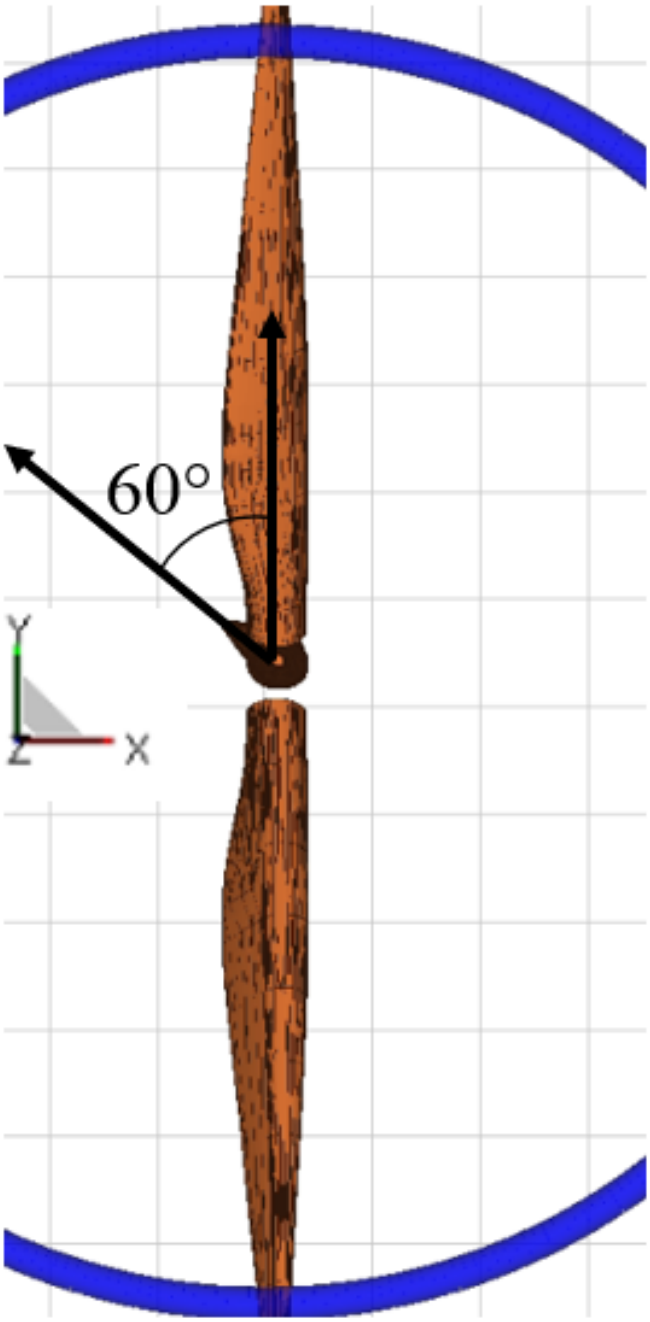

Figure 53: An image of the simulation setup used to characterize the RCS of the HAWT blades only, showing the 60 degree rotation of the HAWT blades.

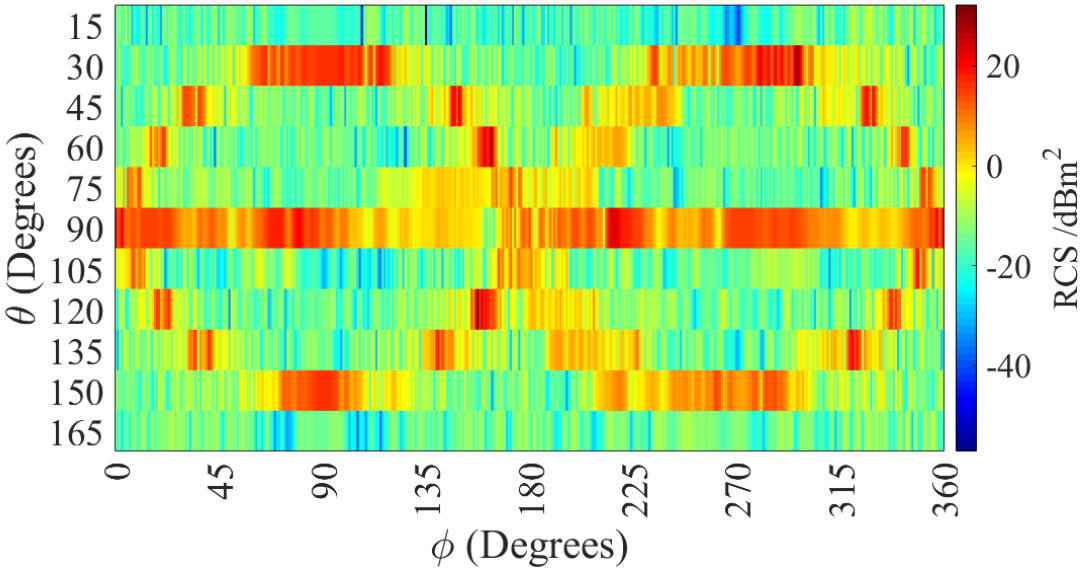

Figure 54: A heat map showing the RCS of the HAWT blades only when there is a 60 ° rotation applied to the blades for a variety of θ and ϕ aspect angles when illuminated by a θ - polarized plane wave.

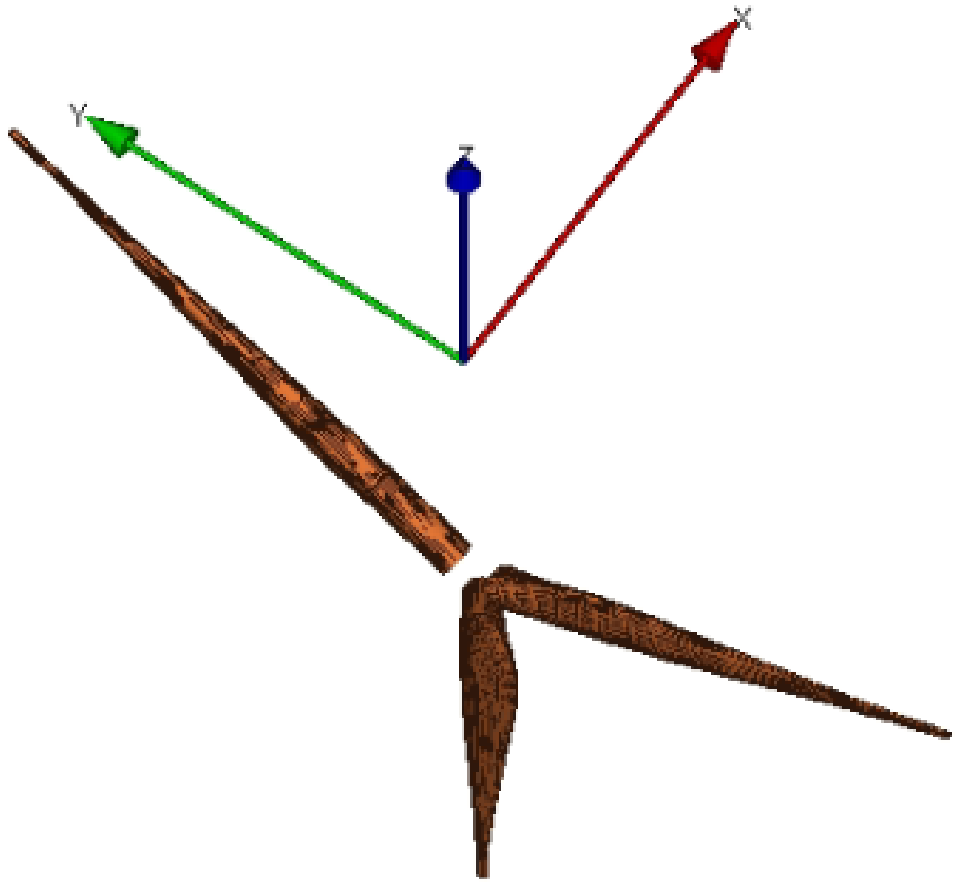

Figure 55: A heat map showing the RCS of the HAWT blades only when there is a 60 ° for a variety of θ and ϕ aspect angles when illuminated by a θ - polarized plane wave.

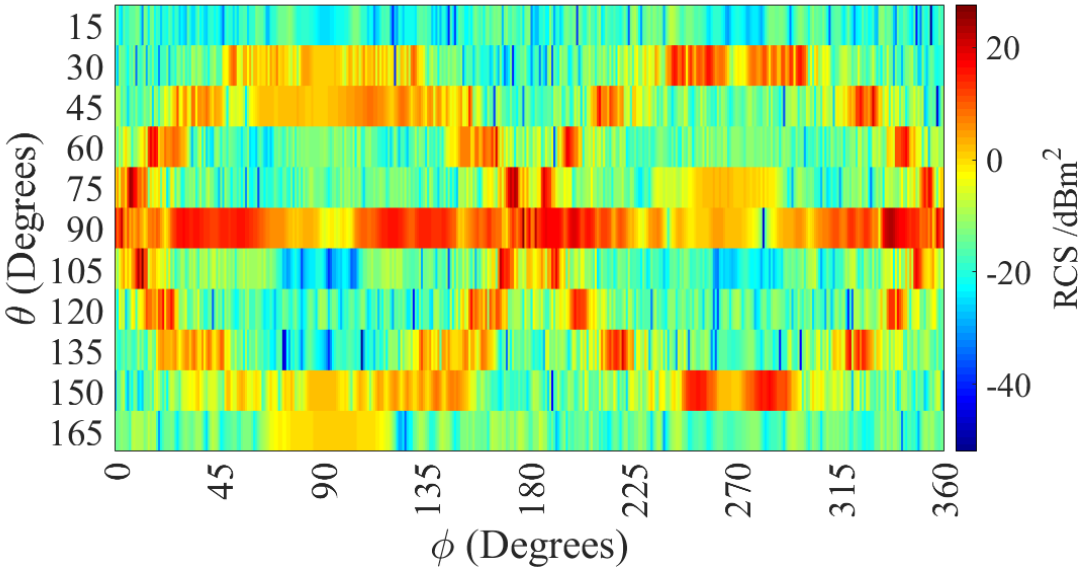

Figure 56: A heat map showing the RCS of the HAWT blades only when there is a 0 ° rotation applied to the blades for a variety of θ and ϕ aspect angles when illuminated by a θ - polarized plane wave.

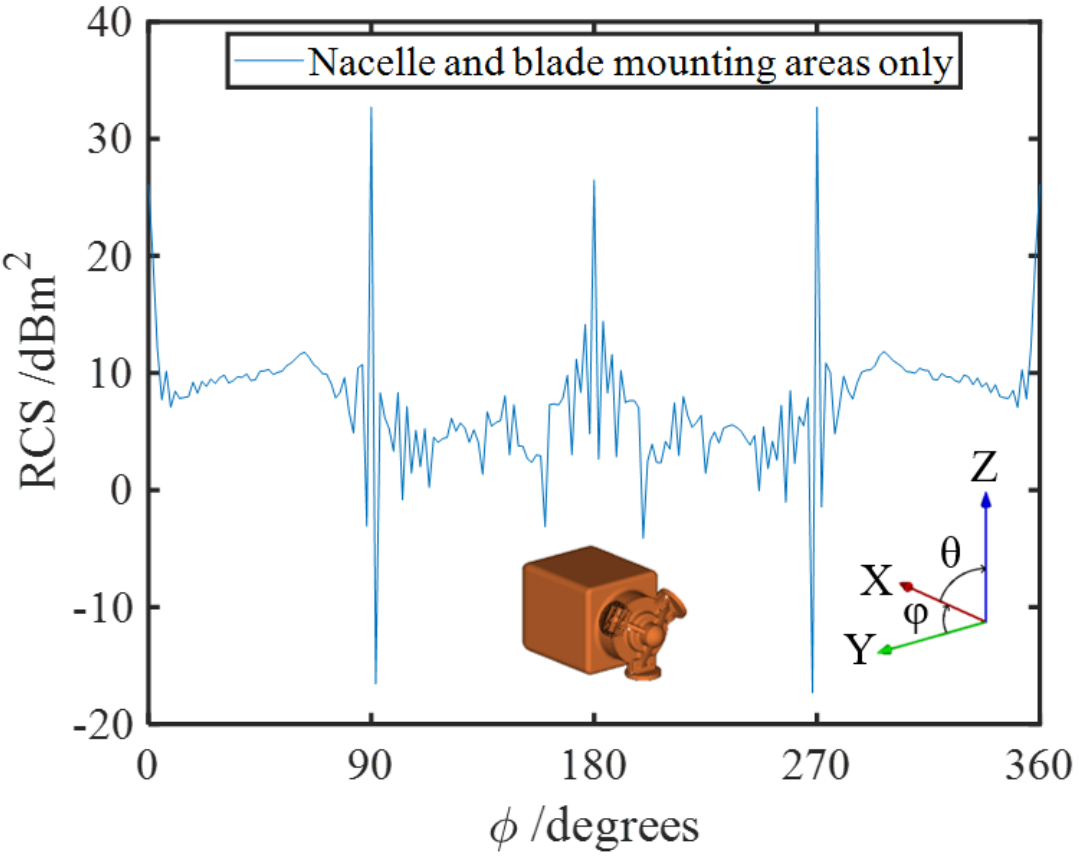

Figure 57: A rectangular plot of the RCS of the nacelle only under ϕ - polarization for all ϕ aspect angles at an aspect angle of $\theta = 90°$.

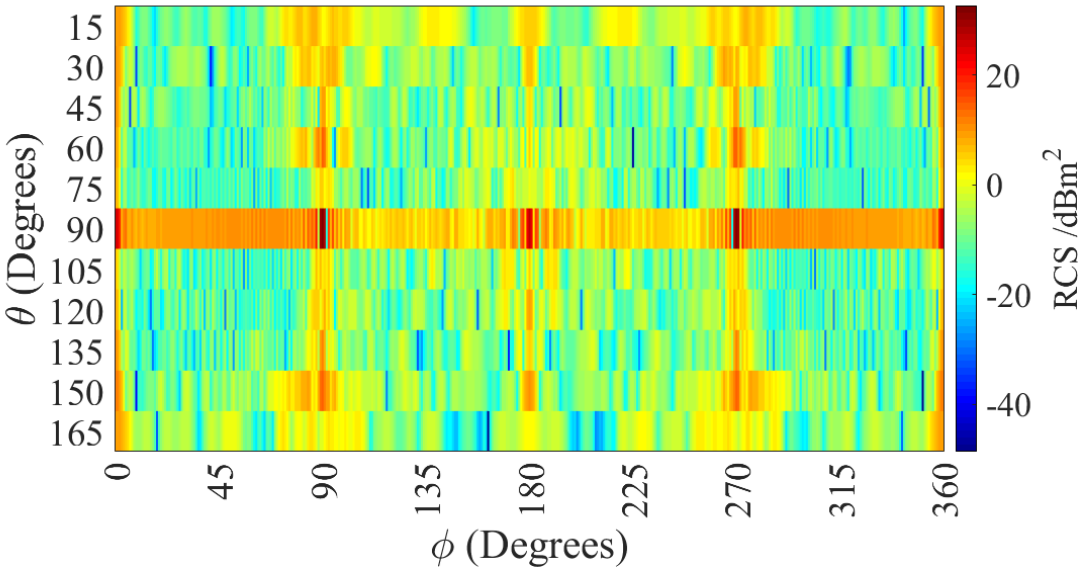

Figure 58: A heat map of the RCS of the nacelle of the HAWT only under ϕ polarization.

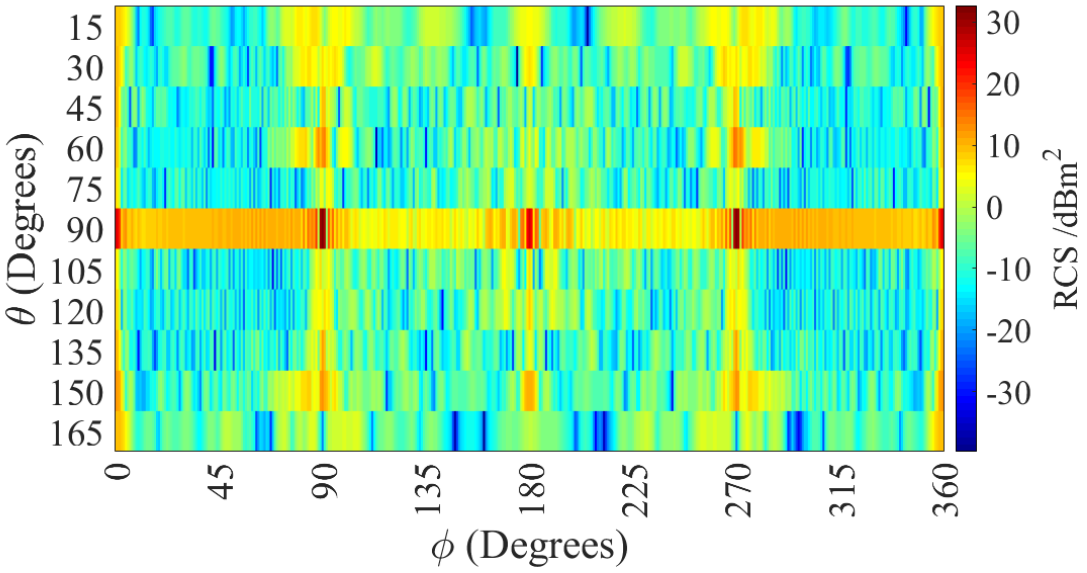

Figure 59: A heat map of the RCS of the nacelle of the HAWT only under θ polarization.

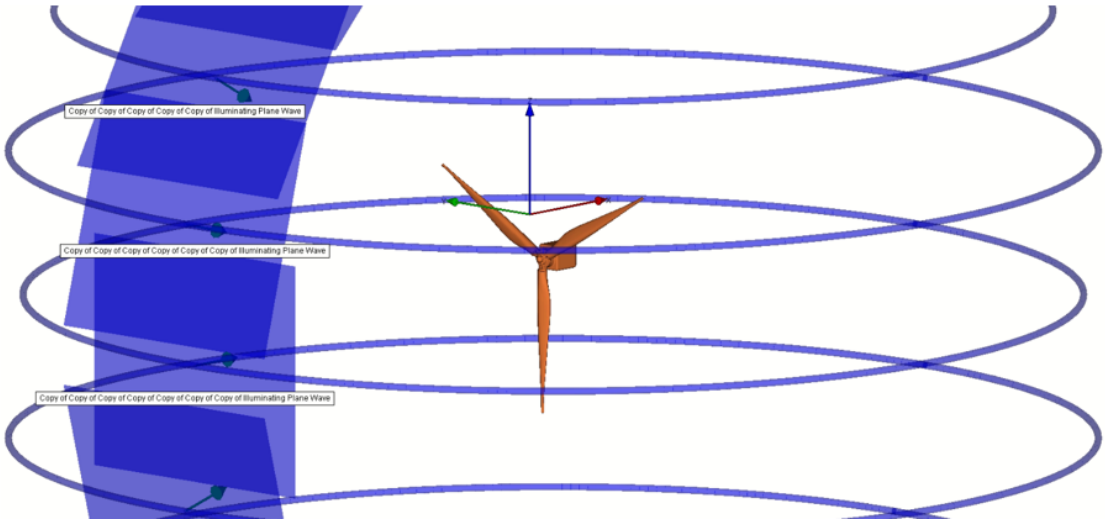

Figure 60: A diagram of the simulation setup used for the simulation of the HAWT nacelle and blades only (without the tower).

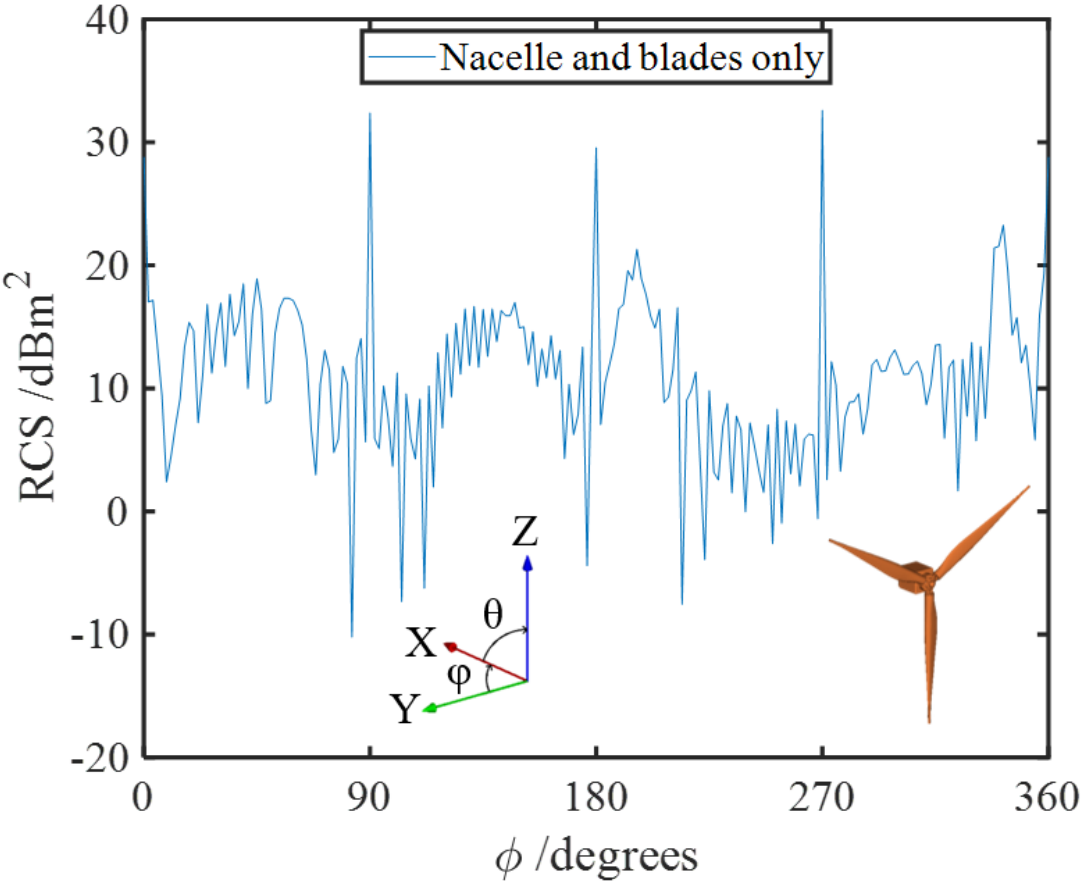

Figure 61: A rectangular plot of the RCS of the nacelle and blades only under ϕ - polarization for all ϕ aspect angles at an aspect angle of $\theta = 90°$.

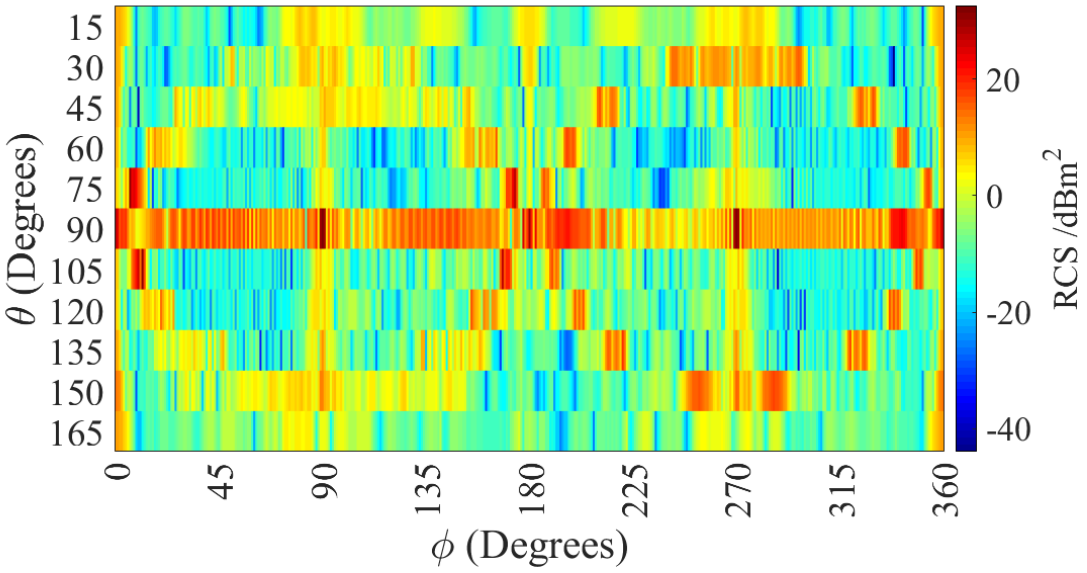

Figure 62: A heat map of the RCS of the nacelle and blades of the HAWT only under ϕ polarization.

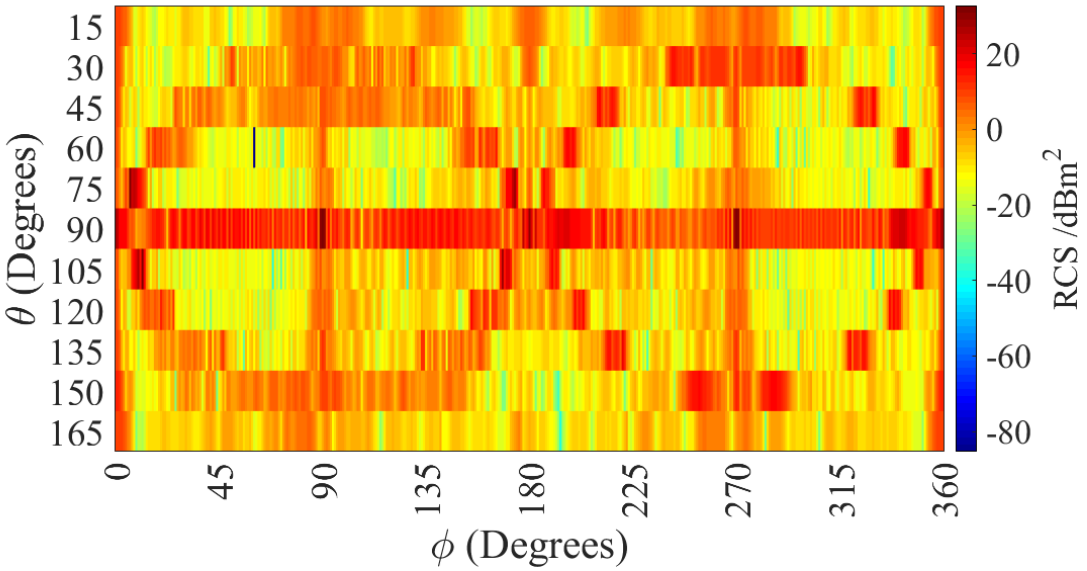

Figure 63: A heat map of the RCS of the nacelle and blades of the HAWT only under θ polarization.

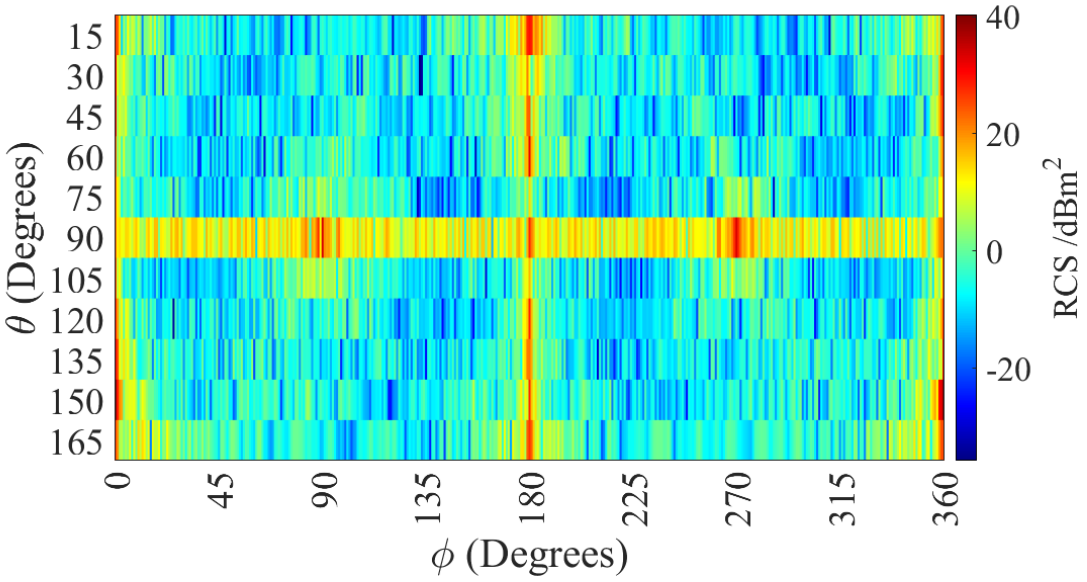

Figure 64: A heat map of the RCS of the nacelle of the Crossflow turbine only under ϕ polarization.

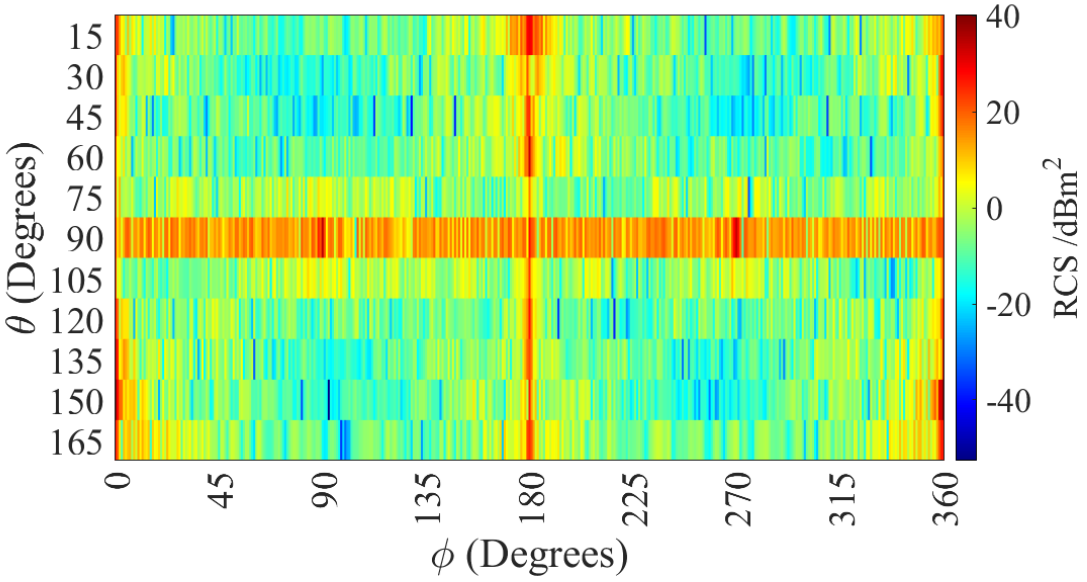

Figure 65: A heat map of the RCS of the nacelle of the Crossflow turbine only under θ polarization.

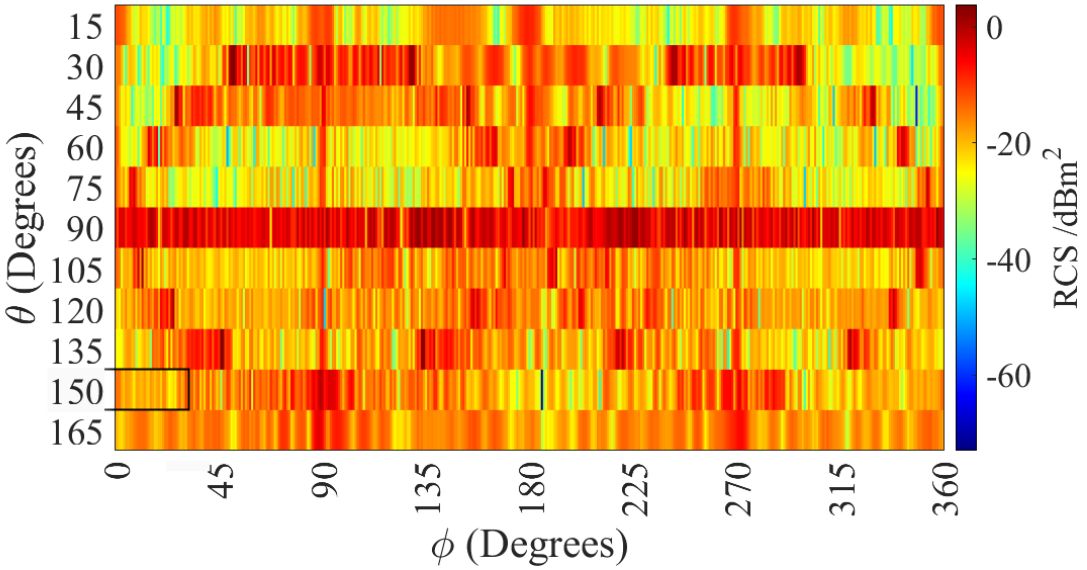

Figure 66: A heat map of the RCS of the HAWT under LHCP illumination.

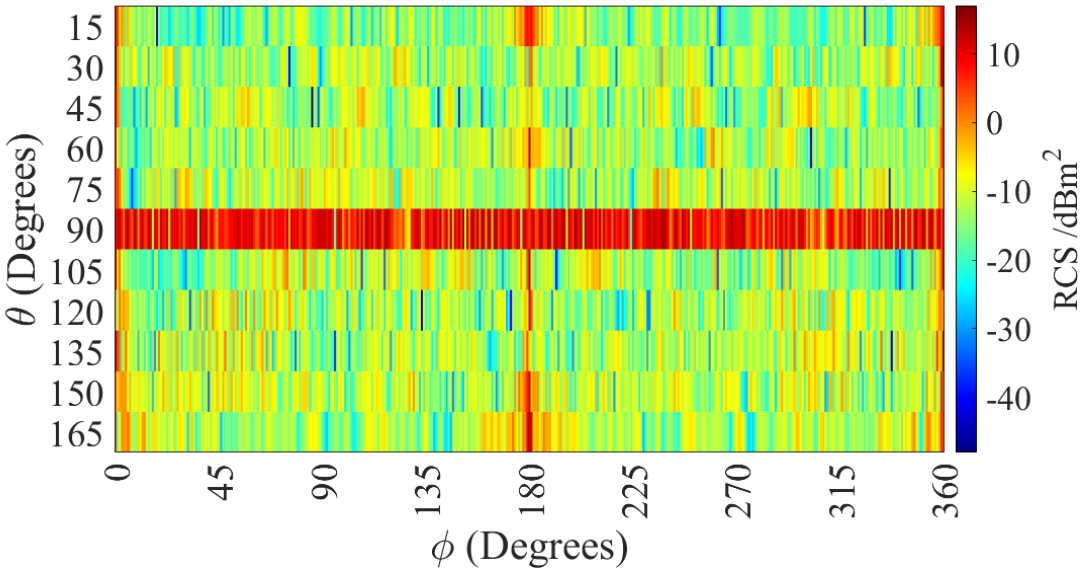

Figure 67: A heat map of the RCS of the Crossflow turbine under LHCP illumination.

5 Radar Cross Section Scale Model Measurements

As discussed previously, simulation results need to be verified experimentally, either via scale model or full scale measurements. In this work, scale model measurements have been chosen due to the comparatively lower cost and lower barriers to realization when compared with full scale measurements.

In the previous section, the first simulation results showing the RCS of the Crossflow turbine were presented, and compared against the RCS results of a commercially available HAWT model with a comparable rated power output. In this comparison, clear advantages for the Crossflow turbine are demonstrated.

In this chapter, a novel scale model RCS measurement technique is presented which utilizes millimeter-wave frequencies (76-81GHz) and has a number of advantages over techniques presented in the literature to date, in addition to being realized at a much lower cost [60] [70] [72] while maintaining similarly high levels of validity and accuracy. In addition to these advantages, the novel method was largely realized using only off-the-shelf, commercially available hardware, as opposed to bespoke hardware. This lowers the monetary barriers to replicating the system and to realizing high-accuracy and high-validity RCS measurements with limited resources. In addition, the system has physically small dimensions, removing the space constraints inherent in the use of certain other systems presented in the literature. The high frequencies used allow for both the range and scale model structure to have physically small dimensions. On the other hand, if the system functioned at a lower frequency of 10GHz, the size of the scale model used would have to be in the order of several meters, as the dimensions of the scale model must scale linearly with frequency. This poses practical difficulties and is an issue that is resolved by the high frequency method presented in this section. These unique features belonging to the system proposed in this chapter will enable the design and rapid prototyping of low-RCS structures for many applications.

5.1 Design of the aviation radar scatterometer system

5.1.1 Similitude theory

The theory states that in order to make accurate measurements of a scale model, the radio frequency used in order to ascertain the radar cross section should be increased by a quantity proportional to the decrease in size [21]. Using this theory, the frequencies that the radar test needs to cover can be calculated [21]:

$$\frac{D_M}{D_0} = \frac{\lambda_M}{\lambda_0}$$

where D_M is a dimension of the scale model, D_0 is the corresponding dimension of the full-scale model, λ_M is the wavelength used to illuminate the scale model, and λ_0 is the wavelength used to illuminate the full-scale structure.

Assuming that the finished Crossflow wind turbine will be in the order of 20m tall and 10m wide, and that that scale model needs to be proportionally ~50 times smaller while maintaining the same geometry, and assuming L an S band operation ($\tilde{2}$-4GHz), then the following wavelengths are calculated:

$$\lambda_M = \frac{D_M \lambda_0}{D_0}$$

$$\lambda_M = \frac{1}{50}\lambda_0$$

For a frequency of 4GHz:

$$\lambda_M = \frac{1}{200}0.15m = 0.0028m$$

and for a frequency of 2GHz:

$$\lambda_M = \frac{1}{200}0.3m = 0.0056m$$

For a frequency of 4GHz. These wavelengths correspond to frequencies of between 100 and 200GHz, which is not a practical solution as the majority of this range of frequencies are close to the Terahertz radiation range (0.3 to 3THz). However, it has been shown that there are still some similarities between the signatures, even when objects are illuminated with a much lower frequency [73] [17].

In a paper by Yamada *et al.* [26], it is again stated that the wavelength of the radiation used to illuminate the model target must be smaller than the frequency of interest by proportionally the same amount as the reduction in size of the object. This is difficult to achieve when the object of interest is a wind turbine with large dimensions.

5.1.2 Available off the shelf hardware

There exist available off the shelf solutions designed for the required frequency range of 100-200GHz. Automotive radar used for obstacle detection and avoidance already operates in the region of 77GHz, and demonstrates good long range operation at distances up to 250m for accurate detection of angular, distance, and velocity information about a target [74]. It has been shown that angular resolution in the region of 9°to 4.6° [74] is achievable. This is demonstrated using the following equations, the first of which shows the separability of distance objects, and the second of which showing the angular resolution achievable for a given wavelength, distance, and signal to noise ratio:

$$\Delta\psi = 1.22\frac{\lambda}{d}$$

$$\delta\psi = \frac{\Delta\psi}{\sqrt{2S/N}}$$

where ψ is the angular resolution, λ is the wavelength used, and d is the distance between the target and observer. This goes to show that it is practical to use frequencies in the range of 100-200GHz for scale model testing, and that frequencies in this range provide great enough resolution for a scale model of $\sim$1m height. In this study by Koehler *et al.*, a vector network analyzer (VNA), together with frequency converters is the set up used to produce the frequencies of 100-200GHz. The researchers also presented the use of an additional "hemispheric resonator" at 77GHz.

The researchers in this paper also examined the radar cross section of several scale model objects using a quasi-monostatic radar setup comprising of a vector network analyzer (VNA), frequency converters in order to reach the higher frequencies, in addition to antennas specifically designed to create a beam pattern with dimensions similar to the object of which the radar cross section is being measured. This approach likely increases the validity of the results, as a much greater majority of the transmitted power is being scattered by the object, as opposed to only a small portion of the wavefront actually coming into contact with the object in question.

In summary, building a bespoke scale model RCS characterization system in the mm-wave frequency range can be difficult, expensive, and time-consuming. However, there now exists commercially available, off-the-shelf hardware that can be used to construct a system that has many of the same advantages but can be constructed in a fraction of the time, with lower complexity, and for a much lower cost.

5.2 RCS Characterisation Method

The method proposed in this thesis builds on the existing literature describing the RCS characterization of scale model structures [27]. Crucially, several novel aspects are introduced which make this method distinct from and preferable to methodologies described in the literature to date. In this section, the mathematical background and theory of scale model radar cross section characterization and an explanation of how this was leveraged in this scenario is provided first. Secondly, the novel characteristics of the method in both approach and implementation are covered in detail. Finally, any issues and limitations that may arise from this unique approach are examined in detail, and the measures that have been taken to mitigate their impact on the validity and accuracy of the results obtained are provided.

A scale model RCS testing method via comparison is thoroughly described in [27]. Initially, the RCS of the object used as a reference must be defined via the radar equation form seen in Eq. 1.

$$\sigma_{Ref} = (4\pi)^3 R^4 \frac{P_{rRef}}{P_t} \frac{L}{G^2 \lambda^2}, \tag{1}$$

where σ_{Ref} is the RCS of the reference object in question, R is the distance between the observing radar system and the object under test, P_{rRef} is the power reflected from the object, P_t is the transmitted power from the observing radar system, G is the gain of the transmitting antenna, L is the overall loss in the system, and λ is the wavelength of operation. For the RCS of the object under test, the RCS equation form shown in Eq. 2 can be used.

$$\sigma_{Obj} = (4\pi)^3 R^4 \frac{P_{rObj}}{P_t} \frac{L}{G^2 \lambda^2}, \tag{2}$$

where P_{rObj} is the power received as a reflection from the object under test. The only difference in these two equations is the presence of the P_{rObj} term in Eq. 2 in place of the P_{rRef} term in Eq. 1. This is to denote that the equations concern different scattering objects. As many of the constants in the equations are the same, and antennas which exhibit identical gain are used for transmitting and receiving, the ratio between the RCS of the object under test and the reference object can be expressed as shown in Eq. 3.

$$\frac{\sigma_c}{\sigma_{Ref}} = \frac{(4\pi)^3 R^4 \frac{P_{rObj}}{P_t} \frac{L}{G^2 \lambda^2}}{(4\pi)^3 R^4 \frac{P_{rRef}}{P_t} \frac{L}{G^2 \lambda^2}} = \frac{P_{rObj}}{P_{rRef}}, \tag{3}$$

Eq. 4, an expression for the RCS of the model under test, can then be derived.

$$\sigma_{Obj} = \sigma_{Ref} \frac{P_{rObj}}{P_{rRef}} = \frac{4\pi a^4}{3\lambda^2} \frac{P_{rObj}}{P_{rRef}} \tag{4}$$

where a is the side length of the square reflector chosen as the reference object. There are a number of conditions which must be observed when performing a scale model RCS measurement [27] [75]:

$$R \geq 2 \frac{(D_a + D_{ob})^2}{\lambda}, \tag{5}$$

$$k \frac{D_{ob}}{2} \ > \ 10 \Rightarrow D_{ob} \ > \ \frac{10\lambda}{\pi} \ , \tag{6}$$

- Firstly, a minimum distance between the antenna and test subject is specified in Eq. 5 as a function of the largest antenna dimension (D_a) and the largest dimension of the object under test (D_{ob}).
- Secondly, the relationship between the largest dimension of the object under test (D_{ob}) and the wavelength displayed in Eq. 6 must be satisfied, thus ensuring that the object under test is in the optical scattering region.
- Thirdly, the measurements must be conducted in a low reflectivity environment.

In Eq. 6, $k = 2\pi/\lambda$ and is the wave number in free space. P_{rObj} is backcalculated using the raw ADC voltage input values [76] [77]. This is achieved using Eq. 7:

$$P_{rObj} = P_{ADC} - G_{LNA} - G_{Antenna} + FPL, \tag{7}$$

where G_{LNA} is the programmable LNA gain (30dB), $G_{Antenna}$ is the gain of the series fed patch antenna (10.5dBi), and FPL is the free-space path loss (45.9091dB over 0.2m).

The power incident on the scale model, P_{tObj}, can be found using Eq. 8:

$$P_{tObj} = P_{Tx} + G_{Antenna} - FPL, \tag{8}$$

where P_{Tx} is the maximum transmit power of the board (12dBm). The RCS in m^2 can then be calculated using Eq. 9:

$$\sigma = 4\pi R^2 \frac{P_{rObj}}{P_{tObj}} \ , \tag{9}$$

where R is the distance between the transceiver and the scale model. Finally, the RCS data for the scale model must have a scale factor applied to it [21] in order for us to obtain the full scale values, as shown in Eq. 10.

$$\sigma_{fullScale} dBsm = \sigma_{scaleModel} dBsm + 10log_{10}\left(n^2\right), \tag{10}$$

where n is the scale factor applied to produce the scale model.

The presented novel mm-wave RCS characterization method was enabled by the use of the AWR1843BOOST evaluation module from Texas Instruments [78], which offers a 76-81GHz frequency modulated continuous wave radar implementation. The frequency span of the radar module corresponds to wavelengths of 3.9mm to 3.7mm, which satisfy the conditions required for valid measurements outlined previously.

Additionally, the third condition requiring a low reflectivity environment was satisfied by conducting testing in a wide-open area. At the employed frequencies, this constitutes a low reflectivity environment due to the large free space loss values observed in the mm-wave range. At 75 GHz, the free space path loss is approximately 59 dB/m. The RCS measurements were conducted in 0.9° increments. The power scattered by the object in the direction of the transceiver, P_{rObj}, and the power incident on the object, P_t, are measured using the AWR1843BOOST + DCA1000EVM hardware combination.

The technical characteristics of the AWR1843BOOST millimeter-wave radar transceiver and the DCA1000EVM high-speed data capture are favorable for the application described in this work. Firstly, this hardware combination can produce sufficiently high frequencies, operating in the region of 76-81 GHz [78]. Additionally, the hardware has a low receive channel noise figure of 14-15 dB, built-in calibration, 3 Transmit and 4 Receive channels, and a robust software ecosystem allowing for quick and easy development. The supplied software also allows the user to configure different transmitted chirp profiles for easy prototyping. The hardware has a configurable transmitted bandwidth in the region of 60 MHz to 5 GHz. The transmitted instantaneous bandwidth used in this application was 1.8 GHz. The range resolution achievable by the hardware is as low as 3.25 cm.

The band of 76-81 GHz was chosen due to the scaling requirement which states that the frequency used must be scaled by a factor n, where n is the scale factor of the model; in addition to the commercial availability of the hardware. This band also ensures that the object under test is in the optical scattering region at the corresponding wavelengths, i.e. $l/\lambda \gg 1$, where l is the shortest dimension of the

object.

The experimental test system setup can be seen in Fig. 68, while the block diagram of the internal components of the AWR1843 Antenna on Package chip can be seen in Fig. 69.

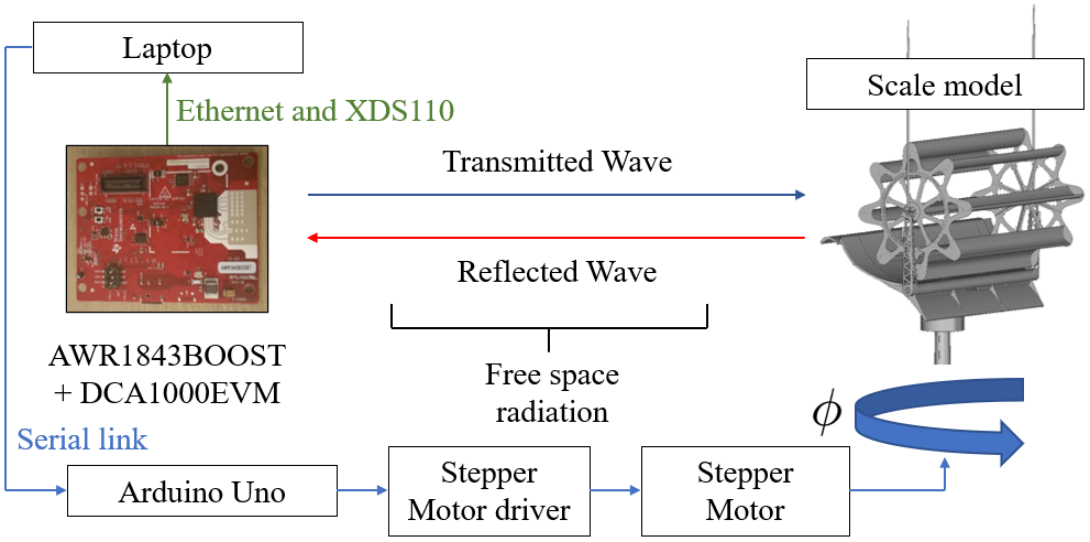

Figure 68: A diagram describing the experimental setup used for the RCS characterization of the scale model Crossflow turbine.

The performance of an indoor RCS test range is typically measured using the following parameters [79]:

- **Isolation:** The level of isolation which is achieved with regards to external electromagnetic noise. The test area should be as quiet as possible, so that the only frequencies that contribute to the RCS measurement are those generated by the measurement system and reflected by the target within the RCS test range. In addition to the isolation of external electromagnetic noise, the isolation of other undesired signals must be considered. These include transceiver leakage, coupling between the transmit and receive antennas, reflections from features of the chamber, or chamber-target interactions [72].
- **Quiet zone:** The quiet zone typically dictates the largest target that can be

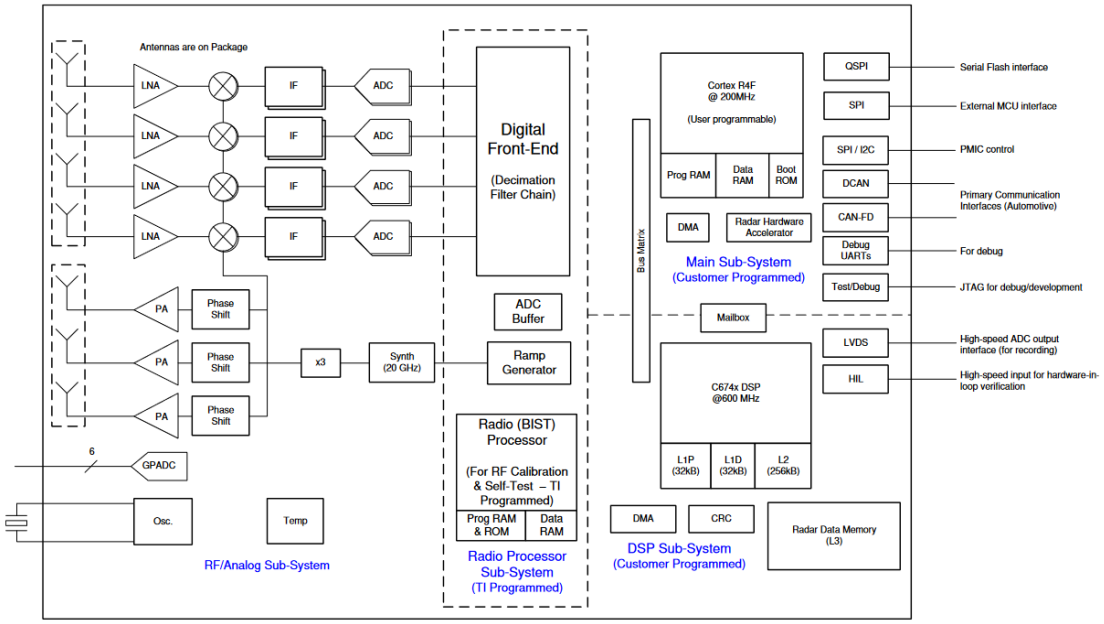

Figure 3-1. Functional Block Diagram

Figure 69: A block diagram of the internal construction of the AWR1843AOP Single-chip 77- and 79-GHz FMCW mmWave Sensor Antennas-On-Package (AOP)

placed within the indoor RCS test range that satisfies the far field conditions, i.e. still allows for a minimum distance between the transceiver and target necessary for the establishment of far field conditions.

- **Minimum detectable RCS:** The minimum detectable RCS is the smallest RCS that can be measured by the range/system.
- **Dynamic range:** This performance metric provides the difference between the maximum power transmitted by the transmit portion of the transceiver, and the noise floor of the receive portion of the transceiver.
- **Frequency range:** The range of frequencies over which the test system can perform measurements.

- **RCS accuracy:** This performance metric is dependent on the total uncertainty present in the system.

The performance of the new system presented in this thesis has been evaluated against other works in the literature using these parameters, and the results are presented in Table. 10. In this table "isolation" refers to the isolation achieved towards electromagnetic signals external to the chamber or range.

Overall, it can be seen that the proposed method and system have several key advantages over methods presented to date in the literature. The most important of these are that the proposed method is low-cost, low-complexity, and fast. This system can therefore facilitate easy and fast prototyping for a number of different applications, where measurement accuracy is important but not safety critical. These advantages can serve to enable an RCS driven iterative design process.

Table 10: A comparison between the system proposed in this thesis and other systems presented in the literature on the basis of their technical characteristics.

Performance indicator	[72]	[70]	[69]	Work in this thesis
Type of radar system	Stepped Continuous wave	Pulsed	Pulsed	Continuous wave
Isolation	> 80dB	> 80dB	> 80dB	> 80dB
Quiet zone	0.5m	Not given	Not given	> 1.5m (Constrained only by the attainable open area)
Minimal detectable RCS	Not given	Not given	Not given	0.2 m^2 from mmWave Sensing Estimator
Dynamic range	Not given	Not given	Not given	56dB
Frequency range (Bandwidth)	11 GHz	0.1 GHz	Not given	4 GHz
RCS Accuracy	High	High	High	High
System Design Time	High	High	High	Low
System Portability	Low	Low	Low	High
System Cost	High	High	High	Low
System Complexity	High	High	High	Low

5.3 Experimental measurements of the Crossflow turbine

A comparison between the results obtained using the proposed experimental method and those obtained via simulations can be seen in Fig. 72 and 73. This diagram shows the excellent agreement achieved between the simulated and experimental results. There is good agreement between the average RCS values, as well as between the location and magnitude of the peak RCS values, observed at $\phi = 90°$ and $\phi = 270°$. These specific areas $\phi = 90°$ and $\phi = 270°$ have been highlighted because they are considered areas of interest, making them good points at which to perform a direct comparison of the simulated and experimentally obtained results.

The newly proposed Radar Cross Section (RCS) characterization method (shown in Fig. 70 and 71) was used to measure the RCS of a scale model of the Crossflow wind turbine kindly supplied by Crossflow Energy.

A dielectric plastic material was used to construct the scale model of the Crossflow turbine via an additive manufacturing method. This is broadly representative of the real life scenario, as the blades of the Crossflow turbine are constructed from Glass-Reinforced Plastic (GRP) composites. Some of the structures of the full scale turbine are made of steel and aluminium, however this difference between the materials used in the scale model scenario and the full scale scenario will not alter the results significantly, as both scenarios are in the far-field scattering region, where the material which the object under test is made out of is of far lesser importance when compared with the geometry of the object when it comes to contribution to RCS.

The novel RCS characterization method presented was used to measure the RCS of a 1:25 scale model of the Crossflow turbine. A comparison between the results obtained using the proposed experimental method and those obtained via simulations can be seen in Fig. 72 for the case of ϕ-polarization and Fig. 73 for the case of θ-polarization. These diagrams show the excellent agreement achieved between the simulated and experimental results. There is good agreement between the average RCS values, as well as between the location and magnitude of the peak RCS values, observed at $\phi = 90°$ and $\phi = 270°$.

These specific areas ($\phi = 90°$ and $\phi = 270°$) have been highlighted because they

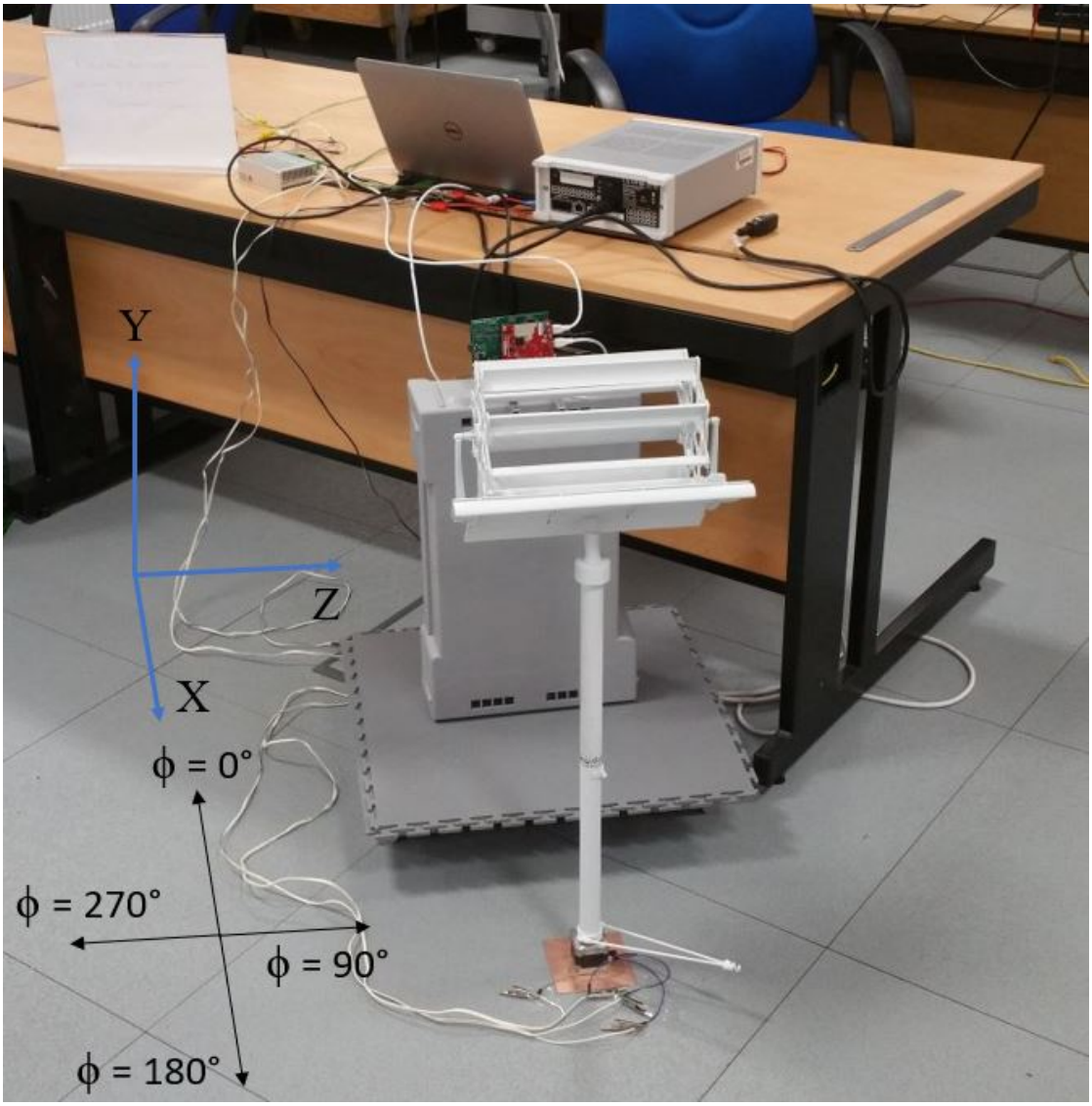

Figure 70: A picture of the Crossflow turbine scale model and experimental setup.

are considered areas of interest, making them good points at which to perform a direct comparison of the simulated and experimentally obtained results. The main cause of the discrepancy between the simulated and experimental results is most likely the non-uniform illumination of the target caused by the specific beam pattern of the antennas on the transceiver. This non-uniform illumination is

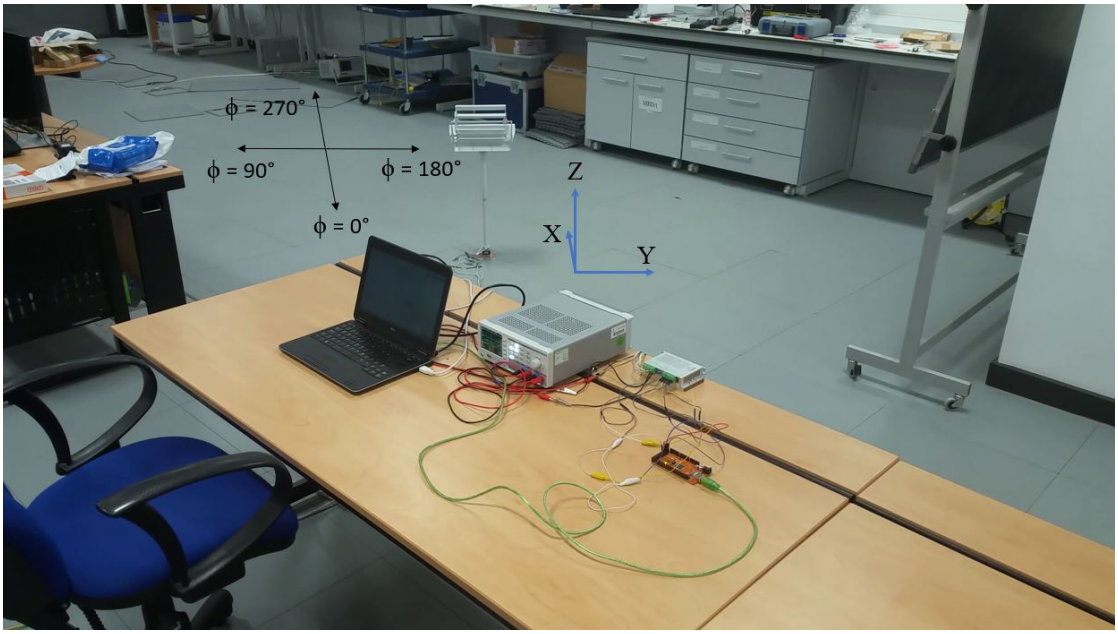

Figure 71: A picture of the Crossflow turbine scale model and experimental setup.

contrary to the scenario presented in simulation, which assumes a plane wave and thus equal illumination of the target, with all areas being illuminated from the same direction. To mitigate this limitation of the experimental setup, the scope of the experimental study was limited to the nacelle of the Crossflow turbine only. This is the primary area of interest in terms of generating novel data - there exists in the literature data for cylindrical structures such as the tower of the turbine, which presents constant radar cross section regardless of aspect angle.

A novel high-frequency RCS characterization method has been presented. The main advantages of the proposed system are a fast measurement speed, low cost, low complexity, and compact nature. These characteristics make the system ideal for fast and easy prototyping, enabling an RCS driven design process, where measurement accuracy is important but not safety critical. Traditional methods typically require an anechoic chamber, and costly bespoke scatterometer systems. In place of these, a wide open space has been used as a low reflectivity environment,

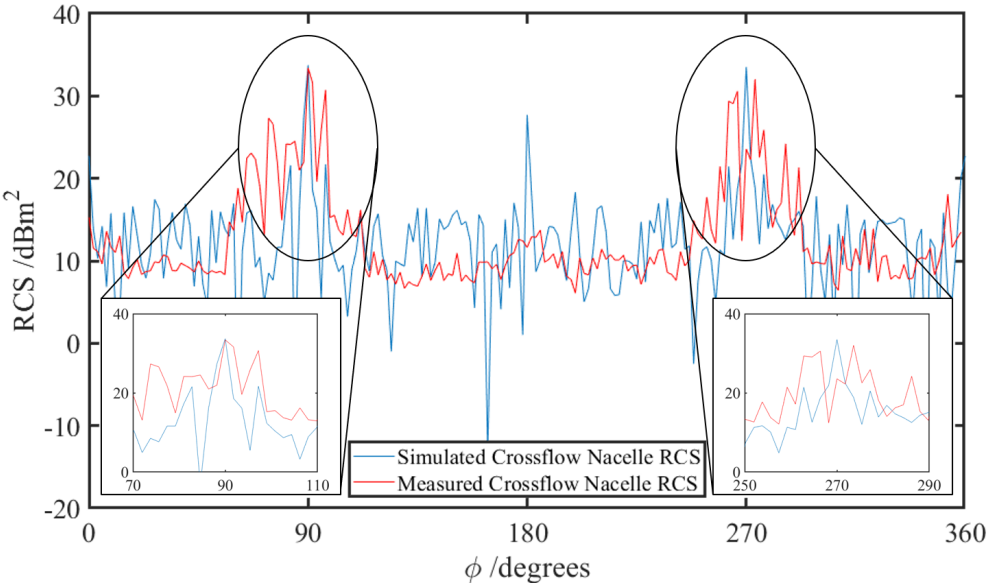

Figure 72: A comparison of the experimental and simulated Crossflow turbine nacelle RCS illuminated by a ϕ polarized plane wave, when the averaged values of the 128 chirps at each point are also averaged, creating just a single line for the experimentally measured RCS.

and a cost effective, commercially available radar system have been used in this work. A table comparing this work against others in the literature can be seen in Table 10. Using the proposed method, RCS measurements of a scale model of the Crossflow turbine have been obtained. These results have been compared against simulation results of the RCS of a traditional HAWT design, and clear advantages for the Crossflow turbine have been demonstrated. Further, good agreement has been observed between the full-scale simulated results and the experimentally obtained scale model results of the Crossflow turbine.This work will also enable the development of novel, low-RCS geometries and designs for a variety of applications such as aviation and ground infrastructure.

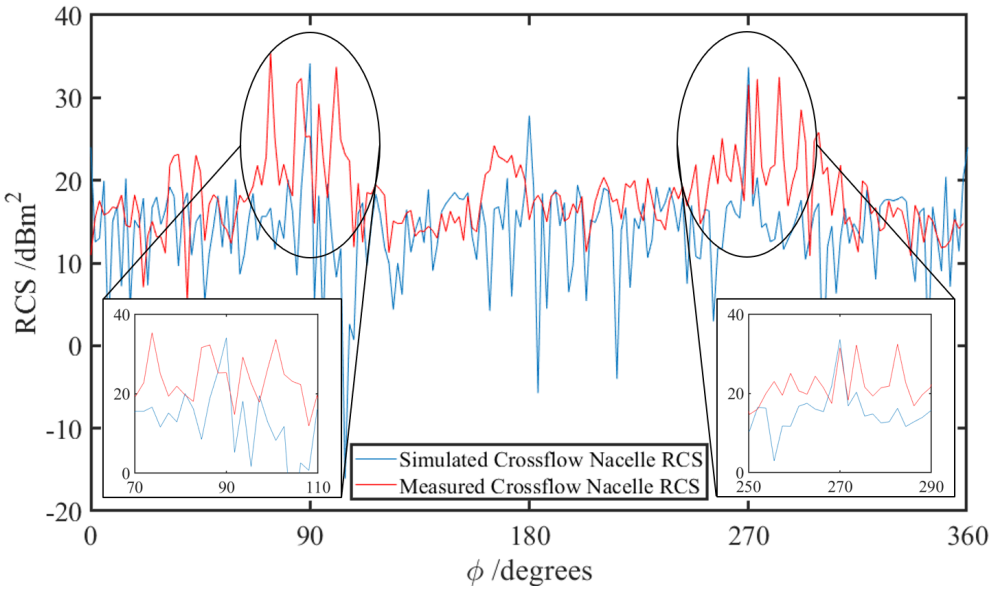

Figure 73: A comparison of the experimental and simulated Crossflow turbine nacelle RCS illuminated by a θ polarized plane wave, when the averaged values of the 128 chirps at each point are also averaged, creating just a single line for the experimentally measured RCS.

6 Frequency Selective Surfaces and Radar Cross Section Reduction

6.1 Introduction

A frequency selective surface (FSS) is generally a thin planar structure consisting of repetitive sub-structures which is designed to exhibit absorption, transmission, reflection, or a combination of all three phenomena over a one or multiple single or narrow frequency ranges. Additionally, FSS can be designed to exhibit a certain refractive index. Typically, an FSS consists of a periodic structure of metallic or dielectric elements. As a result of this design, frequency selective surfaces have properties that are not only dependent on frequency, but also angle of incidence.

FSS find a wide range of applications. The first FSS structures developed were absorbers and radomes. Both were initially developed for defense applications. Both absorbers and radomes were first developed for the purposes of radar stealth applications. In the case of absorbers, the aim was to reduce the reflectivity of the coated object, for the purposes of reducing the detectability of the target by hostile radars. The application of FSS radomes is similar, as antennas typically exhibit high radar cross sections (RCS) when illuminated by frequencies outside of their operating ranges.

6.2 Equivalent circuit modelling of FSS

Metamaterials can be defined as materials which exhibit properties which are not readily available in any natural materials. These properties also arise from the engineered structure of the metamaterial, as opposed to any inherent property of the constituent materials. The first realized metamaterial was a double negative metamaterial, which simultaneously exhibits negative electric permittivity, and negative magnetic permeability.

Another useful property which metamaterials can be engineered to have is that of the capacity to absorb electromagnetic radiation which is incident on the meta-

material surface. This has extreme potential for the radar cross section reduction of various structures from antennae to large objects. Generally, the absorption is produced when the metamaterial array resonates in response to being excited by a particular electromagnetic frequency, or range of frequencies. Under this condition, the real part of the surface impedance $\Re(Z_s)$ of the metamaterial matches that of free space, thus reducing reflections; while the imaginary part of the surface impedance $\Im(Z_s)$ tends towards infinity [80] [81].

The resonance of a metamaterial array is a result of the capacitances and inductances which arise from the metamaterial structure. An extremely effective and useful method of designing and modelling a metamaterial array is the use of an equivalent circuit model. This approach involves using empirical formulas in order to express the effective capacitances and inductances of the structure in terms of the dimensions and geometry of the structure. These effective circuit impedances can then be arranged in an effective circuit, the topology of which is also dependent on the geometry of the structure in question.

6.3 The equivalent circuit model

6.3.1 Explanation of the model and the model implementation

The equivalent circuit model presented in this section is a modification of the equivalent circuit model presented in [1]. The model consists of two parallel impedances. One of the impedances, Z_{Fss} represents the impedance of the frequency selective surface, i.e. the surface metallization. The second impedance Z_{TML} models the impedance encountered in the substrate and ground plane.

A diagram of the equivalent circuit model of a square loop metamaterial absorber taken from [1] can be seen in Fig. 74.

The FSS impedance Z_{FSS} can be expressed in the following way [1]:

$$Z_{FSS} = R_{FSS} + j\omega L_{FSS} + 1/j\omega C_{FSS} \tag{11}$$

Where Z_{FSS} is the surface impedance of the frequency selective surface, R_{FSS} is the resistive component of the impedance of the frequency selective surface, L_{FSS}

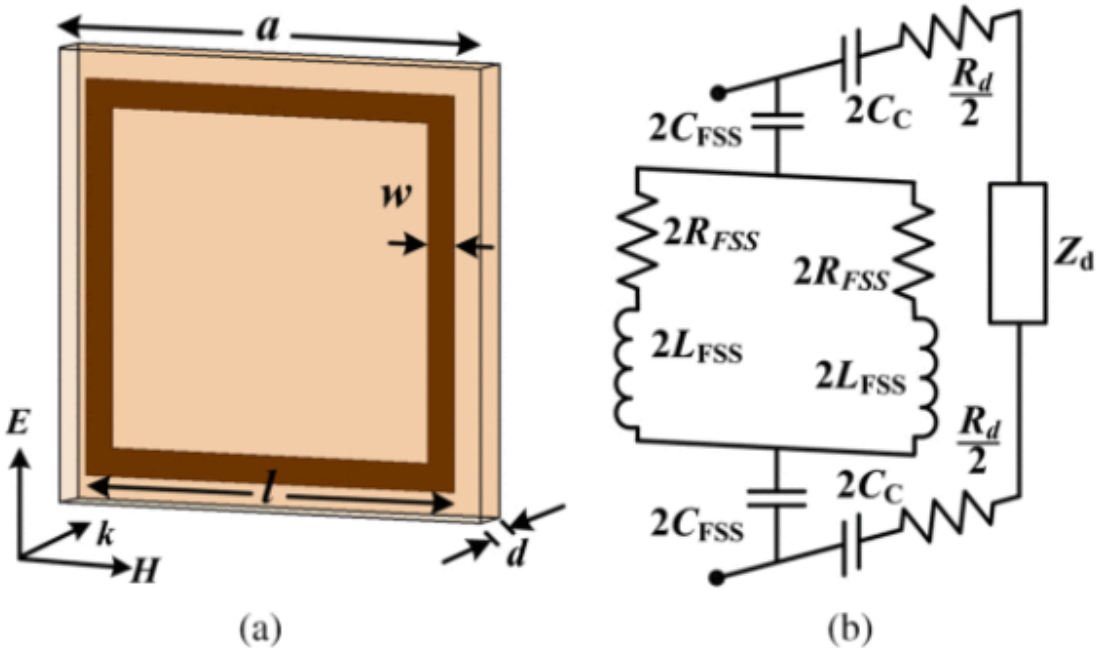

Figure 74: A diagram of an equivalent circuit model of a square loop resonator taken from [1].

is the inductive component of the impedance of the frequency selective surface, and C_{FSS} is the capacitive component of the impedance of the frequency selective surface.

On the other hand, the substrate impedance Z_{TML} can be expressed in the following way:

$$Z_{TML} = Z_d + Z_c = j\sqrt{\frac{\mu_0\mu_r}{\epsilon_0\epsilon_r}}tan(kd) + R_d + \frac{1}{j\omega C_c} \tag{12}$$

The surface impedance of the frequency selective surface is then given by:

$$Z_{surf} = Z_{FSS}||Z_{TML} \tag{13}$$

From this point, the lumped element values can be related to the physical frequency selective structure (FSS) dimensions.

6.3.2 Example case used for results validation

A square loop metamaterial array was realized and simulated in the CST Microwave Suite. This was done with the aim of validating the results produced by the equivalent circuit model.

6.3.3 FSS resistance

The FSS resistance can be calculated using empirical equations for resistivity, and is dependent on the dimensions of the square loop, and the resistivity of the metal used for its construction. As the cross sectional area of the FSS patch and its physical composition are assumed to remain constant throughout, the resistance of the FSS patch can be calculated in the following way, for our example case:

$$R_{FSS} = \rho \frac{l}{A} \tag{14}$$

$$R_{FSS} = \rho_{copper} \times \frac{4 \times squareloopfactor \times innerradius}{stripwidth \times copperthickness} \tag{15}$$

$$R_{FSS} = \rho \frac{l}{A} = 5.8 \times 10^7 \times \frac{4 \times 16.97 \times 10^{-3}}{2 \times 10^{-3} \times 0.012 \times 10^{-3}} \tag{16}$$

$$R_{FSS} = 0.089\Omega \tag{17}$$

6.3.4 FSS inductance

The FSS inductance is calculated using the following formula:

$$L = \frac{Z_C \times \sqrt{\epsilon_{re}}}{c} \tag{18}$$

where $c = 3 \times 10^8$. This equation gives us the inductance per unit length for the frequency selective surface. Before we can solve this equation, we first need to calculate the effective permittivity ϵ_{re}, and the characteristic impedance Z_c for the scenario. These can be calculated using transmission line theory, in the following

way [82]:

For the case where $W/h \leq 1$:

$$\epsilon_{re} = \frac{\epsilon_r + 1}{2} + \frac{\epsilon_r - 1}{2}((1 + 12\frac{h}{W})^{-0.5} + 0.04(1 - \frac{W}{h})^2) \tag{19}$$

$$Z_c = \frac{\eta}{2\pi\sqrt{\epsilon_{re}}} \ln(\frac{8h}{W} + 0.25\frac{W}{h}) \tag{20}$$

and in the case where $W/h \geq 1$:

$$\epsilon_{re} = \frac{\epsilon_r + 1}{2} + \frac{\epsilon_r - 1}{2}(1 + 12\frac{h}{W})^{-0.5} \tag{21}$$

$$Z_c = \frac{\eta}{\sqrt{\epsilon_{re}}}(\frac{W}{h} + 1.393 + 0.677\ln(\frac{W}{h} + 1.444))^{-1} \tag{22}$$

6.3.5 FSS capacitance

The FSS capacitance is a result of the mutual coupling between neighbouring unit cells. When the electromagnetic radiation is incident on the structure, the distribution of the electric field results in a circular formation of surface currents within the square loop structure. This is true for both TE and TM polarization. Each unit cell exhibits odd mode coupling with two of its neighbours, and even mode coupling with the other two [2].

C_{FSS} has been designated as the horizontal coupling between neighbouring unit cells, whereas C_c has been designated as the vertical coupling between unit cells and the ground plane.

The following image demonstrates the capacitances formed between neighbouring lines in the odd and even modes, i.e. in the case that the currents are parallel (even mode), and in the case that the currents in the two lines are running antiparallel (odd mode) [2]:

We can then use the following equations:

$$C_{FSS-odd} = C_{ga} + C_{gd} \tag{23}$$

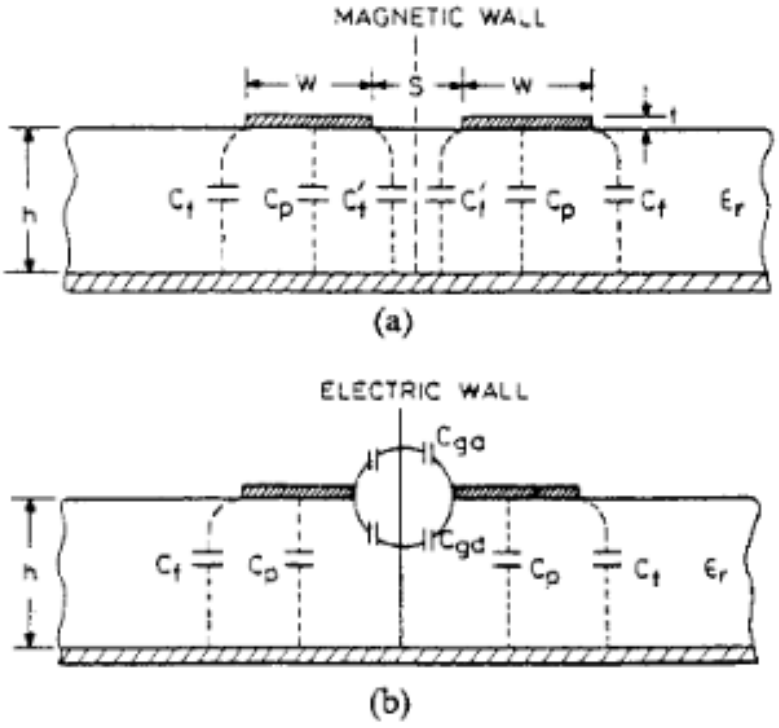

Figure 75: A figure reproduced from [2] demonstrating where capacitance is generated in the case of coupled microstrip lines where (a) illustrates even-mode capacitances and (b) illustrates odd-mode capacitances.

As there is no horizontal component of capacitance during even mode coupling:

$$C_{FSS-even} = 0 \tag{24}$$

Where:

$$C_{ga} = \epsilon_0 \frac{K(k')}{K(k)} \tag{25}$$

and:

$$k = \frac{S/h}{S/h + 2W/h} \tag{26}$$

$$k' = \sqrt{1 - k^2} \tag{27}$$

$$\frac{K(k')}{K(k)} = \begin{cases} \frac{1}{\pi} \ln(2\frac{1+\sqrt{k'}}{1-\sqrt{k'}}), & \text{if } 0 \leq k^2 \leq 0.5 \\ \frac{\pi}{\ln(2\frac{1+\sqrt{k}}{1-\sqrt{k}})}, & \text{if } 0.5 \leq k^2 \leq 1 \end{cases} \tag{28}$$

In addition to this, we can also go ahead and write the equation for C_{gd}:

$$C_{gd} = \frac{\epsilon_0 \epsilon_r}{\pi} \ln(\coth \frac{\pi}{4} \frac{S}{h}) + 0.65 C_f [\frac{0.02}{S/h} \sqrt{\epsilon_r} + 1 - \epsilon_r^{-2}] \tag{29}$$

Where:

$$C_f = \frac{\frac{\sqrt{\epsilon_{re}}}{cZ_0} - C_p}{2} \tag{30}$$

and

$$C_p = \epsilon_0 \epsilon_r \frac{W}{h} \tag{31}$$

Finally, we can write an equation for the FSS capacitance:

$$C_{FSS} = 2 \times C_{FSS-odd} + 2 \times C_{FSS-even} \tag{32}$$

so for each square loop FSS unit cell, and due to the fact that there are two C_{ga} and two C_{gd} capacitances in series:

$$C_{FSS} = 2 \times (0.5 \times C_{ga} + 0.5 \times C_{gd}) \tag{33}$$

$$C_{FSS} = C_{ga} + C_{gd} \tag{34}$$

6.4 Substrate and ground plane related impedances

6.4.1 The substrate capacitance

The substrate capacitance C_c is the capacitance formed as a result of the vertical gap between the frequency selective surface and the ground plane. From Figure 2, we can see that the capacitance formed between the frequency selective surface and the ground plane can be expressed as follows. For the case of odd mode coupling, for one set of coupled microstrip transmission lines:

$$C_{c-odd} = 2 \times (C_p + C_f) \tag{35}$$

and for the case of even mode coupling between transmission lines:

$$C_{c-even} = 2 \times (C_p + C_f + C_{f'}) \tag{36}$$

Therefore, we can say that for the total vertical component of capacitance for each unit cell, we have the following:

$$C_c = 2 \times (C_{c-odd} + C_{c-even}) \tag{37}$$

now, if we substitute the values in, expand, and collect, we can arrive at the final equation for C_c in the following way:

$$C_c = 2(2(C_p + C_f) + 2(C_p + C_f + C_{f'})) \tag{38}$$

$$C_c = 4(C_p + C_f + C_p + C_f + C_{f'}) \tag{39}$$

$$C_c = 4(2C_p + 2C_f + C_{f'}) \tag{40}$$

6.4.2 Equivalent resistance due to dielectric loss

The equivalent resistance due to dielectric loss in the substrate, and representing the imaginary part of the material parameters is R_d. The dielectric loss is a result of thermal agitation which is a randomizing force on the dipole orientations within the substrate, meaning that the dipole moments cannot react instantaneously to changes in the applied electric field. This can be calculated in the following way:

$$R_d = \frac{d}{\omega \epsilon_0 \epsilon_r'' A} \tag{41}$$

6.4.3 The substrate impedance

The impedance due to attenuation in the substrate is given by the following equation [1]:

$$Z_d = j\sqrt{\frac{\mu_0 \mu_r}{\epsilon_0 \epsilon_r}} tan(kd) \tag{42}$$

where

$$k = k_0 \sqrt{\epsilon_r \mu_r} \tag{43}$$

and [83]:

$$k_0 = \frac{2\pi}{\lambda} \tag{44}$$

where k_0 is the wavenumber of the wave in free space, and k is the wavenumber of the wave in the substrate.

6.5 Equivalent circuit modelling reproduction of absorptive-transmittive surface

Using the information presented in the previous subsections, equivalent circuit models of metamaterial and absorptive-transmittive structures can be realized. This is a very useful technique in the design of frequency selective surfaces. It allows the designer to arrive at a desired equivalent circuit model performance, then translate this into a functional design in the electromagnetic domain.

As flexible metamaterial absorbers and absorptive transmittive surfaces i.e. rasorbers have already been described in the literature, I turned my attention to realizing a novel design using a flexible substrate and the advantages of the screen printing technique.

In order to verify the equivalent circuit modelling methodology, I first replicated the results presented in several works in the literature

6.6 Genetic Algorithm based Metamaterial Design

For the realization of a fast optimization system using genetic algorithms, the evaluation time for a unit cell simulation must be kept to a minimum due to the large number of unit cell simulations required. Three different options were investigated – using MATLAB to evaluate the unit cell performance, running the unit cell on a cluster, and running the unit cell in time domain on the GPU computers in the lab. There is a fourth available option, which is running the simulation locally on a desktop or laptop. This is feasible, however any speedup that can be achieved would be greatly beneficial.

6.6.1 Unit cell evaluation in MATLAB

Running the unit cell evaluation in MATLAB essentially involves programming an FDTD solver from close to scratch, so this would be a method that is very heavy in terms of developer time, and would require even more time to optimize correctly.

6.6.2 Unit cell evaluation on a GPU accelerated computer

In order to test the time taken for the GPU computers to run a single evaluation of a unit cell, a simulation was set up using the time domain method, which benefits greatly from GPU acceleration. A test simulation was put together consisting of 16,464 unit cells.

In order to set a benchmark time, this was first run locally on my laptop. The simulation completed in a total of 62 seconds. Following this, the simulation was sent to over the internal university network for simulation on the GPU enabled machines in the lab. Performing this operation resulted in a simulation time of 36 seconds. It is possible that the speed-up would be more significant if the simulations were run directly on the GPU machine as opposed to being run via the Distributed Computing (DC) functionality of CST. This is because using the DC functionality of CST results in additional overheads, most significantly that of passing data back and forth between the two computers. Removing this overhead, we should see a time closer to 30 seconds.

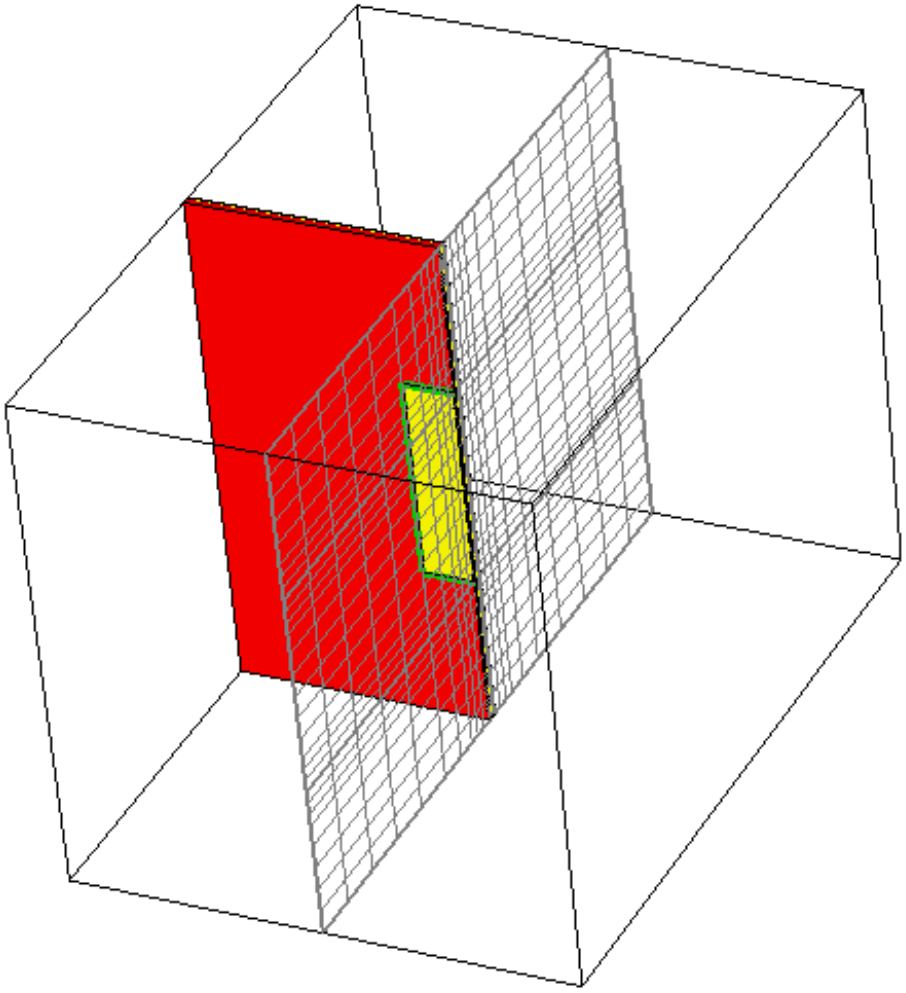

Figure 76: A diagram of an example of one of the frequency selective surface unit cells that was simulated as part of the implementation of the genetic algorithm based optimization method.

6.6.3 Feasibility in terms of time

One of the papers we can use to arrive at a time calculation is presented by Cui et al. and is titled "Novel planar electromagnetic absorber designs using genetic algorithms". In this paper, the researchers present a planar absorber design for the frequency range of 20-25GHz, and use a similar methodology to the one we intend to use for our application. Using our current benchmarks of around 1-5-2.5 hours per generation, and assuming that we need to run a number of generations in the order of several hundreds, we can calculate that this should take in the order of 1-2 weeks. This process can be sped up by running the simulations on a faster machine such as the GPU containing computers in the lab.

6.6.4 Methodology

The unit cell was initially set to be of size 5x5mm, and was split into 10x10 smaller squares. For the first generation, 100 designs were generated by randomly assigning either a 0, a 1, or a 2 to each square. This corresponded to no conductive layer deposition, deposition of silver containing ink, or deposition of carbon containing ink respectively. This operation was carried out in MATLAB, after which MATLAB instructs CST to build the structure, simulate it, and return the S11 and S21 parameter data back to MATLAB for analysis. This data is then used to calculate the absorption exhibited by the structure over the frequency range of simulation. The area under the absorption curve is then calculated by performing numerical integration using the trapezoidal rule, and this score forms the fitness function against which the designs are evaluated. The communication between MATLAB and CST was realized using the

After the 100 individuals comprising the first generation have all been simulated and evaluated against the fitness function, the top 50 designs are chosen to be used for the creation of the second generation of individuals. Initially, this was achieved by performing a two point crossover using a function file uploaded to the MATLAB file exchange from the author Seyedali Mirjalili. However, I had to modify the code for it to work correctly with the form of data that I was providing I was providing to the function. Also, it would not work correctly under double mode crossover,

i.e. producing two individuals from the two parents, which is another reason why I had to modify the code. Unfortunately it appears that I have not modified the code correctly or sufficiently, as the result show that after the first successful non-stop run of 20 generations, the results were not improving from roughly the second generation onwards. In addition to this, the two "children" produced by the Crossover events are not of the same size, indicating an incorrect crossover methodology. Part of the reason for this lies in the fact that the genetic crossover function which I used was taken from the MATLAB file exchange, and was designed to work with 1 dimensional arrays only as opposed to two dimensional arrays like the type that I have used to store the genome for the absorber designs.

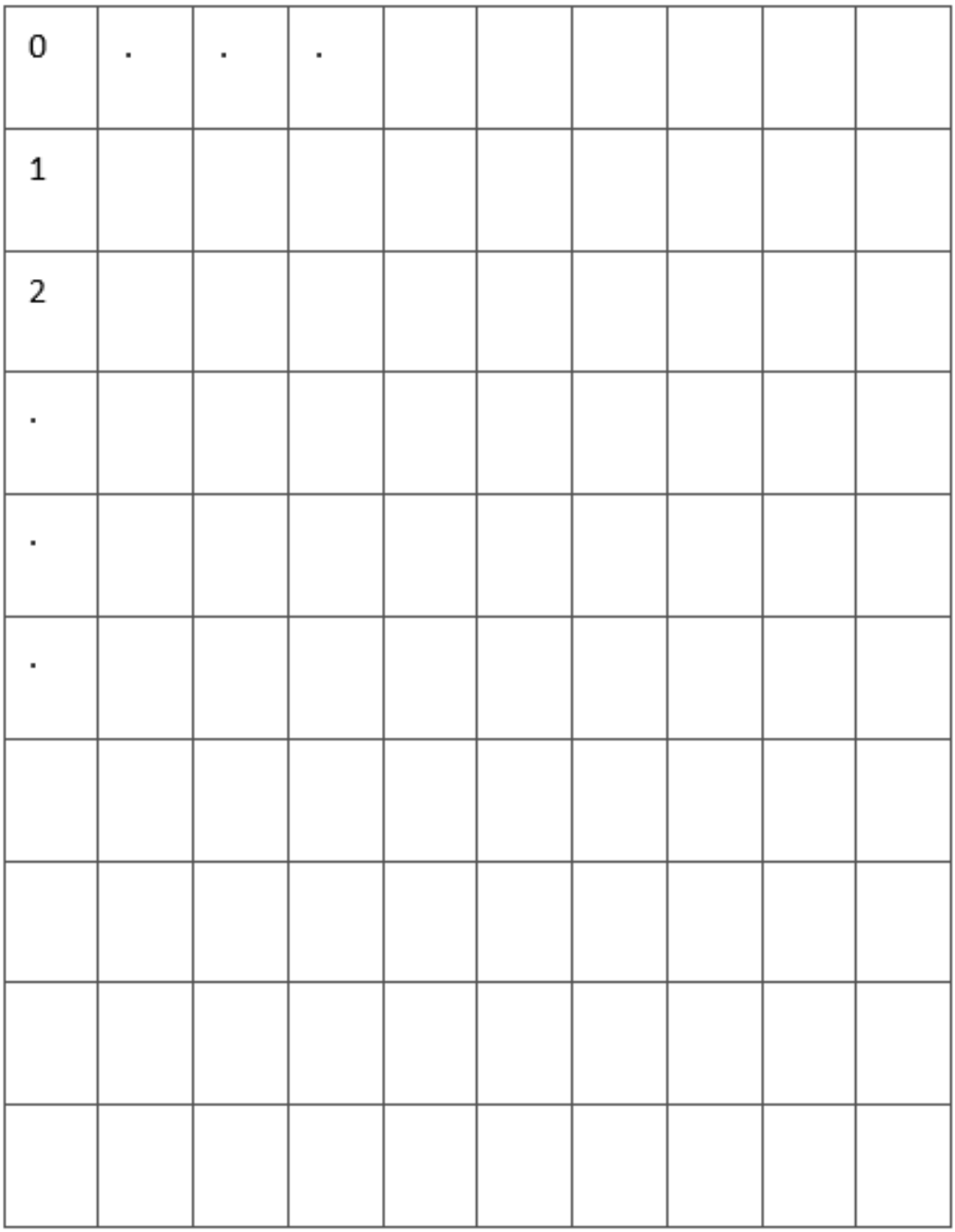

Figure 77: A diagram of an example of one of the frequency selective surface unit cells that was simulated as part of the implementation of the genetic algorithm based optimization method.

6.6.5 End goals of using the genetic algorithm approach for electromagnetic absorber design

While the genetic algorithm approach can be used for a wide variety of applications, here it is used for the design of practical electromagnetic absorber structures. We seek to innovate in this field by improving on several key metrics used for the performance characterization of electromagnetic absorbers. Specifically, these key areas are thickness, flexibility, ease of manufacturing, bandwidth, and the magnitude of the exhibited absorption.

The motivation for wanting to improve on these metrics is that it is necessary to do so for the manufacturing of a practical electromagnetic absorber which can be applied conformally to a wide variety of structures, including ones where aerodynamic performance is a concern, such as wind turbines.

6.7 Split ring resonator structures for Radar Cross Section Reduction

6.7.1 Introduction

Metamaterials have been a burgeoning field of research in recent years, with many new developments such as reconfigurable designs [84] capable of live absorption spectrum switching [85], wideband designs [86] with bandwidths in the region of 30GHz [87], and multi-band [88] absorber designs with as many as 4 [89] absorption bands, as well as many other applications such as negative refraction and subwavelength resolution. In addition to a variety of different metamaterial absorber designs, a metamaterial cloak has been presented [90], which functions as a planar waveguide in order to guide electromagnetic radiation around the object contained within the cloaking structure. While this technology is promising, and could be applied to the tower section of wind turbines; it cannot be applied to situations where aerodynamic performance is necessary, e.g. the blades of a wind turbine.

In this section, the performance of a selection of ring based metamaterial absorber structures which can be employed to reduce the RCS of the Crossflow tur-

bine (and other wind turbines) is demonstrated and evaluated. Having the ability to cheaply and effectively reduce the RCS in this manner is one potential way to allay concerns regarding interference from new wind turbine developments. This technology can also be retroactively applied to existing wind turbine installations, improving safety and target tracking in the vicinity. A unique aspect of this work is the mass low cost production of a printed metamaterial absorber layer applied to wind turbine surfaces for the reduction of their RCS. A widespread adoption of this technology could see areas much closer to civilian and military airfields suddenly become viable areas on which wind turbines can be installed. This would increase the pace of adoption of renewable energy generation technologies, as well as providing a valuable commercial opportunity, and allowing airports and other locations with radar installations to have their own energy generation facilities in the form of wind turbine installations.

We chose to study the presented ring resonator structures for their simplicity, ease of manufacturing, and low material cost. They are also structures for which a number of analytical models exist that can assist with the design process [91] [92]. In addition to this, we did not find a direct comparison of the performance of these four canonical structures in the existing literature, hence this is another novel aspect of our work.

6.7.2 Ring resonator selection and unit cell characterization

Initially, four different ring resonator structures were studied and characterized. The structures studied were a round loop, a split round loop, a square loop, and a split square loop. These four unit cells can be seen in Fig. 1. The four structures were all tuned to have their main resonance peaks at 2.82GHz, in the S-band, which is the central frequency used by primary air traffic control radar. All of the designs feature a solid copper backplane and were designed using 1.6mm thick FR-4 substrate, and a copper thickness of 0.012mm.

$$A = 1 - |S_{11}|^2 - |S_{21}|^2 \tag{45}$$

These structures were simulated using CST Microwave Suite to obtain the S_{11}

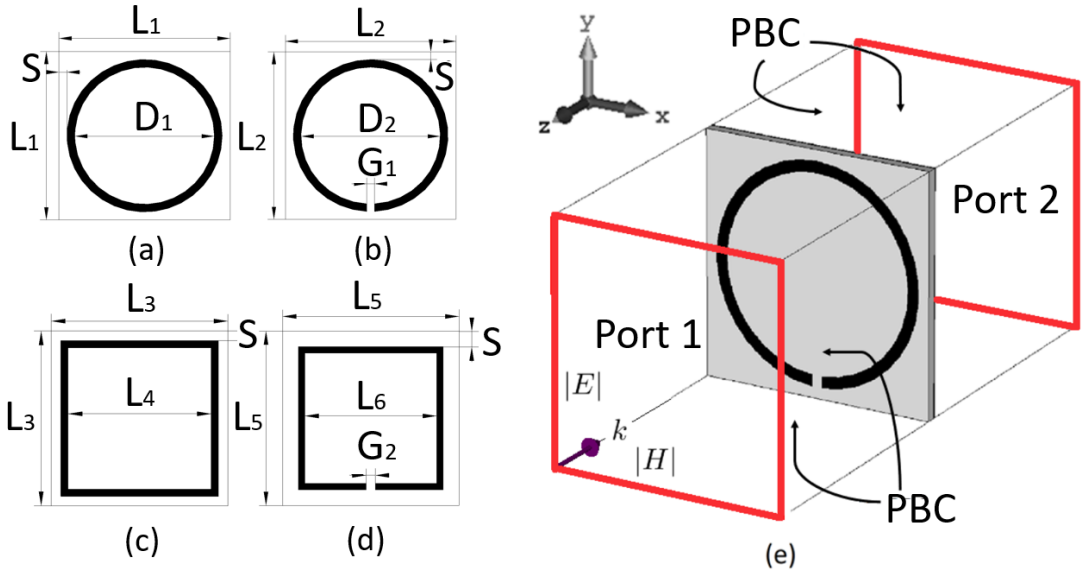

Figure 78: (a) - Round loop unit cell where $D_1 = 17.58mm$, and $L_1 = 21.58mm$. (b) - Round split loop unit cell where $D_2 = 17.766mm, G_1 = 1mm$, and $L_2 = 21.766mm$. (c) - Square loop unit cell where $L_3 = 17.3594mm$, and $L_4 = 14.0573mm$. (d) - Square split loop unit cell where $L_5 = 19.11mm, G_2 = 1mm$, and $L_6 = 14.1391mm$. For all unit cells, $S = 1mm$. (e) - The simulation methodology used for the characterization of the unit cells.

results seen in Fig. 2. As shown in Fig. 1, a periodic boundary condition was used in order to capture the effects of mutual coupling between neighbouring cells, and two ports were used in order to capture the S_{11} and S_{21} parameters. Following this, Eqn. 1 was used to calculate the absorption.

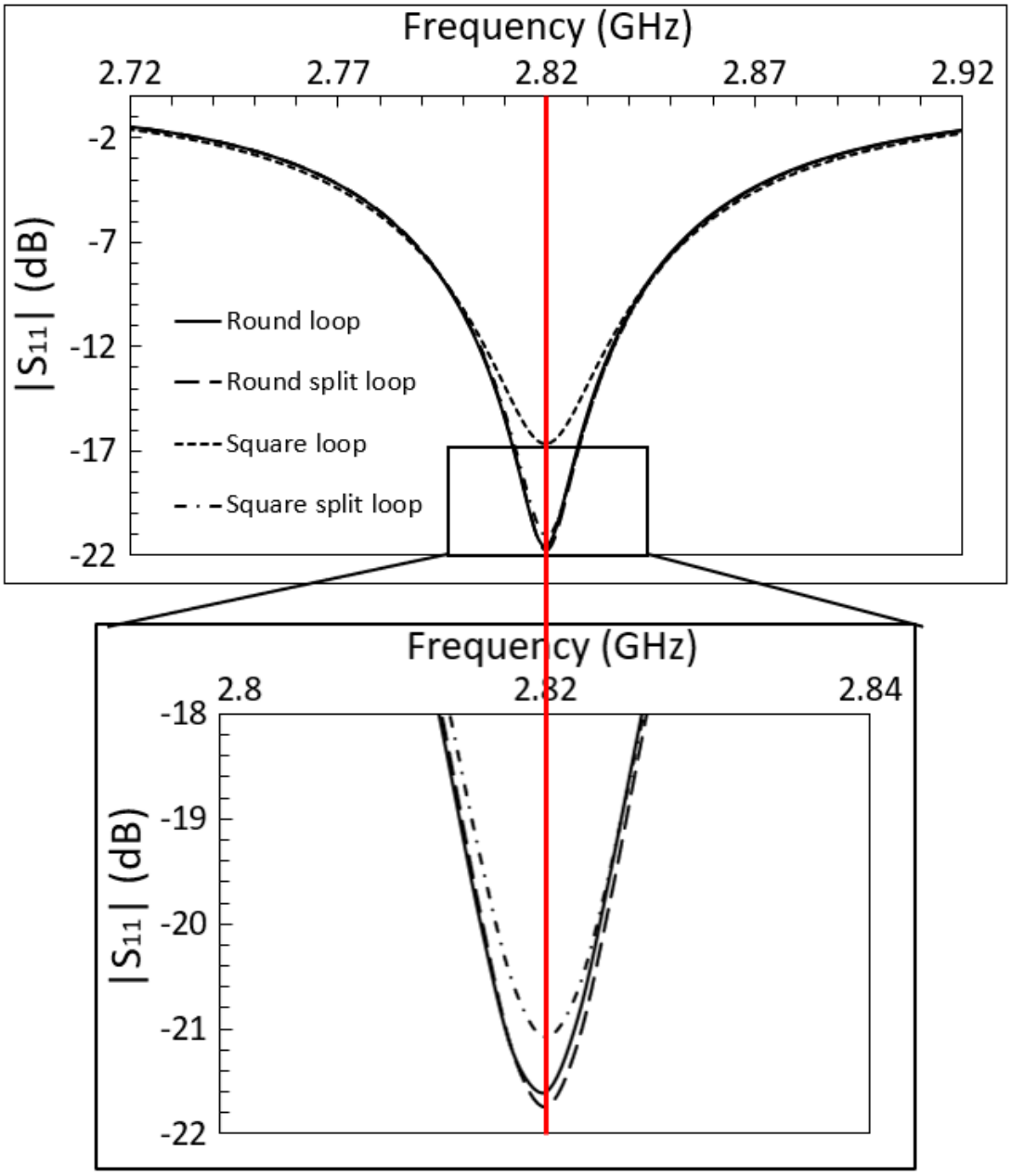

Figure 79: The S_{11} parameter results for the unit cells, performed under TE polarization.

6.7.3 Array characterization and simulation results

In order to better capture the interaction between adjacent unit cells, with the aim of more accurately modelling array behaviour, as well as more accurately recreating the planned experimental procedure, we carried out simulations of four different arrays, each made up using one of the four respective unit cells. Simulations were conducted using TE and TM polarized radiation at close to normal incidence. This is considered a valid and sufficient test as symmetrical resonator geometries have been shown to display polarization independence [93], and in the case of an asymmetrical design, the unit cell can be rotated to match the polarization. In addition to this, simulating the arrays under TE and TM polarized incident radiation is a good approximation for the performance that may be observed when the arrays are illuminated by circularly polarized radiation, which is utilized by primary surveillance radar in most civil aviation applications. The four arrays constructed were 9x13 unit cells in size, and can be seen in Fig. 3. In Fig. 4, we can see the simulation setup used to characterize the reduction in S_{21} affected by the four arrays. Finally, the reduction in S_{21} affected by each of the four absorber arrays as compared with a copper sheet of the same area can be viewed in Fig. 5.

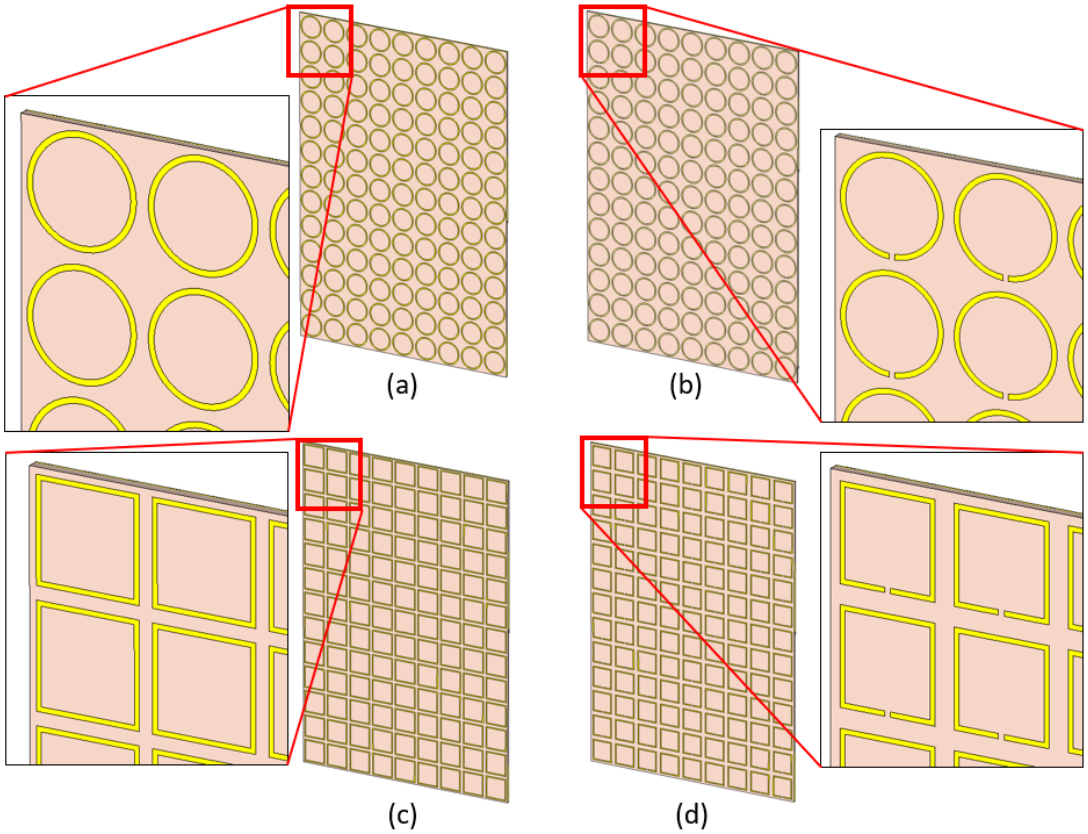

Figure 80: (a) - The round loop array, (b) - The round split loop array, (c) - The square loop array, (d) - The square split loop array. All arrays consist of 9x13 unit cells.

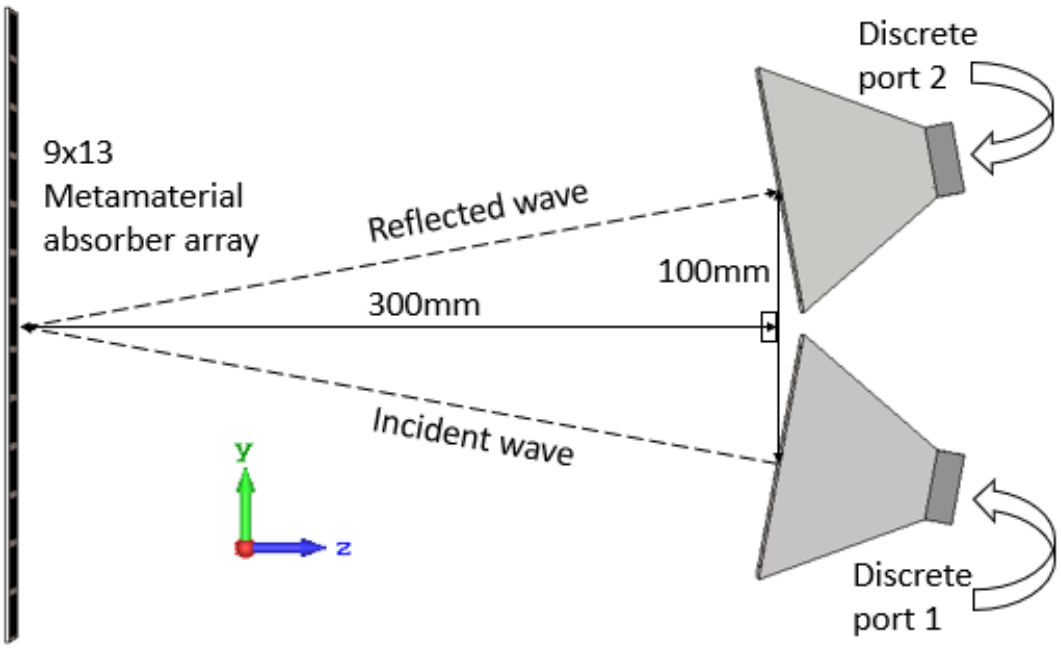

Figure 81: A diagram of the simulation setup used to characterize the four 9x13 arrays.

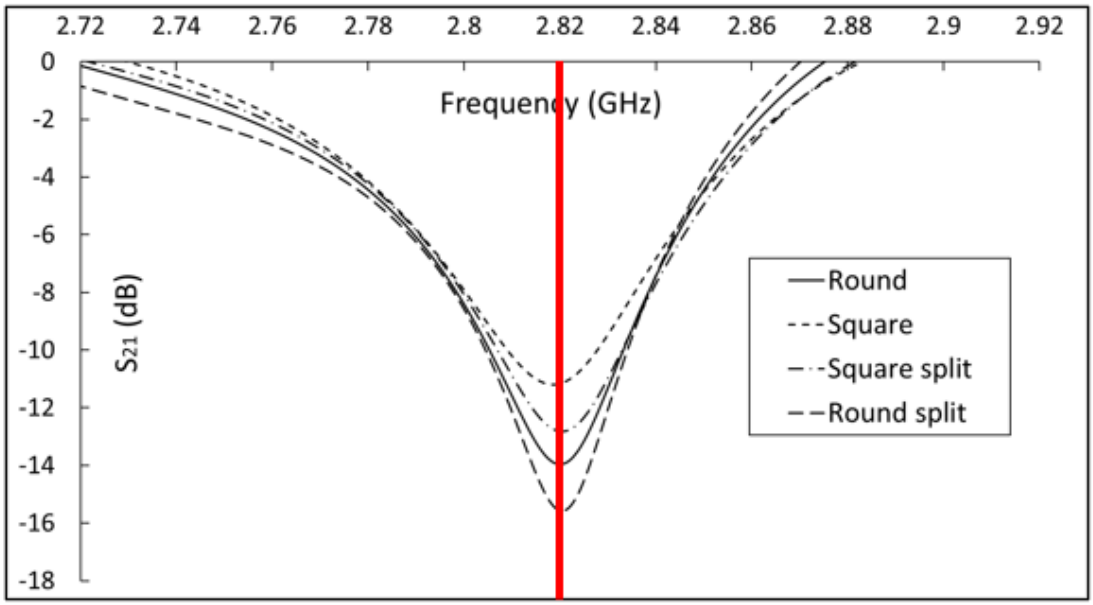

(a)

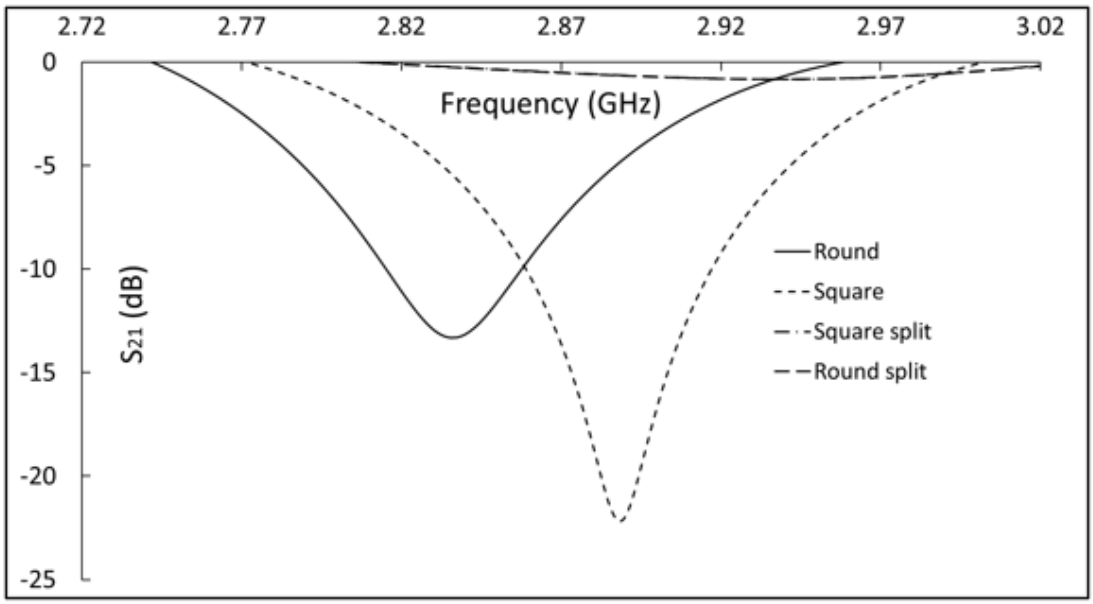

(b)

Figure 82: A graph of the S_{21} results for the four absorber arrays produced via simulation. (a) - Under TE polarization (b) - Under TM polarization.

6.8 Experimental validation of results

In order to validate the simulation results presented, the four 9x13 metamaterial designs were manufactured and tested in order to demonstrate the concept of using metamaterial absorbers for RCS reduction. The designs were fabricated on a 1.6mm thick FR-4 dielectric sheet using standard PCB printing technology, or more specifically, a wet chemical etching process. A PCB milling machine was also used to manufacture the designs, with the aim of reducing the discrepancy between the simulation and experimental data, however this approach was no more successful than the wet chemical etching process in producing closer agreement between the two sets of results.

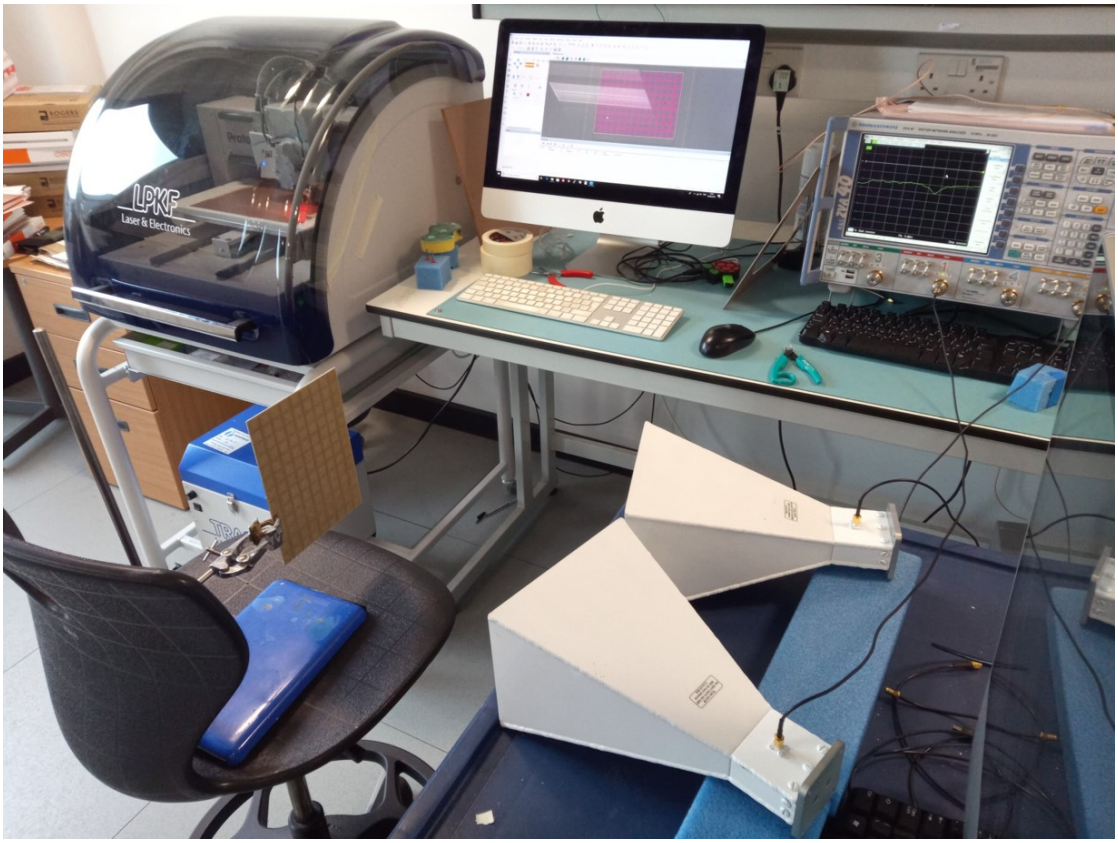

Figure 83: A picture of the setup used for the experimental validation of the S_{21} results of the four absorber arrays.

In Fig. 6, we can see one of the finished absorber arrays under test. Two identical horn antennas were used, in conjunction with a VNA, to measure the S_{21} parameter between two of the ports on the VNA, each of which was attached to one of the horn antennas. In this way, we closely mimicked the setup used for the simulation of the absorber arrays.

The sample was supported by a very thin clamp stand, in order to minimize the reflection contribution of the supporting structure. Initially, the metamaterial sample was oriented so that the solid copper backplane was facing the antennas. The S_{21} parameter was then measured, in order to create a point of comparison for the exhibited absorption. The metamaterial absorber was then flipped, so that the split ring side was facing the antennas. The S_{21} parameter was then measured again. Throughout this process, the absorber sample was kept in the middle of the two antennas, ensuring that the angle between the normal of the metamaterial absorber face and the direction of maximum gain of the antenna is the same for both antennas. Once S_{21} results were obtained for both sides of each absorber, the S_{21} data obtained when the ring side of the absorber was facing the antennas was subtracted from the S_{21} data obtained when the ground plane side of the absorber was facing the antennas. In this way, the S_{21} reduction affected by each absorber was calculated. This process was repeated again after rotating and re-aligning the antennas, in order to obtain data for performance under TM polarization also. In Fig. 84, the S_{21} reduction results obtained in this way can be seen, while in Fig. 8, a diagram comparing the peak S_{21} reduction (and hence peak absorption) exhibited by each array can be seen.

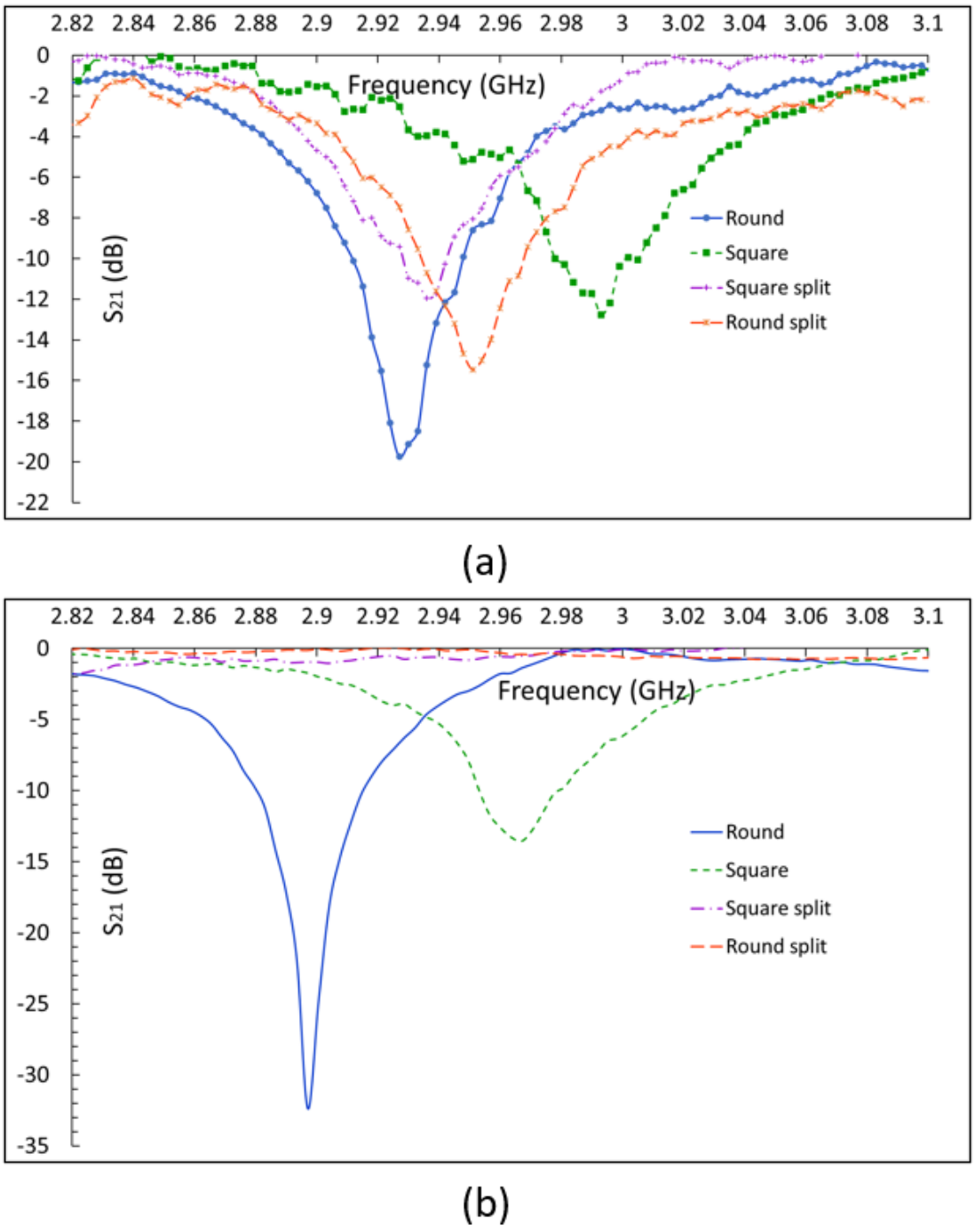

Figure 84: A comparison of the S_{21} results obtained via experimentation. (a) Under TE polarization (b) Under TM polarization.

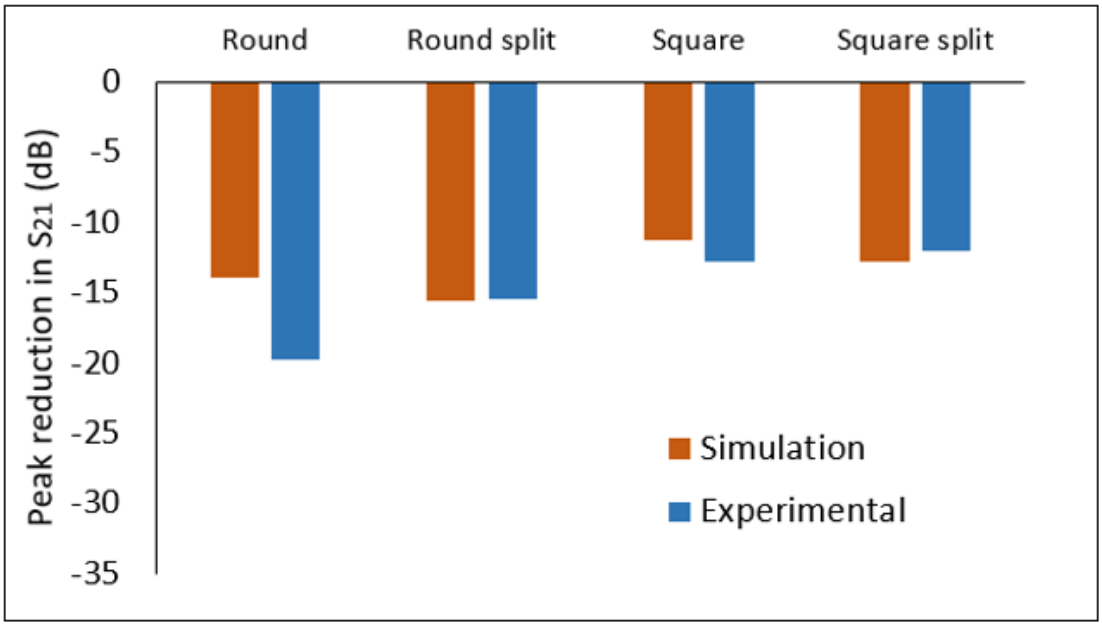

(a)

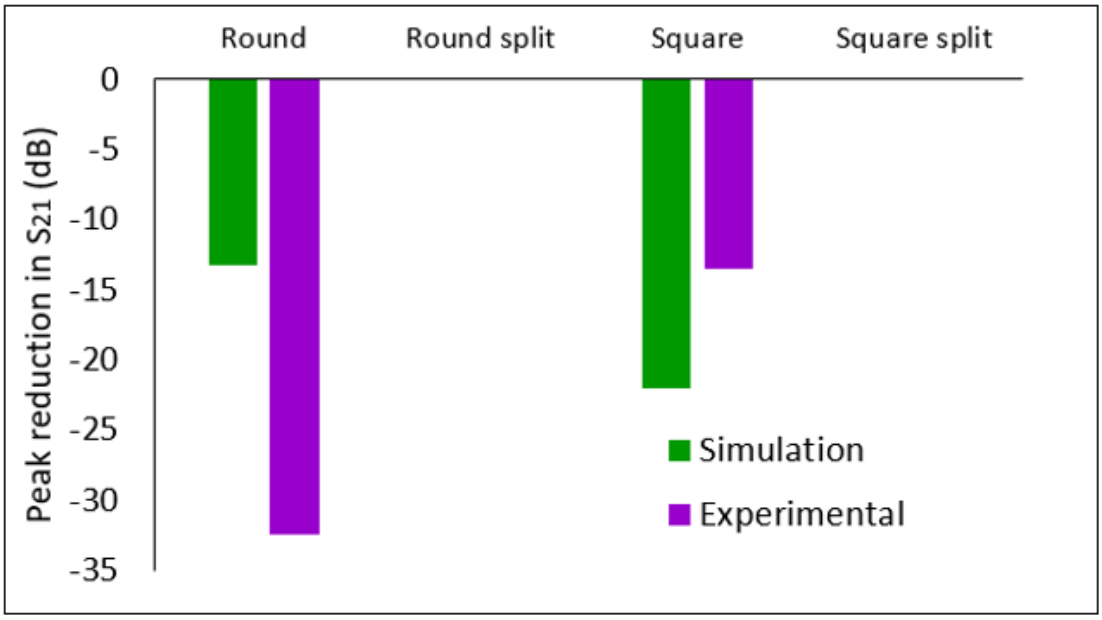

(b)

Figure 85: A comparison of the peak reduction in S_{21} results obtained via simulation, and those obtained experimentally. (a) - Under TE polarization (b) - Under TM polarization.

6.8.1 Result analysis

We can see the narrow band nature of the absorption affected by the split ring resonator structures. This behaviour is useful for specific applications, where the frequency used by the radar installation with which we wish to avoid interfering is known. It is possible to stack metamaterial absorber layers which resonate at different frequencies in order to produce a wideband response [94], for the purposes of avoiding interference with multiple radar installations in the vicinity using different frequencies, or in the case that the frequencies used by nearby radar installations are unknown.

The resonant frequencies were marginally different between the simulated and observed results. When the arrays were studied under TE polarization, we observed a range of resonant frequencies from 2.927GHz to 2.993GHz, with an average resonant frequency between the four manufactured arrays of 2.95175GHz. This corresponds to an error of between 3.7943% and 6.1348% respectively, with an average error value of 4.6720%, when compared with the simulation results. Similarly, when the arrays were studied under TM polarization, we observed a range of resonant frequencies from 2.837GHz to 2.888GHz, with an average resonant frequency between the four manufactured arrays of 2.8625GHz. This corresponds to an error of between 0.603% and 2.411% respectively, with an average error value of 1.507%, when compared with the simulation results. However, it is difficult to interpret these error values for the TM mode in the same way as those for the TE mode, as the resonant frequencies exhibited by the arrays during the simulation of the TM mode was different to those exhibited during TE excitation. In terms of the S_{21} values, we have achieved agreement between the simulation and experimental results, in the sense that the round loops exhibit a greater reduction than the square loops, however there is a discrepancy in the sense that the split loops exhibit higher S_{21} reduction in practice than the split loops, while in simulation, the split loops exhibit better performance. This can be seen in Fig. 8. There are several variables which contribute to these discrepancies - one of these is the fact that the specification given for the relative permittivity of the substrate is $\epsilon_r < 5.4$, allowing a wide range of values around the stated $\epsilon_r = 4.2$. In addition to this,

we observe imperfect tolerances in the wet chemical etching and PCB milling processes. Finally, our measurement process did not make use of an anechoic chamber, so it is likely that some reflections from the environment further contributed to the discrepancies, owing to the slightly different scattering characteristics of each array. Overall, we have been able to demonstrate good agreement between the simulated and observed results.

6.8.2 Conclusion

In conclusion, we have presented a proof of concept in both simulation and practical experimentation for the use of low cost and rapidly producible metamaterial absorbers for radar cross section reduction, and provided a direct comparison of four canonical structures with the aim of advising future works. For entirely metallic structures, if such a metamaterial absorber layer is applied to all surfaces, we could expect to see a reduction in RCS similar to that shown in our results. Metamaterial absorbers can also be redesigned for a wide range of frequencies, making them a tenable solution to a number of modern radar interference problems. We can also conclude that round geometries produce higher absorption, and hence greater RCS reduction, than square geometries. In this regard, round geometries would make a better starting point for the design process of a practical metamaterial absorber.

6.9 Flexible metamaterial absorber

6.9.1 Review of material and manufacturing method selection

Many frequency selective surface and metamaterial designs are based on rigid substrates such as FR-4, and are designed to be manufactured using traditional PCB manufacturing methods such as machining or chemical etching. While these manufacturing techniques and materials offer a low material and manufacturing cost, the rigidity of common substrates makes these designs unsuitable for applications requiring a conformal coating such as wind turbine towers, blades, and nacelles. Additionally, it is difficult and costly to incorporate lumped elements such as re-

sistors into a design. These lumped elements additional increase the inflexibility of the product, as well as increasing its fragility and decreasing its environmental resistance.

Screen printing is a novel, high production volume ready technique involving the deposition of functional coatings on rigid or flexible substrates. In addition to enabling the realization of fine geometries with tight tolerances, one key advantage of the novel screen printing process for the production of frequency selective surfaces and metamaterial designs is that it allows for the deposition of functional inks with varying conductivities, thus removing the need for the use of lumped elements, the characteristics of which can instead be realized using patches or areas of inks possessing a different conductivity, a specific shape, or both. In addition to this, screen printing also allows for the realization of active components e.g. MOSFETs. These advantages enable designs that are less fragile, have lower overall thicknesses, and can be realized using a flexible substrate.

6.9.2 Ink selection and prototyping using the stencil printing technique

In order to verify that the screen printing process would be suitable for the creation of a metamaterial design employing inks of different conductivities, a design was prototyped in CST Microwave Studio and realized using a stencil printing technique similar to the screen printing process. For a successful design, both high and low conductivity sections would be necessary. High conductivity inks are necessary for the production of areas that would normally be constructed using copper, while high resistivity conductive inks can be used to replace lumped elements. A review was conducted of the commercially available inks. The inks surveyed that would be suitable for the creation of high conductivity areas of an eventual metamaterial absorber design can be seen in Table 11.

A commercially available carbon containing ink was used for the stencil printing of the prototype patch-style absorber design. The design in question was a simple periodic chamfered patch style design printed on a thin and flexible PET film. Two designs were produced, each targeting absorption over a different frequency band. The process consisting of laying a stencil over the PET film, applying a conformal

Ink and supplier	**Conductivity (typical)**	**Cost per kg**
AG500-A conductive silver ink (Agas)	2×10^8 S/m	£975.71
Dyesol® DYAG100 conductive silver ink (Sigma Aldrich)	2×10^7 S/m	£14,950
S0860 Conductive Silver ink (Strem Chemicals)	4×10^6 S/m	£8,550.72

Table 11: A table showing the commercially available conductive ink products surveyed for suitability for use in the construction of a flexible screen printed metamaterial absorber/frequency selective surface design.

coating of conductive carbon containing ink, letting the ink dry, and peeling away the stencil. The covered sample can be seen in Fig. 86. A stage in the process of peeling back the stencil can be seen in Fig. **??**. The finished products can be seen in Fig. 87. The flexible characteristics of the finished products can be seen in Fig. 88.

Once these prototypes were completed, they were scanned using an optical surface scanning technique. This operation was performed in order to verify that the technique is capable of producing a deposited layer of ink that was of sufficient thickness to achieve the required feature resistance. A cross section of the deposited ink comprising one of the patches can be see in Fig. 89. A 3D image produced using the optical scanning technique can be seen in Fig. 90.

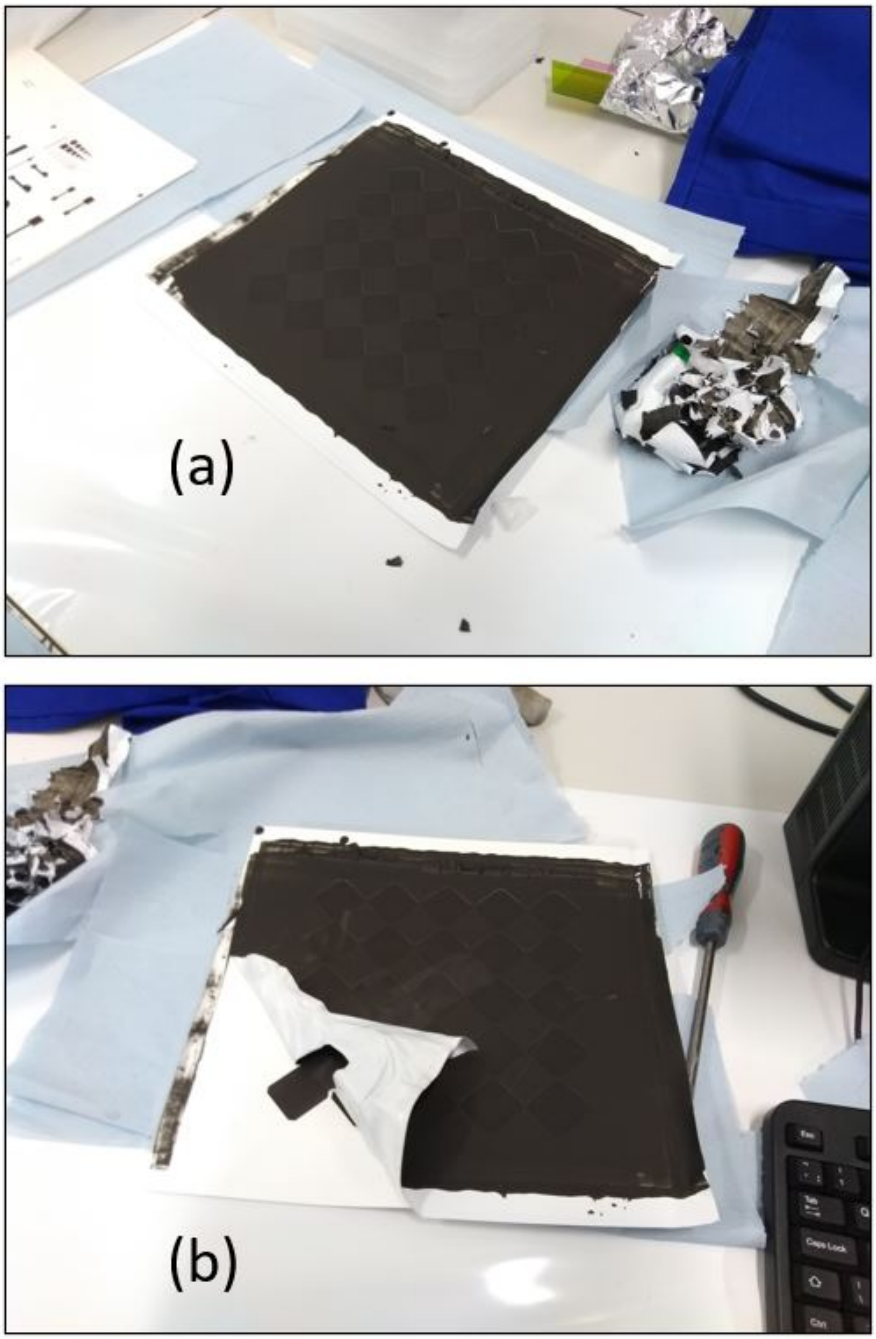

Figure 86: An image of (a) the stencil for the low frequency absorber design after the ink is applied to the stencil, (b) the low frequency absorber design part way through the removal of the stencil.

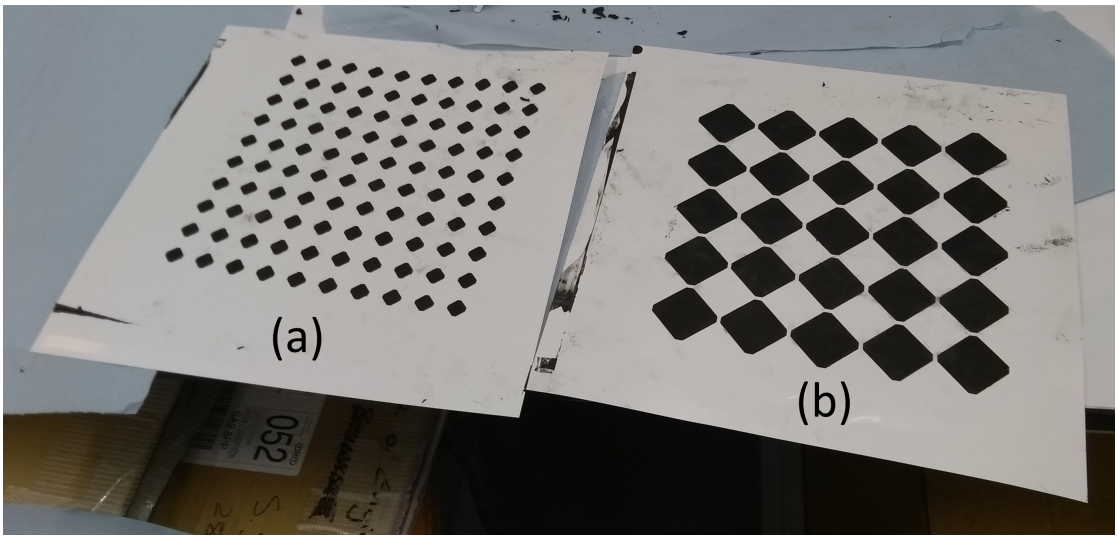

Figure 87: An image of (a) - The high frequency absorber, and (b) the low frequency absorber.

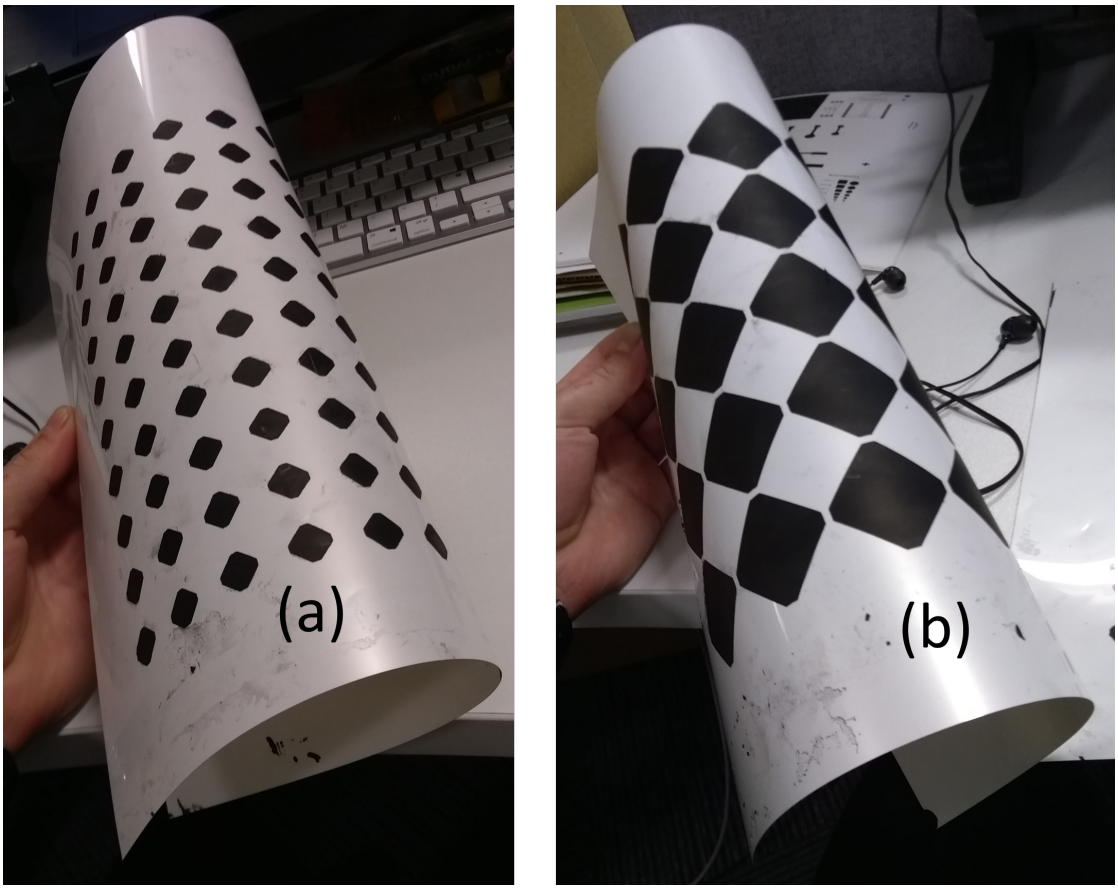

Figure 88: An image showing the flexible characteristics of (a) - The high frequency absorber, and (b) the low frequency absorber.

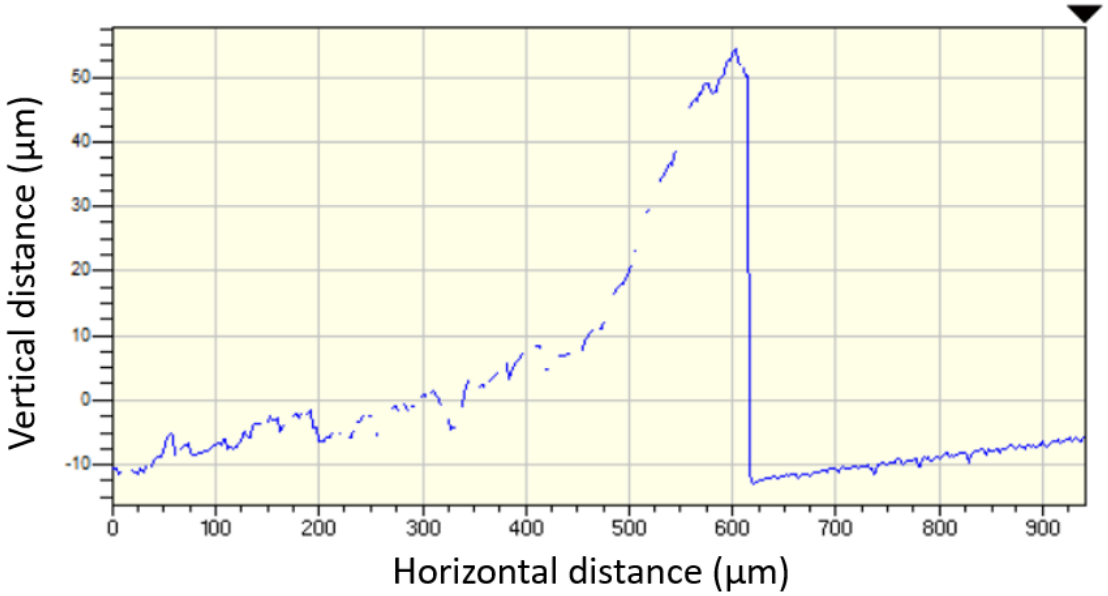

Figure 89: A graph showing a cross section of the distribution of the carbon ink around the edge of one of the chamfered patches.

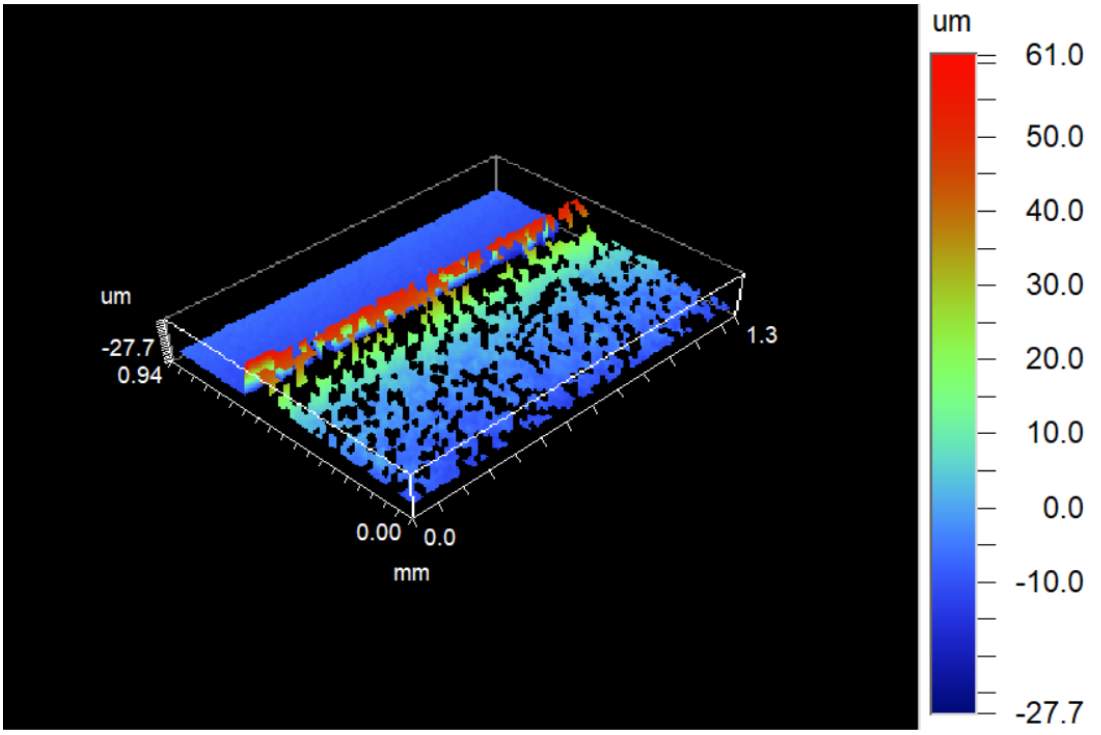

Figure 90: A graph showing the distribution of the carbon ink at the edge of one of the patches in 3 dimensions.

6.9.3 Short literature review and identification of area for innovation

A short literature review was conducted of the works published describing low-profile, flexible-substrate, and multi-band absorptive-transmittive surfaces [95–108].

Among the studied and cited works on the topic of flexible-substrate low-profile absorptive-transmittive structures, a number of common disadvantages were identified. These are listed below:

- Lumped elements (resistors, capacitors) increase cost and manufacturing complexity, as well as making the design less practical and more fragile, thus less suitable for conformal applications
- Where lumped elements are not used, graphene areas are typically used, driving up cost and manufacturing difficulty
- The use of an air gap to separate layers is also not practical for conformal applications, and makes the design more fragile and difficult to install
- For reconfigurable designs, electrical connections are typically used, increasing manufacturing complexity and installation difficulty

After studying the disadvantages associated with the existing designs reported in the literature, I then focused on opportunities for innovation in this field, and settled on a set of requirement for a novel design. These are listed below:

- 4 transmission windows, and at least 3 absorption windows (Major point of novelty and innovation)
- High selectivity
- No lumped components
- No use of graphene
- Performance independent of polarization

- Can tolerate high angle of incidence variation
- Practically applicable and robust design
- Flexible substrate
- Low-profile

An absorptive-transmittive surface (rasorber) is typically comprised of a lossless and lossy layer. The lossless layer acts as a bandpass filter, allowing transmission where necessary, or acting as a ground plane for the lossy layer. The lossy layer absorbs in the rejection bands, but must be transparent in the transmission windows.

I first began with the design of the lossless layer using the equivalent circuit model method described previously. To gain proficiency in the equivalent circuit modelling method, I replicated results from the papers previously listed, using both the CST Microwave Studio and LTSpice circuit simulation software packages. The equivalent circuit model for the proposed lossless layer can be seen in Fig. 91. The S_{11} and S_{21} results produced by the presented circuit can be seen in Fig. 92.

Following the design of the equivalent circuit model, I next considered the 3D design that would realize the desired performance when coupling with free-space radiation. The design I arrived at can be seen in Fig. 93. The characteristics of the designed lossless layer are as follows:

- Thin complementary ring resonator structure provides the necessary multi-band behaviour
- Loop structures are selected for their high selectivity, simplicity, and polarization independence
- Ultra-thin, flexible, 0.175mm substrate used
- Suitable for conformal applications

The design exhibited the necessary quad-passband, high-selectivity characteristics.

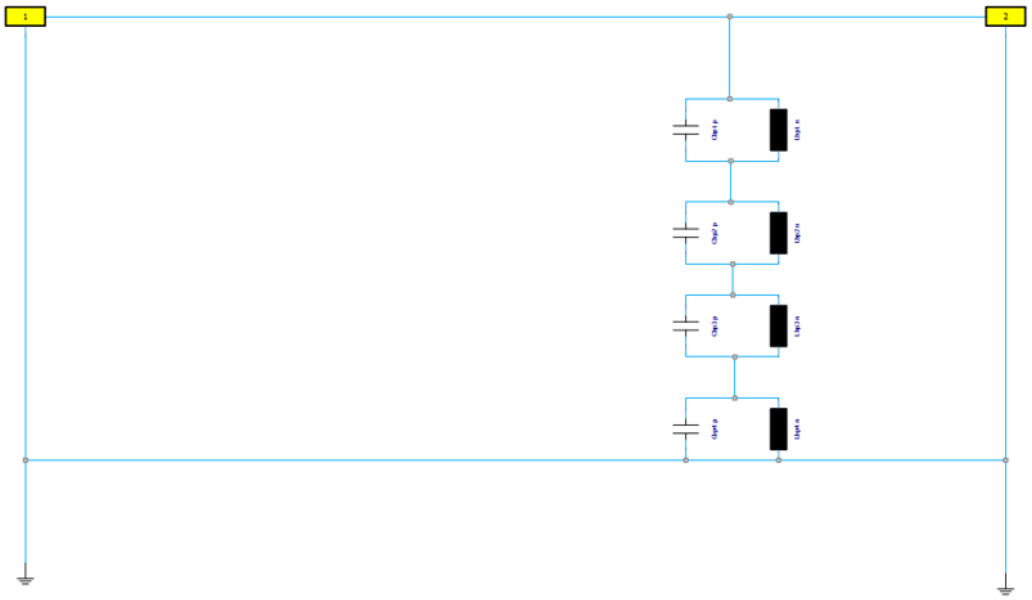

Figure 91: A diagram of the equivalent circuit model for the proposed lossless layer of the rasorber structure.

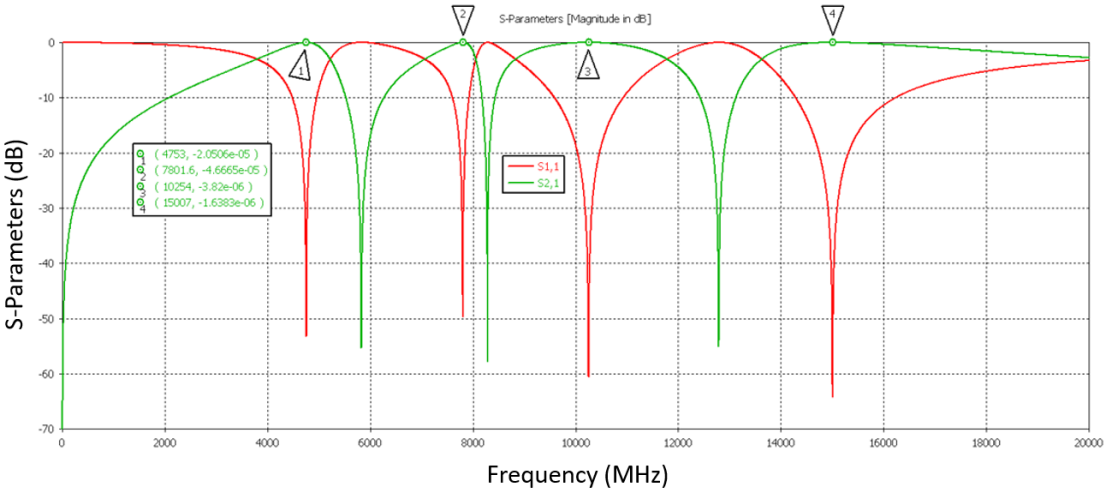

Figure 92: A chart showing the some of the S-parameters produced by the equivalent circuit model of the lossless layer of the rasorber structure.

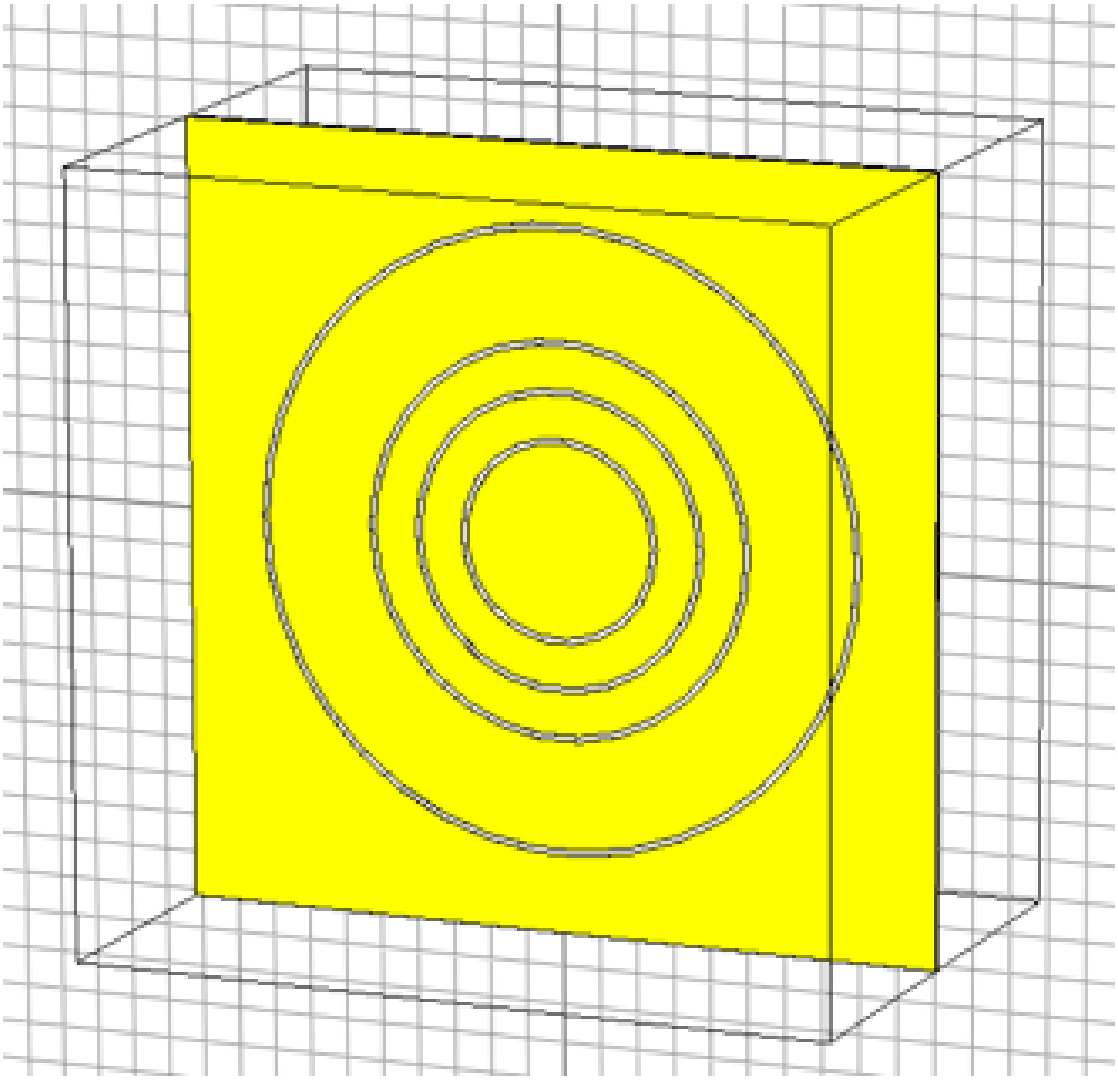

Figure 93: A diagram showing the 3D design for the lossless layer of the proposed rasorber.

I then shifted my attention to the design of the lossy layer. The lossy layer absorbs in the rejection bands, but must be transparent in the transmission windows. Most designs use a combined loop type and n-pole centre-connected structure for the unit cell of the lossy layer, so I started out with a loop-type design for the 3D structure. This can be seen in Fig. 94.

The results of the simulation of the lossy layer can be seen in Fig. 95

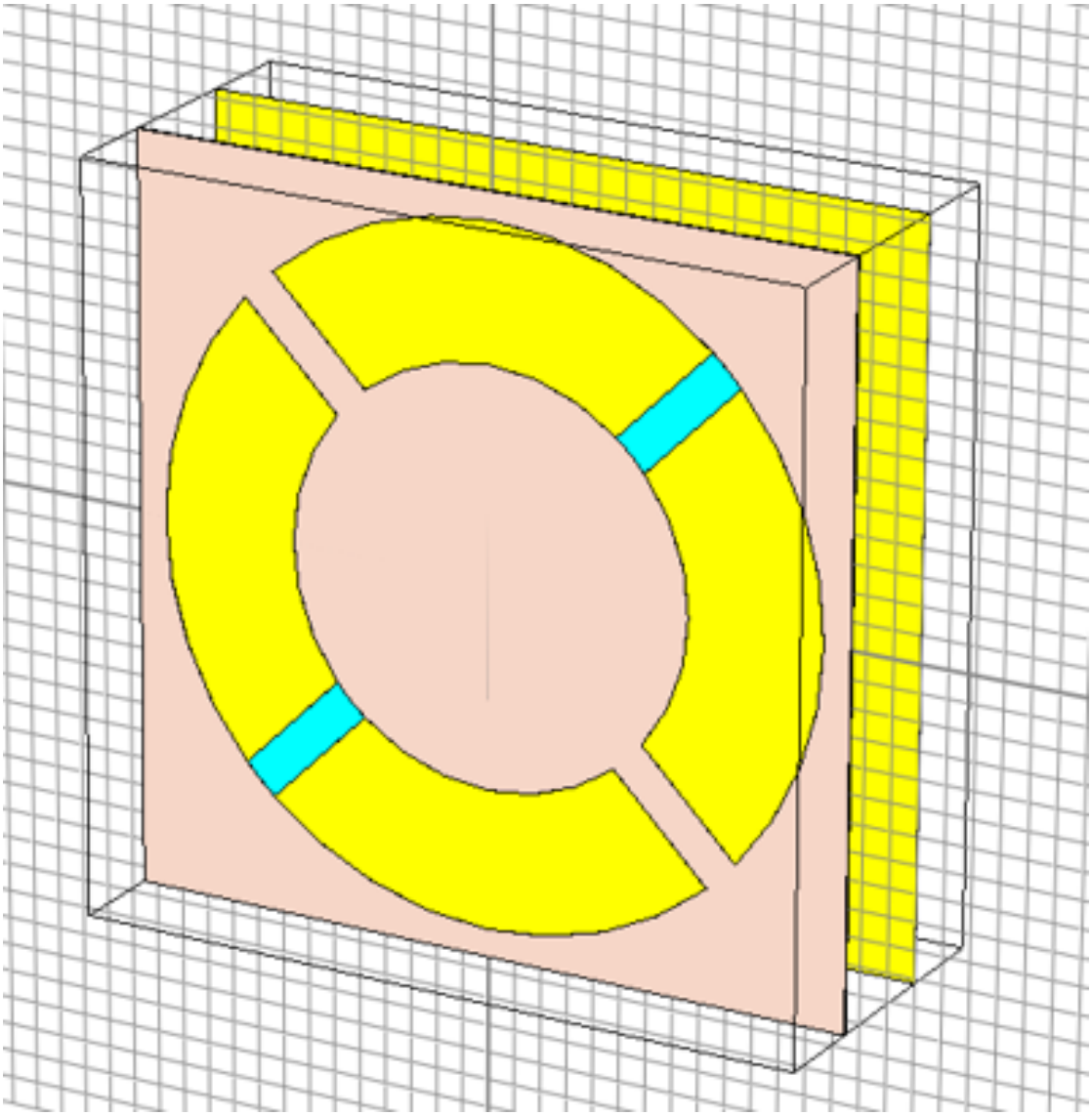

Figure 94: A diagram showing the 3D design for the lossy layer of the proposed rasorber.

Unfortunately, this is as far as I was able to get with the development of this design. The following points are left in terms of future work:

- Design of the lossy layer - Equivalent circuit model simulations are the next step in the lossy layer design

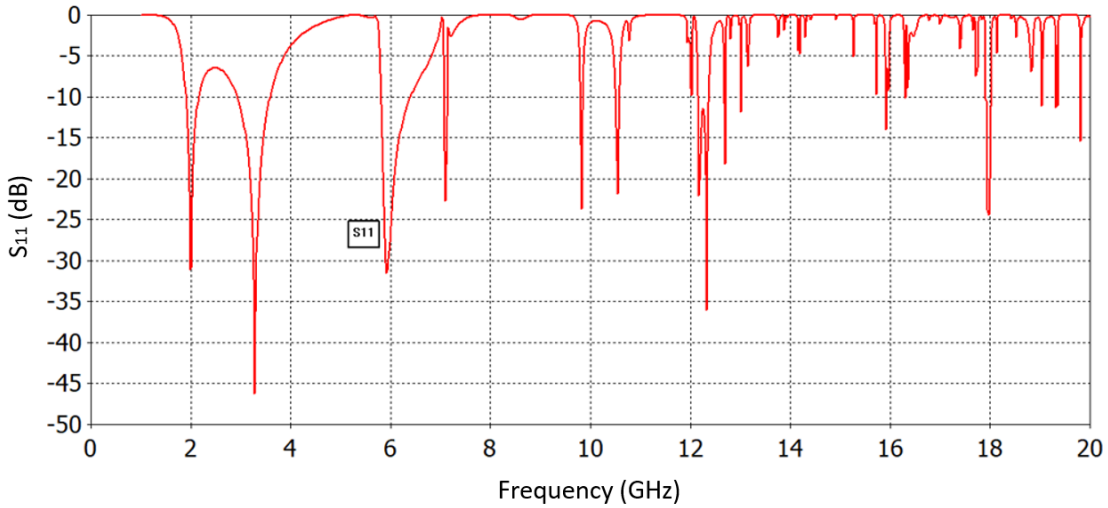

Figure 95: A chart showing the S-parameters of the lossy layer design of the proposed rasorber.

- Optimization of the structure once both surfaces are modelled together as opposed to individually (CST)
- Manufacturing and experimental testing

7 Conclusion and Future Work

7.1 Thesis summary

This work is primarily focused on the topics of radar interference and the nature of radar interference generated wind turbines, different RCS characterization techniques and the importance of obtaining high quality RCS data for novel structures, as well as techniques used for RCS reduction and the study of frequency selective surfaces and metamaterials.

In Chapter 1, the motivations for this work are identified and described. Additionally, the research objectives and methods used are described. A list list of publications based on the work carried out in this thesis are presented preceding Chapter 1.

In Chapter 2, a detailed literature review is presented covering the topics which underpin this work, with a specific focus on the work carried out in the fields of scale model radar cross section testing, the characterization of wind-turbine radar interference, and the use of frequency selective surfaces and metamaterials for RCS reduction. The project requirements and computational resources utilized during the project are also described here.

In Chapters 3 and **??**, the efforts spent on the simulation of the nature and magnitude of the interference generated by the Crossflow turbine and other wind turbine types on civil aviation radar are described. The computational methods and the different software packages utilized are also described. Detailed results of simulations of the RCS of the Crossflow turbine and a traditional horizontal-axis wind turbine design are presented and compared. Results from analytical work carried out to ascertain the dynamic radar characteristics and Doppler spectrum contamination generated by the Crossflow turbine are also presented and described.

In Chapter 5, a novel radar cross section characterization method and system are described with a variety of advantages over existing systems, namely a low-cost, compact nature, millimeter-wave frequency range operation, and a lack of a requirement for an anechoic chamber. This system was used to characterize the

radar cross section of a scale model of the Crossflow turbine, and the results from this work are presented and good agreement is demonstrated with the simulation results presented in Chapter **??**.

In Chapter 6, a description of the work centering around the use of FSS structures and metamaterial absorbers for the purposes of RCS reduction is given, and the associated results are presented. A novel design of a high-efficacy, low-profile, and mass-producible absorber structure is presented as a suggested solution for some of the interference generated by wind turbines and large structures in the vicinity of radar installations. The theory underpinning the design of FSS and metamaterials is presented and the work carried out towards the realization of a novel flexible-substrate multi-band absorptive transmittive surface is described.

7.2 Contribution

The contributions of this work are numerous. Firstly, research has been carried out into the RCS modeling of large structures and their characterization under dynamic conditions. Novel data has been presented on the RCS and Doppler spectrum characteristics of the Crossflow turbine, a novel design of wind turbine with a variety of advantages over traditional designs. This data was compared against the simulated RCS of a traditional HAWT design, and significant advantages in terms of static and dynamic RCS characteristics were demonstrated for the Crossflow turbine.

In order to validate the simulation results presented, a scale model RCS measurement approach was chosen. A novel scale model RCS characterization system was designed and constructed using predominantly off-the-shelf, commercially available parts. This system has a variety of advantages over the bespoke systems traditionally used for scale model RCS measurements, namely a low-cost, high measurement speed, compact nature, the lack of a need for an anechoic chamber, high-frequency operation, and good accuracy. This will enable an iterative, RCS-driven design process for a variety of structures.

Additionally, research has been carried out into the use of frequency selective surfaces and metamaterial absorber structures for RCS reduction. A proof of con-

cept was demonstrated in simulation for the use of a low-profile frequency selective surfaces for the purpose of reducing the RCS of a large structure such as a wind turbine. Several canonical metamaterial absorber structures were also characterized for their performance with this application in mind. Experiments were also carried out assessing the suitability of the screen-printing process for the construction of ultra-thin and flexible metamaterial absorber structures that have various advantages over designs traditionally constructed using a rigid substrate and/or lumped elements. Absorbers and frequency selective surface structures constructed using this method would be more suitable for retrofitting to existing wind turbine structures without impacting their aerodynamic performance, as compared with existing designs in the literature. As part of this work, a novel 5-band ultra-thin flexible substrate frequency selective structure was designed and demonstrated in simulation.

7.3 Future work

Future works may seek to improve on the RCS characterization approach presented in this work, particularly in terms of productization and refinement of construction. Future works may also seek to use different combinations of off-the shelf parts to realize such systems in a similar way at higher frequencies of operation to allow for the use of smaller and easier to construct scale models.

In terms of the work regarding the use of FSS and metamaterial absorbers for reducing the impact of wind turbines and other large structures on nearby radar installations, future works may seek to develop the concept of a flexible substrate ultrathin absorber realized using screen printing technology further, as well as looking to realize absorptive-transmittive structures using the same techniques.

References

[1] S. Ghosh and K. V. Srivastava, "An equivalent circuit model of fss-based metamaterial absorber using coupled line theory," *IEEE Antennas and Wireless Propagation Letters*, vol. 14, pp. 511–514, 2015.

[2] R. Garg and I. J. Bahl, "Characteristics of coupled microstriplines," *IEEE Transactions on Microwave Theory and Techniques*, vol. 27, pp. 700–705, Jul 1979.

[3] F. Kong, Y. Zhang, R. Palmer, and Y. Bai, "Wind turbine radar signature characterization by laboratory measurements," in *2011 IEEE RadarCon (RADAR)*, pp. 162–166, May 2011.

[4] H. Heemskerk, "Naval stealth from design to real life - the rnln adcf." Stealth, 26th and 27th April 2006, The hatton, London, London, SMi Conferences Ltd, 2006, 2006. TNO Defensie en Veiligheid.

[5] J. Perry and A. Biss, "Wind farm clutter mitigation in air surveillance radar," in *2007 IEEE Radar Conference*, pp. 93–98, April 2007.

[6] I. R. E. Agency, "Future of wind."

[7] R. Best and P. J. Burke, "Adoption of solar and wind energy: The roles of carbon pricing and aggregate policy support," *Energy Policy*, vol. 118, pp. 404–417, July 2018.

[8] S. Bachmann, Y. Al-Rashid, P. Bronecke, R. Palmer, B. Isom, and L. Martin, "SUPPRESSION OF THE WINDFARM CONTRIBUTION FROM THE ATMOSPHERIC RADAR RETURNS," p. 5.

[9] R. J. Vogt, T. D. Crum, M. J. B. Sandifer, E. J. Ciardi, and R. Guenther, "A WAY FORWARD WIND FARM – WEATHER RADAR COEXISTENCE," p. 9.

[10] B. M. Isom, R. D. Palmer, G. S. Secrest, R. D. Rhoton, D. Saxion, T. L. Allmon, J. Reed, T. Crum, and R. Vogt, "Detailed Observations of Wind Turbine Clutter with Scanning Weather Radars," *Journal of Atmospheric and Oceanic Technology*, vol. 26, pp. 894–910, May 2009.

[11] B. M. Kent, K. C. Hil, A. Buterbaugh, G. Zelinski, R. Hawley, L. Cravens, Tri-Van, C. Vogel, and T. Coveyou, "Dynamic Radar Cross Section and Radar Doppler Measurements of Commercial General Electric Windmill Power Turbines Part 1: Predicted and Measured Radar Signatures," *IEEE Antennas and Propagation Magazine*, vol. 50, pp. 211–219, Apr. 2008.

[12] O. of the Director of Defense Research and Engineering, *The Effect of Windmill Farms On Military Readiness*. Department of Defense, 2006.

[13] N. Litov, H. Zhou, and A. Mehta, "Low Cost Millimetre-Wave Scale Model RCS Characterisation," in *2020 IEEE International Symposium on Antennas and Propagation and North American Radio Science Meeting*, pp. 1147–1148, July 2020. ISSN: 1947-1491.

[14] F. Kong, Y. Zhang, and R. D. Palmer, "Wind Turbine Radar Interference Studies by Polarimetric Measurements of a Scaled Model," *IEEE Transactions on Aerospace and Electronic Systems*, vol. 49, pp. 1589–1600, July 2013. Conference Name: IEEE Transactions on Aerospace and Electronic Systems.

[15] R. Vogt, T. D Crum, J. B Maj, S. , E. J Ciardi, and R. Guenther, "A way forward; wind farm–weather radar coexistence," 01 2009.

[16] T. M. C. JASON Program Office, *Wind farms and radar*. 2008.

[17] B. M. Isom, R. D. Palmer, G. S. Secrest, R. D. Rhoton, D. Saxion, T. L. Allmon, J. Reed, T. Crum, and R. Vogt, "Detailed observations of wind turbine clutter with scanning weather radars," *Journal of Atmospheric and Oceanic Technology*, vol. 26, no. 5, pp. 894–910, 2009.

[18] "Radio Detection and Ranging," *Nature*, vol. 152, pp. 391–392, Oct. 1943. Number: 3857 Publisher: Nature Publishing Group.

[19] C. Hülsmeyer, "Verfahren, um metallische Gegenstände mittels elektrischer Wellen einem Beobachter zu melden.."

[20] W. E. Willshaw, L. Rushforth, A. G. Stainsby, R. Latham, A. W. Balls, and A. H. King, "The high-power pulsed magnetron: development and design for radar applications," *Journal of the Institution of Electrical Engineers - Part IIIA: Radiolocation*, vol. 93, pp. 985–1005, Jan. 1946. Publisher: IET Digital Library.

[21] M. I. Skolnik, *Radar handbook*. McGraw Hill, 1990.

[22] F. A. A. (FAA), "Airport surveillance radar." https://www.faa.gov/air_traffic/technology/asr-11. Accessed 20/02/2018.

[23] V. S. Chernyak, *Fundamentals of multisite radar systems: multistatic radars and multiradar systems*. CRC Press, 1998.

[24] J. Shipman, J. D. Wilson, and C. A. Higgins, *An Introduction to Physical Science*. Cengage learning, 2015.

[25] J. Shapira and S. Y. Miller, *CDMA Radio with repeaters*. Springer, 2007.

[26] Y. Yamada, N. Michishita, and Q. D. Nguyen, "Calculation and measurement methods for rcs of a scale model airplane," in *2014 International Conference on Advanced Technologies for Communications (ATC 2014)*, pp. 69–72, Oct 2014.

[27] J. Ochodnicky, Z. Matousek, M. Sostronek, and A. Hykel, "Radar cross section measurement by subscale models," in *2008 International Radar Symposium*, pp. 1–4, May 2008.

[28] N. Litov, A. Pal, and A. Mehta, "Ring Resonator Metamaterials for Radar Cross Section Reduction," in *2019 IEEE International Symposium on An-*

tennas and Propagation and USNC-URSI Radio Science Meeting, pp. 1329–1330, July 2019. ISSN: 1947-1491.

[29] H.-K. Jang, W.-H. Choi, C.-G. Kim, J.-B. Kim, and D.-W. Lim, "Manufacture and characterization of stealth wind turbine blade with periodic pattern surface for reducing radar interference," *Composites Part B: Engineering*, vol. 56, pp. 178–183, Jan. 2014.

[30] W. Salisbury, ""patent no. 2599944 - absorbent body for electromagnetic waves," June 1952.

[31] A. Lai, T. Itoh, and C. Caloz, "Composite right/left-handed transmission line metamaterials," *IEEE Microwave Magazine*, vol. 5, pp. 34–50, Sept 2004.

[32] R. W. Ziolkowski and N. Engheta, "Metamaterial special issue introduction," *IEEE Transactions on Antennas and Propagation*, vol. 51, pp. 2546–2549, Oct 2003.

[33] J. B. Pendry, A. J. Holden, D. J. Robbins, and W. J. Stewart, "Magnetism from conductors and enhanced nonlinear phenomena," *IEEE Transactions on Microwave Theory and Techniques*, vol. 47, pp. 2075–2084, Nov 1999.

[34] Great Britain, Civil Aviation Authority, and Safety and Airspace Regulation Group, *CAP 670: Air traffic services safety requirements*. 2013. OCLC: 885443419.

[35] Great Britain, Civil Aviation Authority, and Safety and Airspace Regulation Group, "CAP 764: Policy and Guidelines on Wind Turbines."

[36] G. Fixter, Greg Peter Wade (Hook, G. Spooner, Christopher Douglas James (Bracknell, and G. Perry, Christopher James (Yateley, "Wind turbine blades," March 2015.

[37] G. J. Poupart, "WIND FARMS IMPACT ON RADAR AVIATION INTERESTS - FINAL REPORT," tech. rep., Qinetiq, 2003.

[38] *Metamaterials and Plasmonics: Fundamentals, Modelling, Applications (NATO Science for Peace and Security Series B: Physics and Biophysics).* Springer, 2008.

[39] D. Sievenpiper, L. Zhang, R. Broas, N. Alexopolous, and E. Yablonovitch, "High-impedance electromagnetic surfaces with a forbidden frequency band," *IEEE Transactions on Microwave Theory and Techniques*, vol. 47, no. 11, pp. 2059–2074, 1999.

[40] D. R. Smith, "About metamaterials – duke home page," *Duke University.*

[41] R. A. Shelby, "Experimental verification of a negative index of refraction," *Science*, vol. 292, pp. 77–79, apr 2001.

[42] H. B. Baskey, A. K. Jha, and M. J. Akhtar, "Design of metamaterial based structure for the radar cross section reduction of a microstrip antenna," in *2014 IEEE International Microwave and RF Conference (IMaRC)*, pp. 104–107, Dec 2014.

[43] M. Paquay, J. C. Iriarte, I. Ederra, R. Gonzalo, and P. de Maagt, "Thin amc structure for radar cross-section reduction," *IEEE Transactions on Antennas and Propagation*, vol. 55, pp. 3630–3638, Dec 2007.

[44] J. C. I. Galarregui, A. T. Pereda, J. L. M. de Falcón, I. Ederra, R. Gonzalo, and P. de Maagt, "Broadband radar cross-section reduction using amc technology," *IEEE Transactions on Antennas and Propagation*, vol. 61, pp. 6136–6143, Dec 2013.

[45] Y. C. Song, J. Ding, C. J. Guo, Y. H. Ren, and J. K. Zhang, "Ultra-broadband backscatter radar cross section reduction based on polarization-insensitive metasurface," *IEEE Antennas and Wireless Propagation Letters*, vol. 15, pp. 329–331, 2016.

[46] W. Chen, C. A. Balanis, and C. R. Birtcher, "Checkerboard ebg surfaces for wideband radar cross section reduction," *IEEE Transactions on Antennas and Propagation*, vol. 63, pp. 2636–2645, June 2015.

[47] M. F. Abedin, M. Z. Azad, and M. Ali, "Wideband smaller unit-cell planar ebg structures and their application," *IEEE Transactions on Antennas and Propagation*, vol. 56, pp. 903–908, March 2008.

[48] D. Schurig, J. J. Mock, B. J. Justice, S. A. Cummer, J. B. Pendry, A. F. Starr, and D. R. Smith, "Metamaterial electromagnetic cloak at microwave frequencies," *Science*, vol. 314, pp. 977–980, nov 2006.

[49] J. B. Pendry, "Controlling electromagnetic fields," *Science*, vol. 312, pp. 1780–1782, jun 2006.

[50] U. Leonhardt, "Optical conformal mapping," *Science*, vol. 312, pp. 1777–1780, jun 2006.

[51] Y. Huang, Y. Feng, and T. Jiang, "Electromagnetic cloaking by layered structure of homogeneous isotropic materials," *Optics Express*, vol. 15, p. 11133, aug 2007.

[52] N. Kumutha, K. Hariharan, B. Manimegalai, and N. Amutha, "Low rcs using superluminal propagation," in *TENCON 2017 - 2017 IEEE Region 10 Conference*, pp. 2658–2661, Nov 2017.

[53] M. G. Silveirinha, A. Alù, and N. Engheta, "Parallel-plate metamaterials for cloaking structures," *Physical Review E*, vol. 75, mar 2007.

[54] A. Alù and N. Engheta, "Achieving transparency with plasmonic and metamaterial coatings," *Phys. Rev. E*, vol. 72, p. 016623, Jul 2005.

[55] B. S. J, A. Rajeswari, G. Thomas, and P. H. Rao, "Rcs reduction with rf cloak," in *2016 International Conference on Wireless Communications, Signal Processing and Networking (WiSPNET)*, pp. 50–51, March 2016.

[56] F. Yue-Nong, C. Yong-Zhi, N. Yan, W. Xian, and G. Rong-Zhou, "An ultrathin wide-band planar metamaterial absorber based on a fractal frequency selective surface and resistive film," *Chinese Physics B*, vol. 22, no. 6, p. 067801, 2013.

[57] L. A. de Andrade, L. S. C. dos Santos, and A. M. Gama, "Analysis of radar cross section reduction of fighter aircraft by means of computer simulation," *J. Aerosp. Technol. Manag*, vol. 6, pp. 177–182, apr-jun 2014.

[58] J. Vidal, "Health risks of shipping pollution have been 'underestimated'," *The Guardian*, Apr 2009.

[59] "Global trade and fuels assessment— additional eca modeling scenarios," May 2009.

[60] V. Borkar, A. Ghosh, R. Singh, and N. Chourasia, "Radar Cross-section Measurement Techniques," *Defence Science Journal*, vol. 60, pp. 204–212, Mar. 2010.

[61] WalesOnline, "£40m to upgrade business computing," Mar 2013.

[62] J. D. Kraus, *Antennas.* McGraw-Hill, 1950.

[63] H. A. Wheeler, "Fundamental limitations of small antennas," *Proceedings of the IRE*, vol. 35, pp. 1479–1484, Dec 1947.

[64] B. M. Kent, K. C. Hil, A. Buterbaugh, G. Zelinski, R. Hawley, L. Cravens, Tri-Van, C. Vogel, and T. Coveyou, "Dynamic radar cross section and radar doppler measurements of commercial general electric windmill power turbines part 1: Predicted and measured radar signatures," *IEEE Antennas and Propagation Magazine*, vol. 50, pp. 211–219, April 2008.

[65] S. Samuel, "Small-scale HAWT | 3D CAD Model Library | GrabCAD,"

[66] REMCOM, "Overview of Remcom's Wind Turbine Research and Capabilities — Remcom - Articles and Papers." Library Catalog: www.remcom.com.

[67] D. Jenn and C. Ton, "Wind Turbine Radar Cross Section," *International Journal of Antennas and Propagation*, vol. 2012, pp. 1–14, 2012.

[68] L. S. Rashid and A. K. Brown, "RCS and radar propagation near offshore wind farms," in *2007 IEEE Antennas and Propagation Society International Symposium*, pp. 4605–4608, June 2007. ISSN: 1947-1491.

[69] Y. Zhang, A. Huston, R. D. Palmer, R. Albertson, F. Kong, and S. Wang, "Using Scaled Models for Wind Turbine EM Scattering Characterization: Techniques and Experiments," *IEEE Transactions on Instrumentation and Measurement*, vol. 60, pp. 1298–1306, Apr. 2011. Conference Name: IEEE Transactions on Instrumentation and Measurement.

[70] F. Kong, Y. Zhang, R. Palmer, and Y. Bai, "Wind Turbine radar signature characterization by laboratory measurements," in *2011 IEEE RadarCon (RADAR)*, pp. 162–166, May 2011. ISSN: 2375-5318, 1097-5659, 1097-5659.

[71] "Introduction to Micro-Doppler Effects - MATLAB & Simulink - MathWorks United Kingdom."

[72] M. J. Coulombe, T. Horgan, J. Waldman, G. Szatkowski, and W. Nixon, "A 524 GHZ Polarimetric Compact Range for Scale Model RCS Measurements," p. 7.

[73] B. Gallardo-Hernando, F. Pérez-Martínez, and F. Aguado-Encabo, "Detection and mitigation of wind turbine clutter in c-band meteorological radar," vol. 4, pp. 520 – 527, 09 2010.

[74] M. K. J. H. H. L. B. L.-P. Schmidt, "Feasibility of automotive radar at frequencies beyond 100 ghz," *International Journal of Microwave and Wireless Technologies*, vol. 5, pp. 49–54, 2013.

[75] G. R. Curry, *Radar system performance modeling*. Artech House radar library, Boston: Artech House, 2nd ed ed., 2005. OCLC: ocm56672359.

[76] "IWR6843ISK-ODS: Verification of Rx Gain - Sensors forum - Sensors - TI E2E support forums."

[77] A. Mani, *Raw ADC data to dBFs*. Texas Instruments.

[78] "AWR1843BOOST Evaluation board | TI.com."

[79] L. Sevgi, Z. Rafiq, and I. Majid, "Radar Cross Section (RCS) Measurements," *IEEE Antennas and Propagation Magazine*, vol. 55, pp. 278–291, Dec. 2013.

[80] Y. Pang, H. Cheng, Y. Zhou, and J. Wang, "Upper bound for the bandwidth of ultrathin absorbers comprising high impedance surfaces," *IEEE Antennas and Wireless Propagation Letters*, vol. 11, pp. 224–227, 2012.

[81] F. Costa, S. Genovesi, and A. Monorchio, "On the bandwidth of high-impedance frequency selective surfaces," *IEEE Antennas and Wireless Propagation Letters*, vol. 8, pp. 1341–1344, 2009.

[82] J.-S. Hong, *Microstrip filters for RF/microwave applications*. John Wiley & Sons, 2011.

[83] W. G. Rees, *Physical Principles of Remote Sensing*. Cambridge University Press, 2 ed., 2001.

[84] Y. He and J. Jiang, "An ultra-wideband metamaterial absorber with active frequency selective surface," in *2015 9th International Congress on Advanced Electromagnetic Materials in Microwaves and Optics (METAMATERIALS)*, pp. 100–102, Sept. 2015.

[85] H. Jeong and S. Lim, "Broadband frequency-reconfigurable metamaterial absorber using switchable ground plane," *Scientific Reports*, vol. 8, p. 9226, Dec. 2018.

[86] S. Ma, X. Hou, Q. Zhang, Y. Yang, and Y. Tang, "Ultra-wideband metamaterial absorber using three-layer ring and patch resonators," in *2018 IEEE MTT-S International Wireless Symposium (IWS)*, pp. 1–3, May 2018.

[87] J. Tang, Z. Xiao, K. Xu, X. Ma, and Z. Wang, "Polarization-Controlled Metamaterial Absorber with Extremely Bandwidth and Wide Incidence Angle," *Plasmonics*, vol. 11, pp. 1393–1399, Oct. 2016.

[88] Y. Zhang, Y. Lyu, D. Liao, and H. Wang, "Ultrathin multiband microwave absorber based on electric-field-coupled-LC resonators," in *2017 International Applied Computational Electromagnetics Society Symposium (ACES)*, pp. 1–2, Aug. 2017.

[89] S. Bhattacharyya, D. Chaurasiya, K. V. Srivastava, A. Bhattacharya, and S. Ghosh, "Compact multi-band polarisation-insensitive metamaterial absorber," *IET Microwaves, Antennas & Propagation*, vol. 10, pp. 94–101, Jan. 2016.

[90] D. Schurig, J. J. Mock, B. J. Justice, S. A. Cummer, J. B. Pendry, A. F. Starr, and D. R. Smith, "Metamaterial electromagnetic cloak at microwave frequencies," *Science*, vol. 314, pp. 977–980, nov 2006.

[91] S. Ghosh and K. V. Srivastava, "An Equivalent Circuit Model of FSS-Based Metamaterial Absorber Using Coupled Line Theory," *IEEE Antennas and Wireless Propagation Letters*, vol. 14, pp. 511–514, 2015.

[92] F. Costa, S. Genovesi, A. Monorchio, and G. Manara, "A Circuit-Based Model for the Interpretation of Perfect Metamaterial Absorbers," *IEEE Transactions on Antennas and Propagation*, vol. 61, pp. 1201–1209, Mar. 2013.

[93] S. Yadav, M. P. Abegaonkar, M. M. Sharma, and C. P. Jain, "A quad-band polarization independent metamaterial absorber," in *2017 IEEE Applied Electromagnetics Conference (AEMC)*, pp. 1–2, Dec. 2017.

[94] X. Yin, L. Chen, and X. Li, "Ultra-Broadband Super Light Absorber Based on Multi-Sized Tapered Hyperbolic Metamaterial Waveguide Arrays," *Journal of Lightwave Technology*, vol. 33, pp. 3704–3710, Sept. 2015.

[95] T. Chen, X. Liu, H. Guo, and C. Liu, "A Frequency Selective Rasorber with Switchable Operating Modes," in *2019 International Symposium on Antennas and Propagation (ISAP)*, pp. 1–3, Oct. 2019. ISSN: null.

[96] Q. Zhou, M. Guo, H. Moghadas, Z. Wu, P. Liu, and M. Daneshmand, "A Frequency Selective Rasorber With Three Transmission Bands and Three Absorption Bands," *IEEE Access*, vol. 7, pp. 160973–160981, 2019.

[97] S. C. Bakshi, D. Mitra, and S. Ghosh, "A Frequency Selective Surface Based Reconfigurable Rasorber With Switchable Transmission/Reflection Band," *IEEE Antennas and Wireless Propagation Letters*, vol. 18, pp. 29–33, Jan. 2019.

[98] Y. Diao, Q. Guo, L. Chen, and Z. Li, "An Absorptive/Transmissive Frequency Selective Surface with a High-selectivity Passband," in *2018 Cross Strait Quad-Regional Radio Science and Wireless Technology Conference (CSQRWC)*, pp. 1–2, July 2018. ISSN: 2377-8512.

[99] X. Zhang, W. Wu, Y. Ma, C. Wang, C. Li, and N. Yuan, "Design Dual-Polarization Frequency Selective Rasorber Using Split Ring Resonators," *IEEE Access*, vol. 7, pp. 101139–101146, 2019.

[100] A. Motevasselian and B. L. G. Jonsson, "Design of a wideband rasorber with a polarisation-sensitive transparent window," *IET Microwaves, Antennas & Propagation*, vol. 6, pp. 747–755, May 2012.

[101] M. Guo, Q. Chen, Z. Sun, D. Sang, and Y. Fu, "Design of Dual-Band Frequency-Selective Rasorber," *IEEE Antennas and Wireless Propagation Letters*, vol. 18, pp. 841–845, May 2019.

[102] H. Chen, Z. G. Liu, W. Jun Wu, W. B. Lu, and A. Qi Zhang, "Flexible Rasorber Based on Graphene," in *2019 International Symposium on Antennas and Propagation (ISAP)*, pp. 1–2, Oct. 2019. ISSN: null.

[103] M. Qu and S. Li, "Graphene-based polarization insensitive rasorber with tunable passband," *Results in Physics*, vol. 14, p. 102172, Sept. 2019.

[104] S. Yu, N. Kou, Z. Ding, and Z. Zhang, "Harmonic Suppressed Frequency Selective Rasorber using Resistive-film Sheet and Square Loops Resonator," *IEEE Antennas and Wireless Propagation Letters*, pp. 1–1, 2019.

[105] Y. Han, W. Che, X. Xiu, W. Yang, and C. Christopoulos, "Switchable Low-Profile Broadband Frequency-Selective Rasorber/Absorber Based on Slot Arrays," *IEEE Transactions on Antennas and Propagation*, vol. 65, pp. 6998–7008, Dec. 2017.

[106] Y. Wang, S.-S. Qi, Z. Shen, and W. Wu, "Tunable Frequency-Selective Rasorber Based on Varactor-Embedded Square-Loop Array," *IEEE Access*, vol. 7, pp. 115552–115559, 2019.

[107] X. Yan, X. Kong, Q. Wang, L. Xing, F. Xue, Y. Xu, S. Jiang, and X. Liu, "Water-Based Reconfigurable Frequency Selective Rasorber With Thermally Tunable Absorption Band," *IEEE Transactions on Antennas and Propagation*, vol. 68, pp. 6162–6171, Aug. 2020. Conference Name: IEEE Transactions on Antennas and Propagation.

[108] B. Li and Z. Shen, "Wideband 3D Frequency Selective Rasorber," *IEEE Transactions on Antennas and Propagation*, vol. 62, pp. 6536–6541, Dec. 2014.